ELECTROMAGNETIC MANIPULATION OF PLASMA LAYER FOR RE-ENTRY BLACKOUT MITIGATION

by

Min Kwan Kim

A dissertation submitted in partial fulfillment
of the requirements for the degree of
Doctor of Philosophy
(Aerospace Engineering)
in The University of Michigan
2009

Doctoral Committee:

Professor Iain D. Boyd, Co-Chairperson
Professor Michael Keidar, Co-Chairperson
Professor Alec D. Gallimore
Professor Brian E. Gilchrist
Professor Kenneth G. Powell

Men of age object too much,
consult too long,
adventure too little,
repent too soon,
and seldom drive business home to the full period,
but content themselves with a mediocrity of success.

- by *Francis Bacon* -

To my beautiful wife, Ok Joo.
Without her dedication, none of this would have been possible.

ACKNOWLEDGEMENTS

I would like to express my sincere appreciation to many people whose help has made the work presented in this dissertation possible. First of all, I owe a debt of gratitude to my two excellent advisers, Prof. Iain D. Boyd and Prof. Michael Keidar, for their advice, direction, guidance, and support. Throughout the four years of my doctoral study, they has been my wonderful advisors and mentors with great patience and lavish support. Prof. Boyd has always been there to listen me, keen insight into the significance of my research and point out important things when I had difficulties in my research. He always helped me to overcome the obstacles in my research and taught me to be a excellent researcher. Prof. Keidar was the first person with whom I researched in the University of Michigan. He gave me an insight of the physics and many research opportunities. In the second year of my graduate study, he moved to George Washington University, but has committed himself to help me to accomplish my doctoral study. Without support of Prof. Boyd and Prof. Keidar, I probably would have graduated a few years ago but with a master's degree only. I am also deeply indebted to my dissertation committee members, Prof. Alec D. Gallimore, Prof. Brian E. Gilchrist, and Prof. Kenneth G. Powell, for their critical comments and suggestions on my thesis. Prof. Gallimore helped me by providing insight of the experiments. For a numerical researcher, this was very fortune for me because there are just few people which has experience of the experiment. Prof. Gilchrist also deeply supported my research and gave many precious advice on my

dissertation. Prof. Powell provided me an insight of numerical methods in magneto hydrodynamics and his suggestions were valuable for numerical issues in my doctoral research.

I would also like to thank my undergraduate advisor in the Seoul National University, Prof. Inseuck Jeung, my academic writing teacher, Prof. Christine Feak, and my plasma dynamics teacher, Prof. Mark J. Kushner. Prof. Inseuck Jeung was one of the greatest advisor in my academic career. He gave me an enthusiasm on aerospace engineering and provided a precious perspective to be an excellent engineer in aerospace engineering. Prof. Feak taught me how to write high-quality research papers and develop good academic communication skills. Prof. Kushner taught me a plasma physics to enhance my dissertation and gave me an eye for the phenomena of plasma. Their guidance is essential to the final completion of this dissertation and my Ph. D. training.

I am grateful to the U.S. Air Force and U.S. Department of Energy for their support during my doctoral work. Without their financial support, we will still have no method to solve radio blackout. I would like to extend my thanks to all the members of our laboratory, Anna, Hicham, Nick, Eunji, Andrew, Timothy, Tim, Erin, Cyril, Paul, Tyler, Adam, Jon, and Alex, for their contribution in the group meeting discussions and suggestions, and for sharing their research results, and experiences with me. My appreciation also goes to the people in the ElectroDynamic Applications (EDA) and the Plasmadynamics and Electric Propulsion Laboratory (PEPL) for their help to me in the experimental measurement and precious discussions in the re-entry communication. In particular, I would like to thank Kristina Lemmer, David Morris, Chris Davis, Joseph Mancuso, and Jonathan Zagel for their suggestions and experimental knowledge.

Many other people have helped me in their own unique ways toward the completion of this journey. I am very grateful to my officemate, Evan Fineda for inspiring discussions about the Finite Element Method and enjoyable conversations during my study. It has been a great pleasure to be with my Korean friends and their families. In particular, I am deeply indebted to Dr. Taeyoung Lee and Heylinm Woo for their invaluable suggestions and heartfelt advice throughout my graduate life at Ann Arbor. I would also like to thank my collage friends, Youngjin, Jinyong, Yongmin, Dongsung, Bongsung, Yongsul, Seunghan, and Kyunghwan for their friendship.

I owe greatly to my parents for their limitless help, unfathomable support and immeasurable sacrifices. Even several thousand miles away, they have always encouraged me to do my best and never failed to do what they could to support me to finish my doctoral study. My appreciation also goes to my parents-in-law who have been a source of much encouragement to complete my study. My sister, brother, brother-in-law and their families also deserve to receive my deep appreciation. I cannot finish my acknowledgement without mentioning my wife. I would like to share this accomplishment with my wife, Ok Joo, for her ceaseless encouragement, support and patience throughout my graduate study. I dedicate this dissertation to her as a small token of my eternal gratitude and to say to her, “My love for you can be stopped only when the world is ended. ”

TABLE OF CONTENTS

LIST OF FIGURES

Figure

LIST OF TABLES

Table

LIST OF NOMENCLATURE

Physical Constants

ϵ_o	Permittivity of free space, 8.8542×10^{-12} F/m
e	Elemental charge, 1.6022×10^{-19} C
k	Boltzmann constant, 1.3807×10^{-23} J/K

Acronyms

CFD	Computational Fluid Dynamics
EDA	ElectoDynamic Applications, Inc.
FEM	Finite Element Method
GPS	Global Positioning System
LeMANS	The Michigan Aerothermal Navier-Stokes Solver
MHD	MagnetoHydroDynamics
NGPDL	Nonequilibrium Gas and Plasma Dynamics Laboratory
OREX	Orbital Re-entry Experiment Vehicle
PEPL	Plasmadynamics and Electric Propulsion Laboratory

LIST OF APPENDICES

Appendix

CHAPTER I

Introduction

Radio blackout refers to a communication interruption during hypersonic or re-entry flight. When a vehicle enters the radio blackout phase, it loses all communication including GPS signals, data telemetry, and voice communication. Blackout occurs when the radio waves used for communication between ground stations and satellites are attenuated and/or reflected by the plasma layer that is created during hypersonic/re-entry flight. This phenomenon was well known at the beginning of space exploration when space capsule would experience several minutes of radio blackout during re-entry. Nearly 50 years later, hypersonic capsules still experience radio blackout during re-entry.

Radio blackout becomes an even more critical issue with development of hypersonic vehicles and the increase in Earth and Mars atmospheric entry missions. During such missions, the communication loss caused by radio blackout introduces significant problems related to the vehicle's safety; specifically, these include the possibility of catastrophe analysis, mission success, vehicle tracking and electric countermeasure capability [5, 6]. During the early 1960s and 1970s, much research was performed related to radio blackout [7, 8, 9, 10, 11] and during that time several approaches were suggested to solve it [6, 7]. However, most re-entry capsules and hypersonic

vehicles still experience several minutes of radio blackout.

One approach to solving the radio blackout problem would be to reduce the plasma number density of the plasma layer. Such an approach would be successful because radio wave transmission is possible at radio wave frequencies greater than the plasma frequency, which is related to the plasma number density of the plasma layer [7]. This approach is explored in this dissertation which proposes two mitigation approaches for re-entry communication blackout: an electrostatic sheath scheme and an electromagnetic (ExB layer) scheme.

The work presented in this dissertation was conducted in close collaboration with experimental work performed by ElectroDynamic Applications (EDA) and the Plasmadynamics and Electric Propulsion Laboratory (PEPL) at the University of Michigan.

1.1 Objective

The main purpose of this dissertation is to study a new mitigation scheme for re-entry blackout via numerical simulation in order to demonstrate the possibilities of the suggested schemes.

When a radio wave frequency becomes greater than the plasma frequency, radio wave transmission is possible. Since the plasma frequency is related to the plasma number density of the plasma layer, the manipulation of the plasma density is a useful method for solving the communication blackout problem. To manipulate the plasma density, this dissertation considers two schemes, one involving an electrostatic sheath and the other an electromagnetic or ExB layer.

This dissertation provides a series of models that were developed for the ExB layer and the electrostatic sheath, and compares these models to data obtained from

experiments that were conducted to explore the use of electric and magnetic fields to manipulate a plasma layer. The developed numerical models allow for the investigation of the detailed physics of the ExB layer and explore the effectiveness of the ExB layer as a mitigation scheme. The dissertation demonstrates that an applied ExB layer can manipulate plasma density in a localized region to reduce radio wave attenuation in a plasma layer, thus enabling communication during radio blackout.

1.2 Radio Blackout

Hypersonic re-entry and cruise vehicles, which can travel anywhere in the world within a few hours, experience communication and tracking difficulties during flight. These difficulties are known as communication or radio blackout. When radio blackout occurs, radio waves are reflected or attenuated against the plasma layer created around the vehicle. As a result of this effect, the radio waves emitted from the vehicle cannot reach a ground station or a Global Positioning System (GPS) satellite. Likewise the radio waves sent to the vehicle also cannot reach the vehicle, leading to a complete interruption of communications. The lost communications include [6, 12]:

1. Voice communication
2. Data telemetry
3. Vehicle tracking
4. GPS navigation
5. Electric countermeasures capability

Radio blackout blocks vehicle communications for between 4 and 16 minutes, depending on the angle of re-entry, the properties of the atmosphere, and the shape of

the vehicle [13]. For instance, the Mercury, Gemini, and Apollo capsules experienced radio blackout for several minutes, as do modern re-entry capsules. For example, the Soyuz TMA (Transport Modified Anthropometric) re-entry vehicle experiences about 10 minutes of radio blackout. Radio blackout also occurs whenever the vehicle enters a planetary atmosphere at hypersonic velocity. For instance, during Mars entry, the Mars Pathfinder experienced a 30-second radio blackout. For hypersonic vehicles, radio blackout is of special concern because continuous contact with ground stations and GPS satellites is required for communication and navigation.

During the last 50 years, a number of approaches have been suggested to solve the problem of radio blackout during re-entry or hypersonic flight. These include aerodynamic shaping, quenchant injection, higher communication frequencies, and Raman scattering [6, 7]. Because all of these suggested approaches have technical or practical limitations such as cost, system weight, and aerodynamic performance, they can only be applied in specific cases. For example, before 1989, Space Shuttles entered a radio blackout phase about 30 minutes before landing at the Kennedy Space Center [13]. In this specific instance, the radio blackout problem was solved by using NASA's Tracking and Data Relay Satellite (TDRS) system, but even the TDRS is not a general solution for the radio blackout problem. Since the TDRS requires the tail end of the vehicle to have less ionization than the front of the vehicle to provide a hole through which communication with the TDRS can be maintained, this approach cannot be used with ballistic re-entry vehicles where the enveloped the entire vehicle, or with powered air-breathing lifting vehicles.

1.2.1 Cause of Radio Blackout

When a vehicle flies at hypersonic velocity, a plasma layer is created as a direct consequence of the conversion of the kinetic energy of the vehicle into thermal and internal energy of the surrounding medium via a shock wave [14]. Within the shock wave, a plasma layer is formed when the temperature is high enough to excite the gas molecules' internal energy modes up to the point where dissociation and ionization reactions occur. The created plasma layer usually has an electron number density of 10^{17} to 10^{20} m^{-3} [14, 15], which may cause negative effects on a vehicle's operation, particularly for its communications, as stated earlier.

As a spacecraft enters an atmosphere, the effect of the charged particles generated by the heating of atmospheric gases will be a blackout of the signal if the resulting charged-particle density exceeds the plasma density at that frequency. For a given electron number density, the plasma frequency, in Hz, is expressed as

$$\begin{aligned} f_p &= \frac{\omega_e}{2\pi} \\ &= \frac{1}{2\pi}\sqrt{\frac{e^2 n_e}{\epsilon_0 m_e}} \\ &= 8.985 \times n_e^{1/2} \text{ Hz} \end{aligned} \tag{1.1}$$

where

$$\begin{aligned} n_e &= \text{electron number density in m}^{-3} \\ m_e &= \text{electron mass}, 9.1 \times 10^{-31}\text{kg} \\ \epsilon_0 &= \text{permittivity of free space}, 8.85 \times 10^{12} F/m^2 \\ e &= \text{electron charge}, 1.6 \times 10^{-19}\text{C} \end{aligned}$$

The signal will be attenuated for frequencies that fall below the plasma frequency and will be unaffected for frequencies that lie above the critical plasma frequency.

When the plasma frequency, f_p, of the plasma layer around a vehicle exceeds the radio wave frequency, f_{radio}, used for communication:

$$f_p > f_{radio} \tag{1.2}$$

the plasma layer reflects or attenuates the radio waves that are transmitted from or to a vehicle. The proximity of plasma to the antenna introduces a severe impedance mismatch that can dramatically weaken the signal power, reducing the channel capacity of the telemetry system and making voice communication impossible [10]. Therefore, communication is temporarily interrupted, which is known as radio or communication blackout.

1.2.2 Importance of Solving the Radio Blackout Problem

When the radio/communication blackout occurs, vehicles lose precise guidance and maneuvering initiated by a GPS satellite or control center. This loss is critical because the vehicles receive no guidance information from either source, thus compromising vehicle safety when it travels hundreds of miles during a few minutes of blackout. For example, the Soyuz TMA travels several thousand miles without guidance during its 10 minutes of blackout. Figure 1.1 provides the re-entry trajectory of Apollo which had a nearly 4-minute blackout period. As can be seen, Apollo flew almost 700 miles during the S-band radio blackout. This is particularly critical for safety because the blackout phase coincided with the maneuvering phase of the re-entry flight [10].

Radio blackout also makes pre or post catastrophe analysis impossible, eliminating a critical factor for understanding and preventing re-entry accidents. Data collected milliseconds prior to a catastrophe could be invaluable in determining its cause, especially at hypersonic velocities. In this case, continuous telemetry is abso-

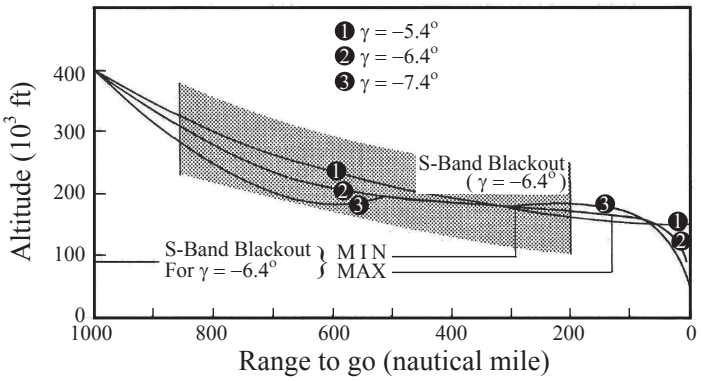

Figure 1.1: Apollo re-entry trajectory [10]

lutely critical because the velocities and altitudes involved imply that it is unlikely that onboard recorders would survive a crash or be found if they do survive after a disaster. In the space shuttle Columbia accident, for example, telemetry was lost prior to disintegration due to radio blackout. When the telemetry was recovered from the radio blackout, there was little available data at the ground station to assist in determining the cause of the disaster [16].

Besides catastrophic events, radio blackout plays a significant role in mission success. For an unmanned vehicle, a blackout results in a loss of control or guidance from a ground station. In this case, continuous and real-time telemetry determines whether the vehicle succeeds in a mission or not. For example, the Mars Pathfinder lost the 8.4GHz (X-band) communications link to Earth for a 30-second period [1]. The emitted signal frequency of 8.43 GHz was received in the one-way tracking mode at the NASA Deep Space Network (DSN) 70m antenna located in Madrid, Spain. The problem here was that this blackout phase coincided with the atmospheric entry phase. Since the vehicle tracking and precise guidance from control center are not possible, even a short blackout can affect the mission success. Although few serious disasters have occurred as a result of radio blackout, in order to ensure vehicle safety,

(a)

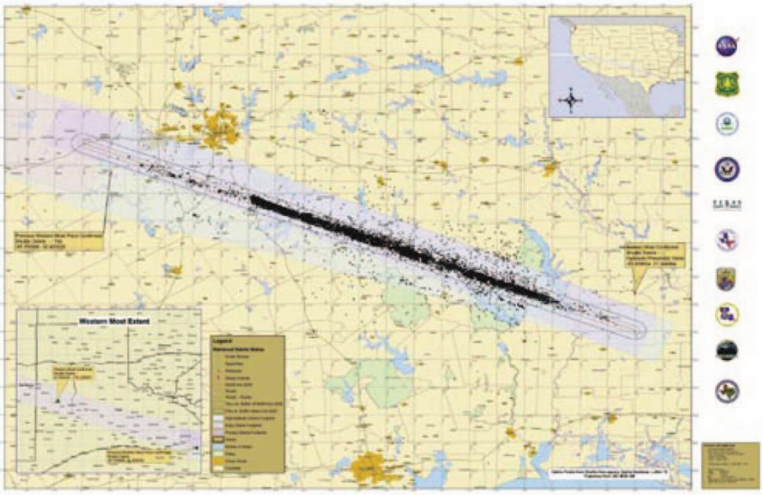

(b)

Figure 1.2: The space shuttle Columbia disaster [16]. (a) recovered debris. (b) the debris field in East Texas spread over 2,000 square miles.

complete data collection, and mission success, it is important to develop solutions that allow communication through a plasma layer.

1.3 Attenuation

This section provides common radio wave frequencies and evaluates radio wave attenuation in terms of plasma density. This part also describes the plasma density required to communicate through a plasma layer. The required plasma density helps to determine the configuration of the mitigation schemes that are presented in Chapters II and III. In this dissertation, the critical number density is defined as the electron number density that result in a plasma frequency that is the same as the radio wave frequency. When the plasma number density exceeds the critical number density, communications will be disrupted. Therefore, the critical number density is the minimum requirement for re-entry communication.

1.3.1 Radio Wavebands for Communication

A radio waveband is a small section of the spectrum of radio communication frequencies in which channels are usually used or set aside for the same purpose. The commonly used radio bands for communication include VHF (Very High Frequency), UHF (Ultra High Frequency), L-band, S-band, X-band, and K_a-band. Table 1.1 shows commonly used radio wave band frequencies and their applications [1, 2, 3].

When the plasma frequency becomes higher than the radio wave frequency, the radio wave signal suffers infinite signal attenuation. Thus, to transmit a radio wave signal in the plasma, the plasma frequency should be less than the radio wave frequency that is used in the communication. This requirement restricts the maximum plasma density of the plasma layer because the plasma frequency is related to the plasma number density. For a given communication frequency, f_{radio} in Hz, the criti-

Table 1.1: Commonly used radio wave frequencies and their applications [1, 2, 3]

Band name	Frequency GHz	Example uses
VHF	$0.03 \sim 0.3$	Voice communication
UHF	$0.3 \sim 3.0$	Data telemetry, Voice communication
L-band	$1.0 \sim 2.0$	GPS, Military telemetry
S-band	$2.0 \sim 4.0$	Data telemetry, TDRS
X-band	$8 \sim 12$	Data telemetry, Satellite communication
K_a-band	$27 \sim 40$	Radar and experimental communication

cal number density can be found for which communications will be interrupted when that critical number density is exceeded. Therefore, the critical number density can be obtained from 1.1 as:

$$n_{critical} = \left(\frac{f_{radio}}{8.985}\right)^2 \tag{1.3}$$

Table 1.2 shows the critical number densities for several common radio wave frequencies.

1.3.2 Signal Attenuation

The plasma layer may attenuate the radio wave even when the plasma number density is lower than the critical number density. In this case, radio wave attenuation depends on the transmission frequency, the electron collision frequency, and the plasma frequency which is related to the plasma number density. The electron collision frequency, the number of collisions per second that the electrons encounter with other species in the plasma, determines the degree of attenuation when the transmission frequency exceeds the plasma frequency. For a plasma with collision frequency, ν, radio wave attenuation can be expressed as [21]

Table 1.2: Common radio wave frequencies and their critical number densities with actual applications

Frequency GHz	Plasma density limitation m^{-3}	Designation
0.30	1.12×10^{15}	Apollo (Voice communication, UHF) [17]
0.92	1.06×10^{16}	Space Shuttle (Voice communication, UHF) [16]
1.55	2.99×10^{16}	GPS
1.68	3.52×10^{16}	OREX (Data telemetry, L-band) [18]
2.29	6.54×10^{16}	Apollo (Data telemetry, S-band) [19]
8.20	8.75×10^{17}	Mars Pathfinder (Data telemetry, X-band) [20]
32.0	1.27×10^{19}	Deep-space communication (K_a-band)

$$\kappa = 8.69 \frac{e^2}{2\epsilon_0 m_e c} \frac{1}{\mu} \frac{n_e \nu}{\omega_{radio}^2 + \nu^2} \text{ dB/m} \tag{1.4}$$

where, n_e is the plasma number density, c is the speed of light, ω_{radio} radio is the radio wave frequency that is used for the communication, ν is the plasma collision frequency, and μ is the refractive index, which is shown in Figure 1.3 in terms of the plasma angular frequency, ω_e and the collision frequency, ν.

Equation 1.4 can be simplified, because collision effects on wave propagation normally are not considered important for communication as [22]:

$$\kappa = \frac{54.6}{\lambda} \acute{k} \text{ dB/m} \tag{1.5}$$

where λ is the wave length of the radio wave and $\acute{k}$ is the extinction coefficient which is defined as [23]:

$$\acute{k} = \sqrt{\frac{f_p^2 - f_{radio}^2}{f_{radio}^2}} \tag{1.6}$$

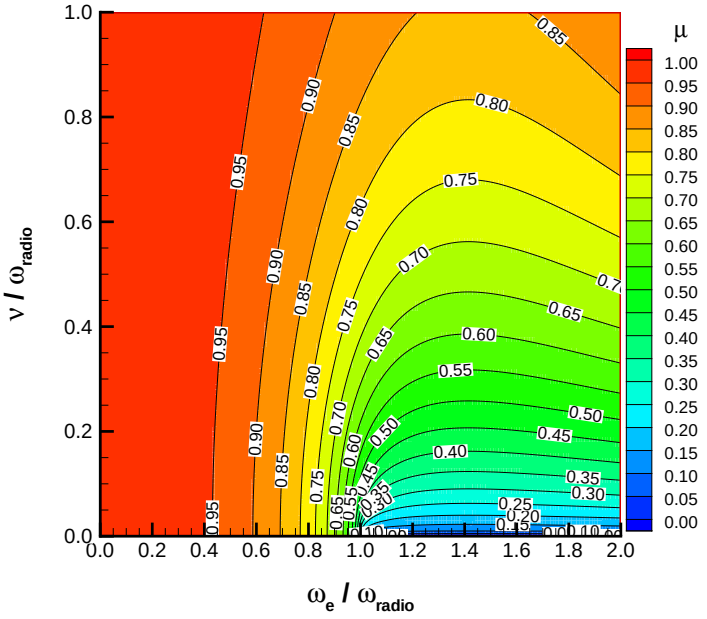

Figure 1.3: Refraction index variation with plasma frequency and collision frequency.

where f_p is the plasma frequency and f_{radio} is the radio wave frequency. From Equations 1.1, 1.5, and 1.6, the radio attenuation per unit length can be obtained in terms of the plasma density and the radio wave frequency as follows [23]:

$$\begin{aligned} \kappa &= \frac{54.6}{c}\sqrt{80.2547 \cdot n_e - f_{radio}} \\ &= 1.8213 \times 10^{-7}\sqrt{80.2547 \cdot n_e - f_{radio}}\ \text{dB/m} \end{aligned} \tag{1.7}$$

Signal attenuations per unit length are described in Figure 1.4. As can be seen, signal attenuation increases rapidly as the plasma number density reaches the critical number density for each radio waveband.

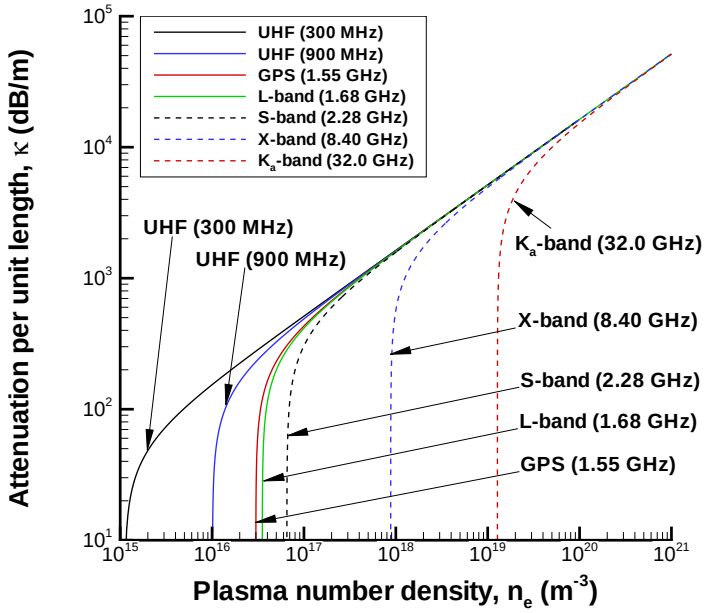

Figure 1.4: Signal attenuation along to the plasma density for several radio wave band.

1.4 Previous Approaches for Communication during Radio Blackout

During the last 50 years, a number of approaches have been suggested to solve the radio blackout problem during re-entry or hypersonic flight [5, 6, 7, 12]. The suggested approaches include aerodynamic shaping, quenchant injection, magnetic windows, high frequencies, and Raman scattering. However, because the suggested approaches have technical or practical limitations such as cost, system weight, and aerodynamic performance, they can only be applied in specific cases. This section reviews previous approaches for radio blackout mitigation and evaluates them in terms of realistic applications.

1.4.1 Aerodynamic shaping method: Remote Antenna Assemblies (RAA)

An aerodynamic shape can be used to control the plasma layer to eliminate or reduce radio blackout. For instance, a sharply pointed geometry is surrounded by a much thinner plasma layer and generates a weaker shock than that surrounding a blunted geometry. Experiments of sharp tipped conical reentry vehicles have demonstrated that at velocities as high as 6.3 km/s it is possible to enter and pass through the Earth's atmosphere without radio blackout [6, 24]. However, a sharply pointed re-entry vehicle has limitations due to a reduced payload capability and increased aerodynamic heating problems compared with blunted re-entry vehicles.

A blunted re-entry /hypersonic vehicle was considered by Belov *et al.* [24] who proposed the Remote Antenna Assemblies (RAA) method. Figure 1.5 shows the blunted re-entry vehicle with Remote Antenna Assemblies [24]. As can be seen, the RAA consists of a hooked cylinder that contains an antenna and has a sharp tip. During hypersonic flight, the antenna is placed ahead of the shock of the vehicle; in other words it is located outside the plasma layer. The plasma layer of a sharp tip is much thinner than that of the vehicle. Therefore, communication could be possible using RAA.

The main concern in this scheme is the maintenance of a sharp tip on the RAA. Belov *et al.* [24] suggested that a sharp tip on the RAA can be maintained by using a refractory metal tip or a transpiration-cooled tip. They experimentally demonstrated that it is possible to communicate through the plasma sheath using RAA [24]. However, many additional problems are created by the flow field interactions between different components of the RAA and also between the RAA and the vehicle. One of the main problems is the shock interactions with the vehicle surface, which requires the use of ablative material for both the antenna and the front of the

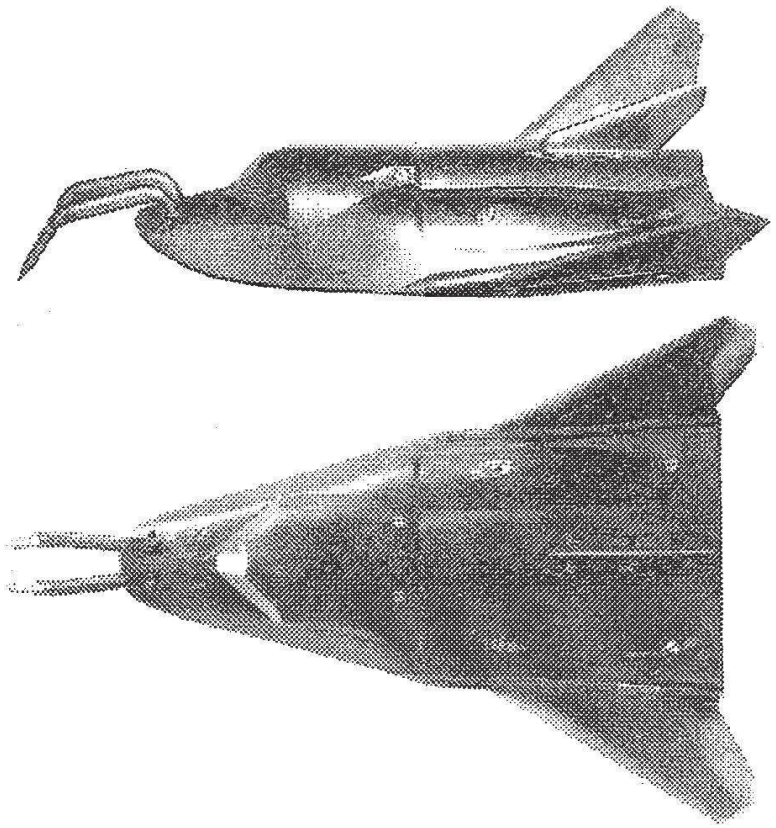

Figure 1.5: Photograph of the vehicle model with Remote Antenna Assemblies [24].

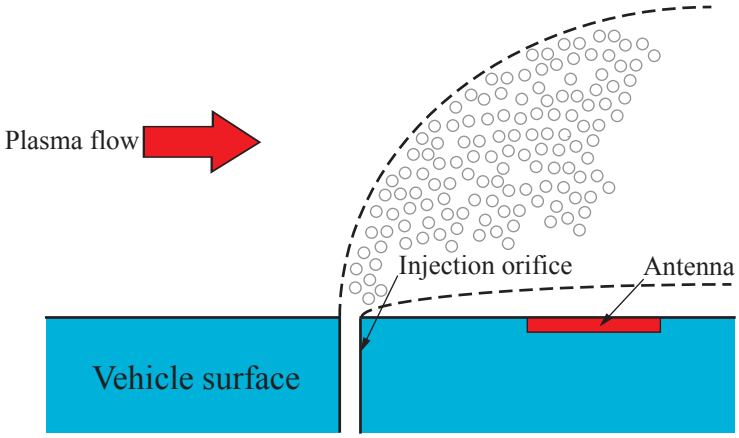

Figure 1.6: A schematic of the injection method

vehicle. The heating problem of the RAA also provides a technical limitation for realistic applications.

1.4.2 Injection of quenchants

Spencer proposed a liquid/gas injection method for blackout mitigation [23]. A schematic of this injection method is shown in Figure 1.6. As can be seen, quenchants, e.g. water, rhenum hexafluoride (ReF_6), sulphur hexafluoride (SF_6), Carbon tetrachloride (CCl_4)], and electrophilics, are injected into the plasma layer [6, 25, 26]. Injecting liquid/gas into the plasma layer affects the plasma number density by cooling the temperature of the plasma layer and consuming free electrons. When the plasma temperature is cooled by the injected quenchants, the balance of reaction rates is altered and shifted toward lower ionization. Since the quenchant molecules themselves become part of the flow species, they can consume free electrons through electron attachment processes. This process was experimentally shown to restore radio communication for reentry conditions [27, 28].

For the NASA RAM-C III flight, when pulses of water and alternately Freon E3 were injected into the flow, on-board sensors and ground station receivers clearly showed decreases in attenuation [29]. The mass flows of quenchant required for full recovery were of the order of 0.3 - 0.4 lb/sec at the most for this small vehicle. To alleviate 32 seconds of VHF blackout for that small vehicle, 12.8 lbs of Freon E3 would be required. However, the amount of quenchant mass needed for scale-up to large vehicles remains an issue [6].

1.4.3 Magnetic window

The magnetic window method, which uses a static magnetic field, has also been proposed to provide a window for communication [6, 30, 9, 11]. The presence of a static magnetic field alters the electrons' motion in the plane transverse to the applied magnetic field, thus introducing new propagation modes. When no interaction takes place between electrons and an electromagnetic plane wave whose wave front, a "spectral window" is opened through which a plane wave travels as if in vacuum [31].

Figure 1.7 shows a schematic of the magnetic window method. Russo and Hughes carried out experimental tests in the 1960s to measure the effects of a static magnetic field on VHF transmission [9]. In their experiment, an electromagnet was mounted behind the antenna and provided a magnetic field up to 0.75 T in a direction normal to the slot antenna and parallel to the transmission propagation direction. The result indicated that the calculated signal attenuation was reduced from 45 dB for zero-field to 28 dB at a 0.75 T magnetic field. A window was created below the plasma frequency, enabling radio waves to propagate with low attenuation. Rawhouser indicated that 1.3 T is required for an S-band signal frequency [11]. Usui *et al.* concluded

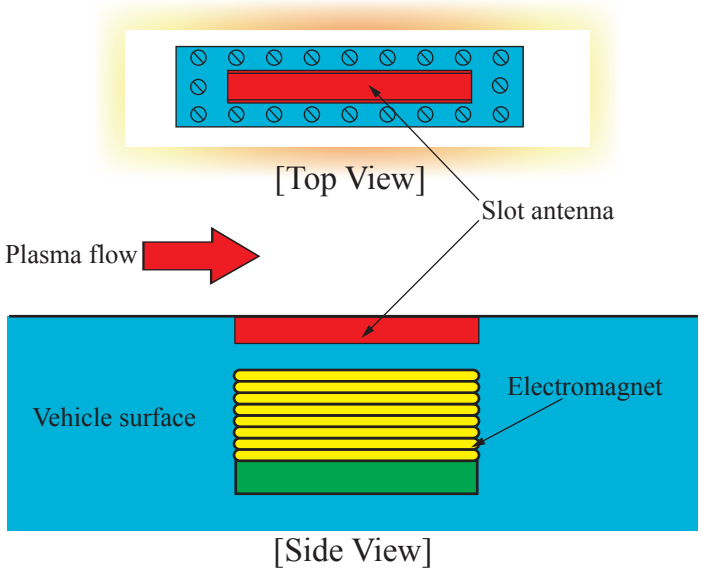

Figure 1.7: A schematic of the magnetic window method

from an analytical experiment that use of the Whistler mode, where the magnetic field cyclotron frequency equals the RF frequency, could provide a window for RF transmission using a 1.5 T magnetic field [32].

However, the size and weight of the electromagnet are obstacles to implementing the magnetic window method. Starkey *et al.* analyzed a hypothetical air-breathing vehicle with very blunt leading edges and calculated that a 1 T magnetic field is necessary to penetrate the created plasma layer using the magnetic window method [5, 30]. To provide a 1 T magnetic field, the total weight of the electromagnet system usually exceeds 500 kg [5, 6], even if the system uses lighter weight composite materials. In addition, the size of the electromagnet introduces a technical difficulty because the creation of a uniform magnetic field requires a very large coil radius. For example, a six feet diameter coil is required to provide a uniform magnetic field, with a uniformity of 10 percent along the axis in the space shuttle geometry [6]. However, no reasonable air-breathing vehicle will have leading-edge radii that large.

1.4.4 High-frequency transmission

As indicated in Section 1.3, the critical number density becomes higher as the radio wave frequency is increased. Therefore, increasing frequency can reduce the signal attenuation.

However, high-frequency transmission causes high attenuation due to the atmosphere and rain. For example, a satellite TV system, which operates at 14 GHz, loses synchronization when rain cells pass by, thus causing a perfect picture to become a blank screen. As a practical limit, the communication frequency should be below about 10 GHz [6].

1.4.5 Raman Scattering process

Nazarenko *et al.* suggested a communication method through a plasma layer via a Raman scattering process [33]. The idea behind the Raman Scattering process is to place a source of an intensive, high frequency electromagnetic pump wave on the vehicle and to use the nonlinearity of the medium to create a backscattered Stokes wave through the interaction of the pump wave with the signal-carrying wave sent by a ground transmitter.

However, this method has several severe limitations, such as collisional damping, sensitivity to plasma parameter non-uniformities, and very short range of resonance for three-wave interactions [6].

1.5 Thesis Overview

In this dissertation, two mitigation schemes for communication blackout are presented and evaluated as possible reentry mitigation schemes. The road map of the dissertation is summarized in Figure 1.8.

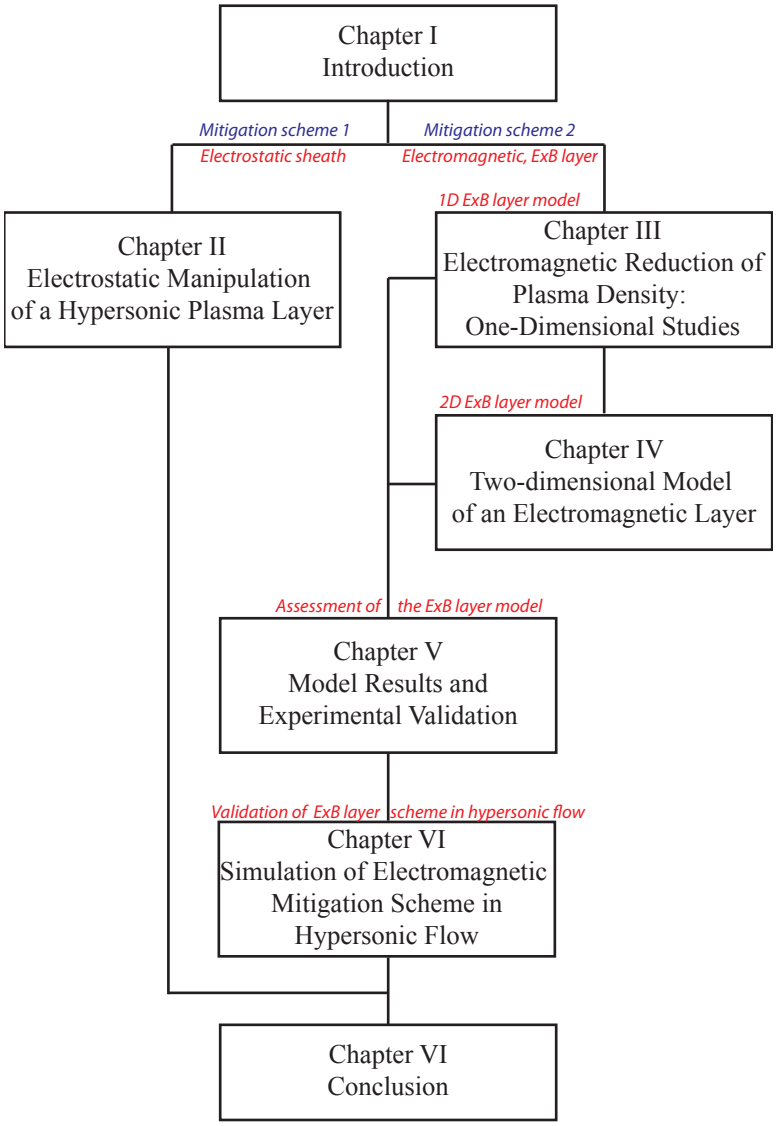

Figure 1.8: A road map of the dissertation

Chapter I introduced and evaluated radio blackout, signal attenuation and previous approaches for communication during radio blackout. The motivation for solving the radio blackout problem was discussed in terms of real world examples. To provide insights into reentry communication, common radio wave bands were described and the critical number density for communication and signal attenuations were evaluated for each radio wave band along with the plasma density. This provided a required plasma density for reentry telemetry. Previous approaches to solve the radio blackout problem were explained and these methods evaluated in terms of technical limitations.

Chapter II describes modeling and simulation of an electrostatic sheath as a mitigation scheme during radio blackout. Also discussed in the chapter are an overview of the electrostatic sheath, mathematical modeling of the plasma sheath, followed by the simulation results of the two-dimensional electrode system. The suggested mitigation scheme is based on the formation of an electron-depleted sheath with a scale length comparable to the plasma layer. As a mitigation scheme, the sheath thickness is important because the created sheath should be large enough to penetrate the plasma layer around the vehicle and to contain the transmit/receive antenna. To maximize the sheath thickness, this chapter suggests two-dimensional shaped electrodes, a U-shaped electrode and a cylindrically shaped electrode. Simulation results of the two-dimensional electrode system are presented and discussed in terms of the possible mitigation scheme.

Chapter III presents a plasma manipulation scheme using an electromagnetic, ExB layer. This chapter mainly focuses on a one-dimensional analysis of the ExB layer with different operating conditions. The chapter also provides an overview of the ExB layer mitigation scheme, an analysis of hypersonic flow, the one-dimensional

ExB layer model, followed by the simulation results of the ExB layer for different operating conditions. The suggested mitigation scheme is an improved magnetic window method which was introduced in Chapter I and the technical limitations of the magnetic window method are presented. The proposed ExB layer is described by a hydrodynamic plasma model with two approximations, namely the plasma-optic and MHD limits. Numerical results of the ExB layer are presented to optimize the configuration of the ExB layer and its possibility as a mitigation approach is discussed.

Chapter IV proposes a two-dimensional ExB layer model and demonstrates the possibility of the ExB layer as a blackout mitigation scheme. The two-dimensional approach is important because it shows the optimal location of the transmit antenna and the effective area of the ExB layer. This chapter uses two different potential distribution models to calculate the potential: the thermalized potential model and a Poisson-like model. The effectiveness of the ExB layer is discussed in terms of the magnetic and electric fields strength. Simulation results are provided and discussed.

Chapter V assesses the ExB layer model that is presented in Chapters III and IV using an analytical solution and experiment results. Experimental study of the ExB layer mitigation scheme was carried out by ElectroDynamic Applications (EDA) in the Plasmadynamics and Electric Propulsion Laboratory (PEPL) at the University of Michigan. This chapter presents a comparison of the one-dimensional ExB layer model and the two-dimensional model in order to demonstrate the consistency of the ExB layer model. Results of comparisons are provided and discussed.

To evaluate the ExB layer mitigation scheme in a realistic operating condition, Chapter VI discusses the simulation of the ExB layer mitigation scheme in a hypersonic flow for the OREX reentry vehicle. This chapter includes a description of the

mathematical model for simulation which is composed of two parts: the flow field and electric field. The flow field equations are the Navier-Stokes equations and are solved numerically using a hypersonic CFD code. For the electric field equation, this chapter describes a finite element method (FEM) for solving the Poisson equation. Simulation results are presented and the effectiveness of the ExB layer is expressed in terms of radio wave attenuation. This chapter also discusses the possible configurations of an ExB layer to solve radio blackout for S-band, L-band, and GPS communications during reentry flight.

Chapter VII summarizes all conclusions from prior chapters. A clear statement is made in Section 7.2 as to the work presented in this thesis that is original and new, representing the contributions made to the blackout mitigation research. In brief, the major contributions to the field include: the suggestion of two possible mitigation schemes, the electrostatic sheath and the electromagnetic layer; the development of the one-dimensional and two-dimensional ExB layer models for optimizing the ExB layer configuration; simulations demonstrating the effectiveness of the suggested mitigation schemes; the assessment of the suggested ExB layer model in terms of analytical solution and experimental measurement; and the demonstration of the possibility of the ExB layer as a blackout mitigation scheme for the OREX reentry vehicle and suggestions of possible ExB layer configurations for L-band and GPS communication during reentry. The chapter ends with suggestions for future areas of research in the field of magneto hydrodynamics.

Appendix A contains a detailed derivation of an analytical solution for the one-dimensional ExB layer. The derivation of the thermalized potential equation is presented in Appendix B. Appendix C provides the detailed derivation of the electrical conductivity tensor.

CHAPTER II

Electrostatic Manipulation of a Hypersonic Plasma Layer

This chapter describes modeling and simulation of an electrostatic sheath as a mitigation scheme during radio blackout. In order to use the electrostatic sheath as a mitigation scheme, the size of the sheath is critical [12, 34] because it must penetrate the plasma layer around the vehicle. Since the size of the plasma sheath is proportional to the applied voltage, this chapter focuses mainly on a high-voltage plasma sheath as a mitigation scheme. For a high applied voltage, the sheath size of the electrostatic layer can be many times the Debye length of the plasma because the applied voltage is many orders of magnitude greater than the electron temperature [35]. Therefore, the high-voltage plasma sheath will be large enough to solve the radio blackout problem. Also discussed in the chapter are an overview of the electrostatic sheath, mathematical modeling of the plasma sheath, followed by the simulation results of the two-dimensional electrode system. The chapter concludes by discussing the possibility of an electrostatic sheath approach for communication during radio blackout. Some of the results presented in this chapter were first reported in [36].

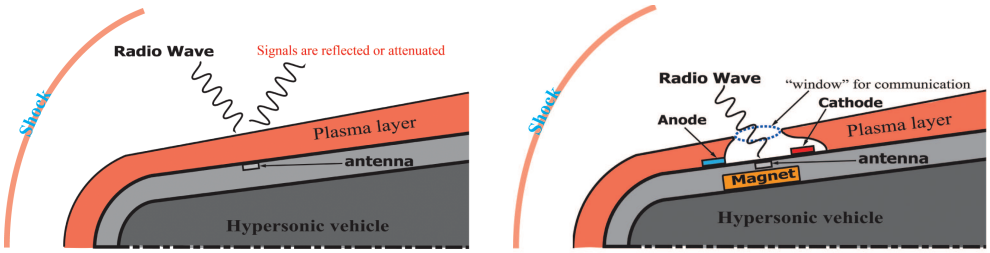

(a) (b)

Figure 2.1: (a) A schematic of a hypersonic vehicle showing the plasma layer around the vehicle. In this case, the radio waves are reflected or attenuated against the plasma layer (b) A schematic of a hypersonic vehicle including a mitigation scheme. The plasma sheath creates a " window " for communication through the plasma layer.

2.1 Overview of the Electrostatic Sheath

When a negative voltage is applied to a cathode in a plasma, electrons are repelled from the cathode. This causes an area of almost zero electron number density to form near the cathode. This electron depleted area is known as a plasma sheath. Since electrons rather than ions primarily interact only with electromagnetic waves [34], the sheath provides a possible solution to the communication blackout problem that occurs for a re-entry vehicle, in hypersonic flight. In the plasma sheath, ions are still present, but they do not affect radio wave attenuation, thus allowing the sheath to act as a passage to transmit radio waves. As illustrated in Figure 2.1, the plasma sheath can be a "window" for communication, through which radio waves can reach and leave an antenna of the vehicle.

In this electrostatic sheath approach, the size of the "window" is important in solving the radio blackout problem. In order for the electrostatic mitigation scheme to work, the created "window" must extend over the vehicle surface up to the peak of the plasma density. Further, in order to achieve efficient communication, the "window" also should cover the physical size of the transmission and/or reception

antennae. Since the size of the created "window" is determined by the plasma sheath thickness, estimating the sheath thickness is important to determine the potential possibility of this approach.

In the one-dimensional steady state case, the sheath thickness can be estimated according to the Child-Langmuir law [37, 38],

$$s = \left(\frac{4}{9}\epsilon_0\right)^{1/2} \left(\frac{2Z_i e}{m_i}\right)^{1/4} \frac{U^{3/4}}{(eZ_i nV)^{1/2}}, \tag{2.1}$$

where V is the ion velocity at the sheath edge, U is the voltage across the sheath, s is the sheath thickness, ϵ_0 is the permittivity of vacuum, Z_i is the ion mean charge number, n is the plasma density at the sheath edge, and m_i is the ion mass. This law demonstrates that the steady-state sheath thickness is determined by plasma density and ion velocity at the sheath edge for a given bias voltage.

The calculated sheath thickness is shown in Figure 2.2 as a function of the applied voltage with plasma density as a parameter. In order for the plasma sheath to be used as a mitigation scheme, the sheath thickness should be several centimeters because of the thickness of the plasma layer and the size of the transmit/reception antenna. Figure 2.2 shows that a high voltage is required to create a large sheath. For example, a plasma with a number density of 10^{18} m^{-3} requires about 7 kV voltage to generate an approximately 2 cm thick sheath. This is enough to solve the GPS communication blackout for a re-entry vehicle because a typical GPS transmit antenna is about 1 cm and the plasma layer of the RAM-C test vehicle was about 2$\sim$3 cm [14, 15].

However, one challenge is that the formation of the high-voltage sheath near the cathode can cause breakdown because the resulting E/N, where E is the electric field and N is the ion number density, which is the scaling parameter for electric fields in low-temperature plasmas, is quite high [39]. This problem can be solved using an ap-

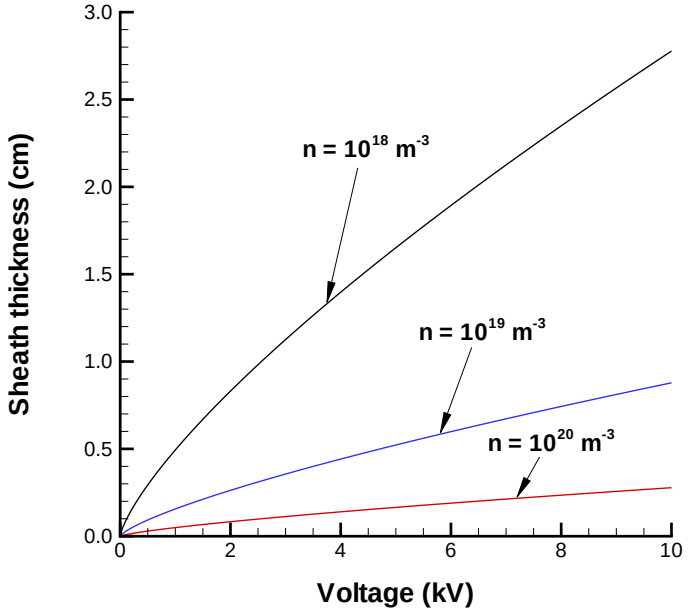

Figure 2.2: Thickness of the electrostatic sheath with plasma density as a parameter

plied magnetic field that leads to high-voltage sheath stabilization [40]. Experimental results demonstrated that a voltage up to 8 kV can be maintained across the sheath [40]. Thus, the magnetic field plays an important role in creating proper conditions for high-voltage sheath formation in contrast to previously described effects.

For a practical application, the applied voltage should be limited because of the arc problem between two electrodes. Thus, it is necessary to increase the sheath thickness without increasing the applied voltage. To maximize the sheath thickness, a two-dimensional shaped electrode system can be employed. Unfortunately, simple analytic expressions for the two-dimensional sheath are not available, and it must be analyzed through the simultaneous solution of the Poisson equation and the sheath equations using numerical methods [41].

2.2 Mathematical Modeling of the Plasma Sheath

The Child-Langmuir law, Eq. 2.1, is valid only for a one-dimensional or plate electrode. Thus, it is impossible to use this law to calculate the sheath thickness of a two-dimensional shaped electrode. For a two-dimensional case, the electrostatic sheath thickness should be estimated by numerically solving the sheath equations [41]. In this chapter, a steady state two-dimensional fluid sheath model is employed to simulate the two-dimensional electrostatic sheath which is based on a hydrodynamic description for ions.

The fluid sheath model essentially consists of ion transport equations and potential equations. The ion transport equations consist of the mass and momentum equations. In the momentum equation, ions are accelerated by an electric field. The electric field is created by applying a voltage between two electrodes, an anode and a cathode. The magnetic field is applied to stabilize the high-voltage plasma sheath. A magnetic field of a few hundred gauss is enough to sustain a strong electric field [40]. However, the considered magnetic field strength is well below the magnitude required for ion magnetization. Therefore, in the steady state, the ions are accelerated toward the negative electrode by the electric field of the sheath without any effect of the magnetic field.

The sheath model makes three main assumptions in order to describe the collisional sheath [42]. The first is that the sheath has a uniform background neutral density and the ions are cold. The uniform background neutral density introduces collision drag terms into the two-dimensional fluid sheath model. Because of the cold ion assumption the ion pressure term of the ion momentum equation is negligible [43]. Second, it is assumed that the electrons satisfy the Boltzmann relation in the

sheath, which can be then coupled with Poisson's equation to calculate the electric potential. Finally, the effect of secondary electrons on sheath formation is assumed to be negligible because the secondary electrons are rapidly accelerated back into the pre-sheath regime. Therefore, the steady state two-dimensional collisional sheath can be described by:

$$\nabla \cdot (n_i V_i) = 0 \tag{2.2}$$

$$m_i \nabla \cdot (n_i V_i V_i) = enE + \nu_c m_i n_i V_i \tag{2.3}$$

$$n_e = n_0 \exp\left(\frac{e\phi}{kT_e}\right) \tag{2.4}$$

$$\nabla^2 \phi = -\frac{e}{\epsilon_0}(n_i - n_e) \tag{2.5}$$

where ν_c is the ion collisional frequency and n_0 is the electron density of the bulk plasma. The electron temperature T_e is assumed a constant because it is small compared to the applied voltage.

Equations 2.2 - 2.5 are solved numerically with an iterative scheme. The ion transport equations, Eqs. 2.2 and 2.3, are solved by a finite volume method with the HLLC (Harten-Lax-van Leer contact wave) Riemann solver [44] and gives the ion number densities and velocities. The obtained ion number density makes it possible to calculate the electron number densities via the Boltzmann relation, Eq. 2.4. Then a new potential distribution is calculated by solving Poisson's equation, Eq. 2.5, with the alternating direction implicit (ADI) method. The calculated new potential distribution gives a new electric field for the next iteration step. After

a sufficient number of iterations, a steady state solution is obtained with sufficient accuracy.

In the collisional electrostatic plasma sheath regime, the initial ion flow velocity is not known, but it will be at or below the Bohm velocity[45, 46, 47]. This classical condition for the sheath formation is applicable for an electrostatic sheath case. Since the formation of the electrostatic layer is considered in the boundary layer of the hypersonic flow field, the velocity of the boundary layer is small and typically smaller than the Bohm velocity [34]. Thus, the simulation uses 1000 m/s as the initial ion flow velocity, and the ion and neutral number densities of the undisturbed plasma correspond to a hypersonic flow field calculated using a particle simulation technique [12].

Figure 2.3 shows the sheath thickness of a flat plate electrode computed by using the fluid sheath model. The fluid sheath model has good agreement with the Child-Langmuir law and experimental data. The model usually predicts a larger sheath thickness than the experimental result because the Bohm sheath criterion is used for the initial ion velocity. Under this criterion, the ions can enter the sheath with supersonic speed in a vacuum condition [40]. The initial ion velocity in the experimental case can be somewhat higher than the Bohm sheath criterion.

2.3 Simulation Result for the Two-dimensional Electrodes

The main issue of the electrostatic sheath method is the sheath thickness, which should be larger than that of the transmission and/or reception antennae and extend across the plasma layer of the vehicle. The two-dimensional electrode system can create a larger sheath than a flat plate electrode. Since the sheath thickness should be maximized to solve radio blackout, the two-dimensional electrode system is em-

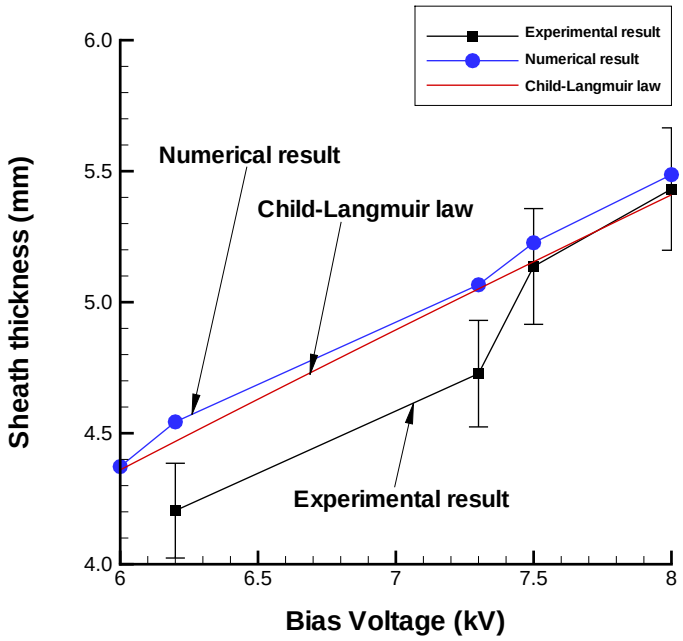

Figure 2.3: Sheath thickness as a function of the applied bias, experiment [40], numerical, and Child-Langmuir results

ployed.Two different types of electrodes are considered in this chapter: a U-shaped electrode and a cylindrically shaped electrode. The geometries of these electrodes are shown schematically in Figure 2.4.

The U-shaped electrode consists of a flat plate anode and U-shaped cathode. It is expected that the maximum sheath thickness is formed near the corner of the U-shaped cathode. This region will be the optimal location of the transmit/reception antenna for mitigation. The cylindrically shaped electrode consists of a hollow anode and cylindrical cathode. A dielectric material is located between the anode and cathode in order to prevent an arcing problem. In this system, the sheath is formed in front of the cathode and has a maximum thickness at the center of the cathode. Therefore, the transmit/reception antenna should be located in the center-line of the cylindrical cathode.

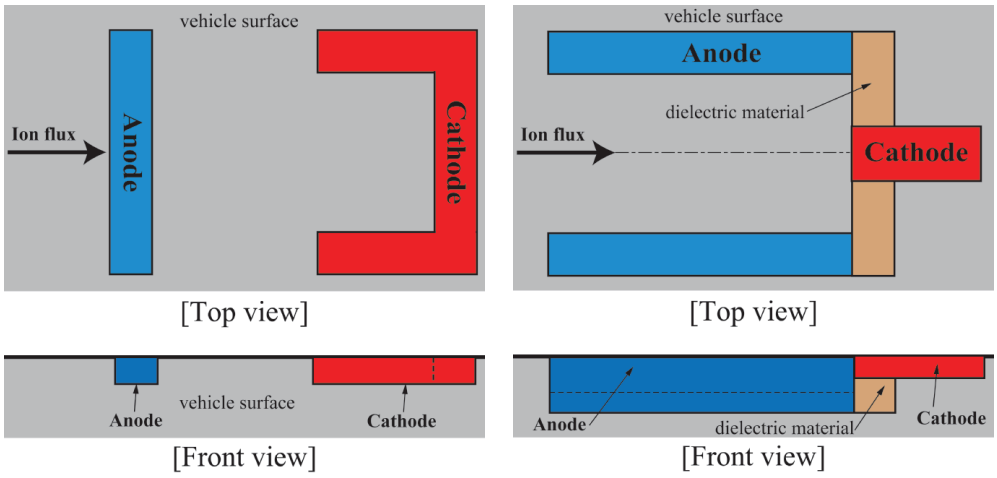

Figure 2.4: Schematics of the two-dimensional electrodes: (a) the U-shaped two-dimensional electrode. (b) the cylindrically shaped two-dimensional electrode.

The suggested two-dimensional electrode systems are simulated in a molecular-nitrogen plasma. The simulation uses 3 mTorr neutral pressure and 10^{18} m^{-3} bulk electron number density, which corresponds to the electron number density of the RAM-C II simulation result [14] at 81 km altitude. Since the RAM-C re-entry vehicle experienced radio blackout at 81 km [29], the initial conditions are useful to show the possibility of using the two-dimensional electrodes as a mitigation scheme.

A -1000 V potential drop is applied between the anode and the cathode. Since the anode sheath is not considered in this simulation, the anode is biased as 0 V. The applied potential drop is large compared with the electron temperature so the electron temperature can be assumed constant as 1.5 eV, which is the maximum electron temperature of the RAM-C flight test [48, 49]. Since a higher electron temperature gives a thinner sheath thickness [50], the applied electron temperature introduces the worst scenario for the electrostatic mitigation scheme.

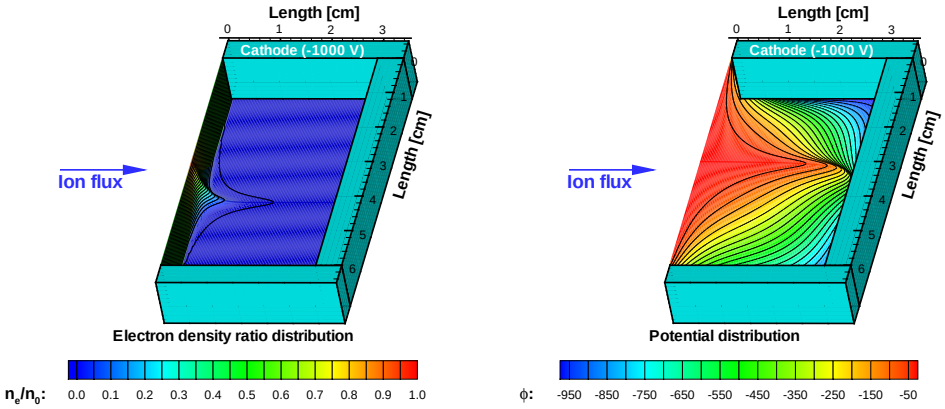

(a) (b)

Figure 2.5: Potential and electron number density distributions of the U-shaped electrode including a schematic of the electrodes. The bulk plasma density n_0 is 10^{18} m^{-3}, and the neutral background density n_n is 10^{20} m^{-3}. The cathode is at -1000 V potential

2.3.1 The U Shaped Electrode

The calculated distribution of the electron number density and potential in the U shaped electrodes is shown in Figure 2.5 where the electron densities are normalized by the bulk electron density n_0. The U-shaped electrode creates a sheath thickness of about 3 cm. Using the same conditions as those employed for the U-shaped electrode, Eq. 2.1 gives a sheath thickness of about 0.5 cm, which is almost a factor of six smaller than the result from the two-dimensional simulation. The sheath thickness calculated from Eq. 2.1 is for a flat plate electrode. Therefore, Figure 2.5 demonstrates the U-shaped electrode can more effectively increase the sheath thickness than a flat plate electrode.

Figure 2.5 shows that the maximum sheath thickness is found near the corner of the U-shaped electrode. This indicates the optimal location of the transmit/reception antenna because this location provides the largest "window" for communication. Therefore, the required voltage drop between the two electrodes can be determined

based on the size of the antenna. A higher applied voltage will give a larger sheath for mitigation, but it can cause a technical problem, known as arcing. When high voltage is applied to the two electrodes, an arc can form and melt the electrodes. The formation of an arc depends on applied voltage, background pressure, distance between the two electrodes, and the rate of ionization [51]. In the U-shaped electrode system, the distance between the two electrodes is not important to determine the formation of an arc because 0 V is applied at the anode. The applied voltage and the rate of ionization mainly determine the arc formation. When an arc is formed, it can be found at the edge of a cathode [52]. Since the configuration of the cathode has several edges, the U-shaped electrode system will not work for a high-voltage condition that is high enough to cause an arcing problem.

The U-shaped electrode is appropriate for low-frequency radio wave mitigation. In order to communicate via a low-frequency radio wave, a high plasma density reduction is required because the plasma density limitation is low for a low frequency radio wave such as UHF, which is used in voice communication. Since the sheath has almost zero electron number density, the plasma density reduction ratio of the U-shaped electrode is much stronger than that of the other plasma manipulation mitigation schemes.

2.3.2 The Cylindrically Shaped Electrode

The cylindrically shaped electrode is technically more feasible than the U-shaped electrode because it can avoid an arcing problem by removing the edge of a cathode. The geometry of the cylindrically shaped electrodes includes a 3-cm-radius anode of 10-cm-length and a 0.5-cm-radius cathode as shown in Figure 2.4(b).

The calculated distribution of the electron number density and potential in the

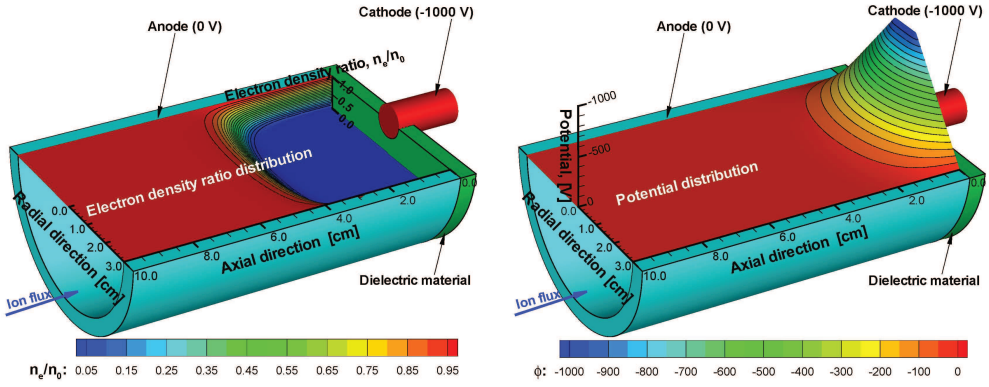

(a) (b)

Figure 2.6: Potential and electron number density distributions of the cylindrically shaped electrodes including a schematic of the electrodes. The bulk plasma density n_0 is 10^{18} m^{-3} and the neutral background density n_n is 10^{20} m^{-3}. The cathode is at -1000 V potential.

cylindrically shaped electrodes is shown in Figure 2.6. The electron number densities are normalized by the bulk electron density n_0, which indicates the plasma density ratio. The electron number density distribution shows the depleted region, the "sheath", near the central electrode. The sheath region in Figure 2.6 extends up to approximately 4 cm over the dielectric surface material. This may satisfy the requirement of affecting the plasma density peak with a stand-off distance of several cm [15, 14]. In this case, the required power is about 66 W.

The radial size of the sheath can be estimated from Figure 2.7, which shows two different anode length conditions of 3.5 cm and 2.5 cm. The 2.5 cm anode produces a sheath having a radius of about 2.5 cm, which can be considered large enough to solve the communication blackout problem. The 3.5 cm anode shows a sheath having a radius of about 1.2 cm, which is comparable to the size of a typical GPS antenna and thus may give a possibility to communicate through the plasma layer.

As demonstrated in Figure 2.8, the cylindrically shaped electrode provides the largest sheath thickness under the same operating condition. For GPS communica-

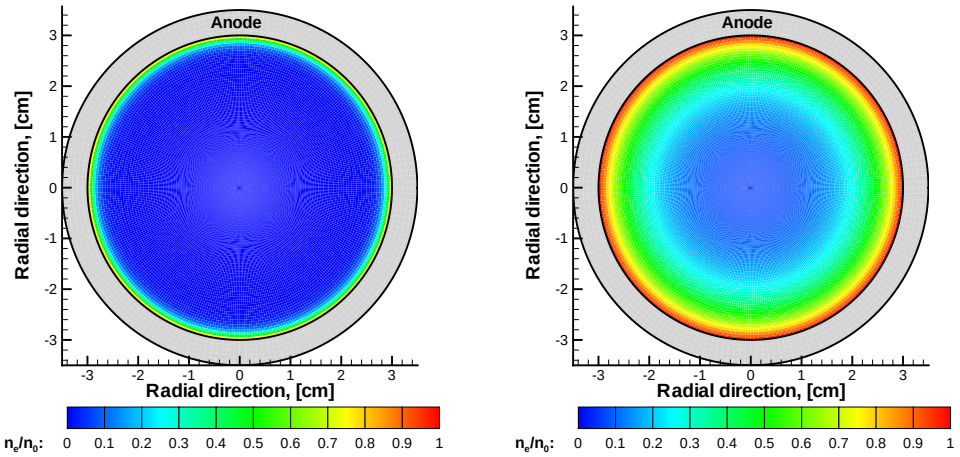

(a) (b)

Figure 2.7: The electron number density is normalized by the bulk number density n_0, which is 10^{18} m^{-3}, and the neutral pressure is 3 mtorr. (a)Electron number density distribution for a cross section at 2.5 cm axial position. (b)Electron number density distribution for a cross section at 3.5 cm axial position.

tion, both the U-shaped and the cylindrically shaped electrodes provide a sufficient size of the electrostatic sheath for the GPS antenna. The cylindrically shaped electrode with a 2.5 cm anode provides almost the same size sheath as a typical data telemetry antenna. However, this size is still small compared with VHF antenna, which is about 8 cm in size.

2.4 Conclusion

Two-dimensional shaped electrodes were investigated as a mitigation scheme for radio blackout. This mitigation scheme is based on the formation of an electron-depleted sheath with the scale length comparable to the plasma layer. In addition, for efficient communication, the sheath region should be larger than the physical size of the antenna. The electron depleted region of the two- dimensional electrode system is simulated by using a two-dimensional fluid sheath model. To estimate the

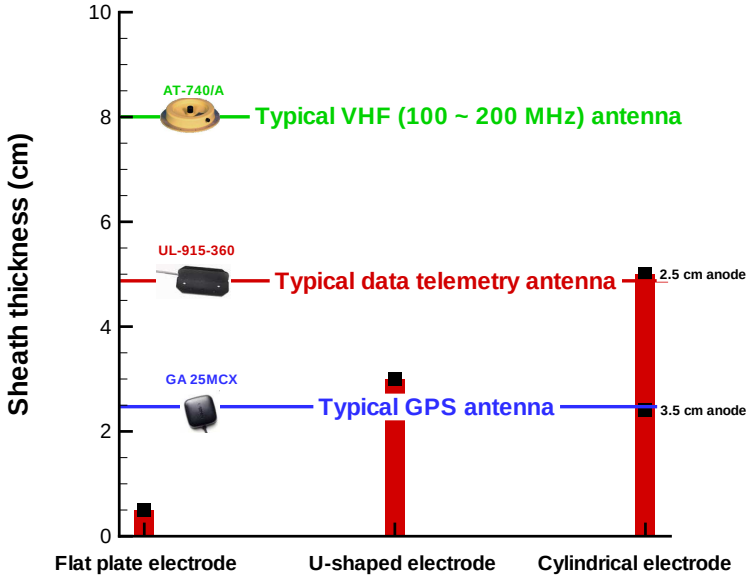

Figure 2.8: The sheath thickness of several shape electrodes which are plate, U-shaped, and cylindrically shaped electrodes with typical size of antennas for aviation, data telemetry, and GPS communication

size of the plasma sheath, the electron number density and the potential distribution near the two-dimensional electrodes are presented. The simulation result shows that the two-dimensional shaped electrodes create a thicker sheath than is possible with a plate electrode under the same voltage condition. When the size of the electrostatic sheath becomes comparable to the size of the transmission antenna, transmission through the plasma layer may be possible during radio blackout. The two-dimensional electrode system is an efficient way of increasing the sheath thickness under a fixed voltage condition.

The electrostatic mitigation scheme has unique advantages compared with other mitigation approaches. Other mitigation schemes based on plasma manipulation present have difficulties in solving a low-frequency radio blackout problem such as voice communication because it is difficult to sufficiently deplete electrons. However,

the sheath region of the electrostatic mitigation scheme has almost no electrons.

As mentioned before, the sheath thickness is also affected by the plasma density. Thus, reducing the plasma density can enlarge the sheath thickness. The plasma density can be significantly reduced by using an electromagnetic, ExB layer, which is discussed in the next chapter. When an ExB layer is applied to a two-dimensional shaped electrode system, the size of the electrostatic sheath will be maximized. Consequently, the possibility of communication during radio blackout will be maximized by a combination of an ExB layer and the two-dimensional shaped electrode.

CHAPTER III

Electromagnetic Reduction of Plasma Density: One-Dimensional Studies

This chapter presents a plasma manipulation scheme using an electromagnetic, ExB layer. As a mitigation scheme, the applied ExB layer can effectively reduce the plasma density in the plasma layer that is created around the hypersonic/re-entry vehicle. For re-entry communication, the plasma number density should be manipulated below the critical density, which depends on the radio wave frequency [5, 7, 12, 34]. In this case, the manipulated plasma density depends on the configuration of the ExB layer, which can be optimized by using a hydrodynamic fluid plasma model. The ExB layer model is simplified with two different approximations, which are the plasma-optic and MHD regimes. The two regimes are investigated with numerical and analytical approaches. This chapter focuses on a one-dimensional analysis of the ExB layer at different operating conditions. The effects of the altitude, magnetic field, and current density are studied and indicate a possible configuration of the ExB layer that solves the radio blackout problem. Most of the results presented in this chapter were first reported in [12, 53].

3.1 Overview of an ExB Layer Manipulation Scheme

As a mitigation scheme, the magnetic window method is the most promising approach to solve the radio blackout problem [6]. In fact, theoretical study and experimental data suggest that magnetic field mitigation of radio blackout may be viable [9, 11]. The magnetic window method however, requires a strong magnetic field to create a sufficient magnetic window for communication. Rawhouser found that the magnetic window method requires a 1.3 T magnetic field for S-band signal communication, which is used for the data telemetry of the RAM-C test vehicle. The electron number density was about 10^{18} m^{-3} at an altitude of 81 km for the vehicle [11]. Compared with a 1 T magnetic field, which is required for lifting a car using an electromagnetic crane, the 1.3 T magnetic field is extremely high for a re-entry or hypersonic cruise vehicle. Actually, the 1.3 T magnetic field is almost the same strength as that required in a magnetic resonance imaging (MRI) machine.

The problem of the magnetic window method is the weight of the magnet needed to produce a strong enough "magnetic window" for communication during radio blackout. As demonstrated in Figure 3.1, a higher magnetic field requires a heavier total system weight. This weight includes the electromagnet coil, cooling system, and power supply. The extra system weight is required to produce the high amount of current needed to generate a higher magnetic field. Since the high electric current also creates a large amount of heat in the electromagnet coil, the weight of the cooling system also increases. For instance, the weight needed to generate a 1.3 T magnetic field is on the order of 1000 kg, which is extremely heavy for a re-entry vehicle when we consider that the approximate weight of the OREX vehicle was 761 kg. Since this required electromagnet weight is unacceptable for a re-entry or hypersonic cruise

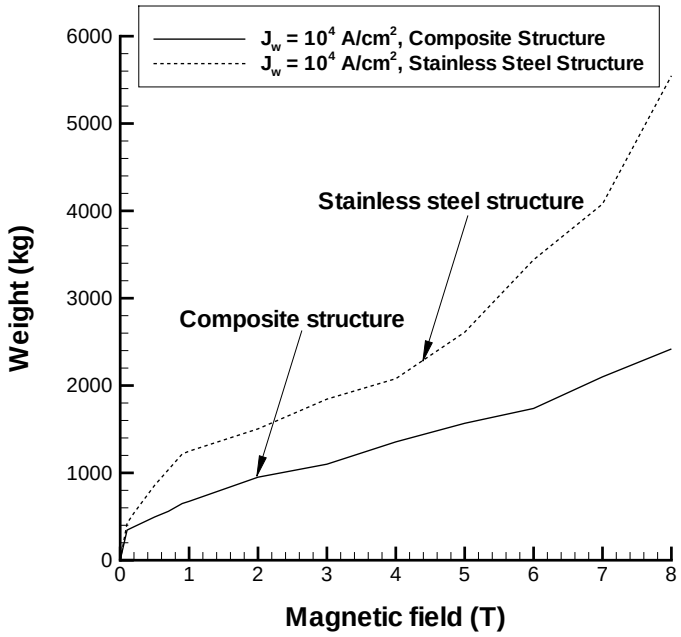

Figure 3.1: Approximate magnet weight to create a required magnetic strength [6, 54]. The magnet weight includes weights of coil, cooling system, and power supply system.

vehicle, another mitigation scheme is necessary to communicate through a plasma layer in a reliable and acceptable manner. One such scheme involves the addition of an electric field.

The magnetic window method uses only a magnetic field to reduce the plasma density, thus it requires a strong magnetic field. This method can be expanded via the addition of electric fields that increase the potential density reduction for a given magnetic field strength. An electric field can more efficiently reduce a plasma density than a magnetic field because of the possibility of a strong electric field. Since an electric field is generated without an electromagnet coil, which is the heaviest part in the magnetic window method, the electric field approach may alleviate the most serious limitation of the magnetic window method. An added benefit is that the application of crossed electric and magnetic fields (ExB) leads to some interesting

phenomena such as electron drift and the possibility of maintaining a strong electric field in a quasi-neutral plasma. Therefore, applying an ExB layer can be a mitigation scheme for communication during radio blackout.

The applied configuration of an ExB layer is shown schematically in Figure 3.2. As can be seen, the ExB layer manipulation system mainly consists of a magnet and electrodes. An embedded magnet integrated beneath the antenna along with electrodes on each side of the antenna will create the electric and magnetic fields. The applied electric field accelerates the plasma temporarily over the antenna. The ion acceleration in this electric field may lead to significant reduction of the plasma density. When the plasma density is lowered below the critical density, the plasma frequency becomes lower than the radio wave frequency. The low plasma frequency prevents infinite attenuation of the radio wave or reflection [5]. Therefore, the reduced plasma density can create a "window" in the re-entry plasma layer through which radio waves can be transmitted.

This mitigation scheme requires that a strong electric field is maintained to accelerate ions. To achieve this, the use of an electric field alone is impractical due to the shielding of the electrodes caused by sheath effects [56], in which a sheath that forms around the electrodes can have a thickness of millimeters or less at high densities. The shielding problem can be improved by applying a magnetic field. The presence of a magnetic field can trap the electrons, allowing the existence of a strong electric field. This allows ion acceleration through regions of a plasma layer, and create a corresponding plasma density decrease.

The plasma density distribution will be affected by the magnitudes and profiles of the magnetic and electric fields. There are still limits on the density of plasma which can be affected, caused by practical limitations on the magnetic and electric

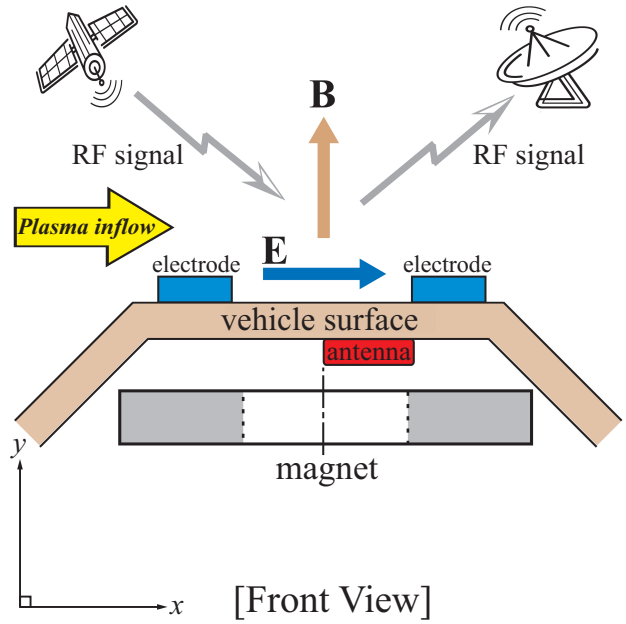

(a)

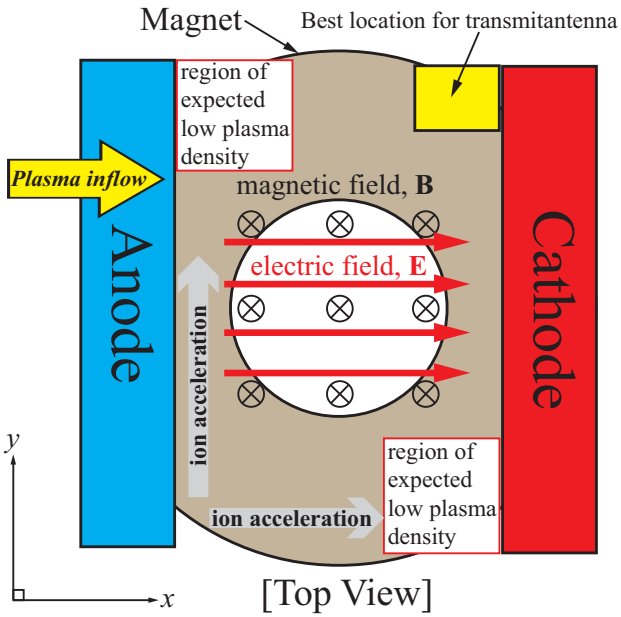

(b)

Figure 3.2: Schematic of an applied electromagnetic, ExB layer for telemetry through a hypersonic plasma layer with two different view, (a)front view (b)top view. In the flight system the magnet would be replaced by permanent magnet requiring no power. The magnetic field traps the electrons preventing them from shielding the ions from the applied electric field. The electric field accelerates the ions past the antenna, reducing the plasma density over the antenna. [6, 55]

fields that can be applied (due to magnet weight and electrode arcing). However, a significant range of densities can be manipulated, corresponding to an increased altitude range of communications or decreased periods of radio blackout.

Since the applied ExB layer can locally affect the plasma flow of the hypersonic boundary layer, the bulk of the hypersonic flow will be undisturbed by the applied ExB layer. This means that the applied ExB layer will have a minimal impact on the aerodynamic characteristics of the vehicle including drag and lift. Minimizing the impact on the vehicle's aerodynamic performance is a key advantage of this mitigation scheme over some other proposed methods.

3.2 Hypersonic Flow Field Analysis

In this section, a typical hypersonic flow is analyzed to understand the creation of the plasma layer and its properties. In the hypersonic flow analysis, the OREX re-entry vehicle is studied, which was launched and inserted into orbit via an H-II rocket in February 1994. OREX is a typical blunt body re-entry vehicle that has a nearly zero angle of attack in the re-entry experiment [4]. The geometry of OREX is presented in Figure 3.3. The nose radius, R_n, is 1.35 m, the base radius, R_b, is 1.7 m, the first cap radius, R_1, is 0.3255 m, the second cap radius, R_2, is 0.479 m, the shoulder radius, R_c, is 0.1 m, and the length of the vehicle, L, is 1.508 m. The hypersonic flow around the OREX vehicle is simulated by LeMANS which is a CFD code for hypersonic flow developed at the University of Michigan [15]. LeMANS solves the Navier-Stokes equations using a point implicit method on general unstructured meshes.

The freestream conditions for the numerical simulations are presented in Table 3.1. These values are chosen to match the conditions of the OREX re-entry experi-

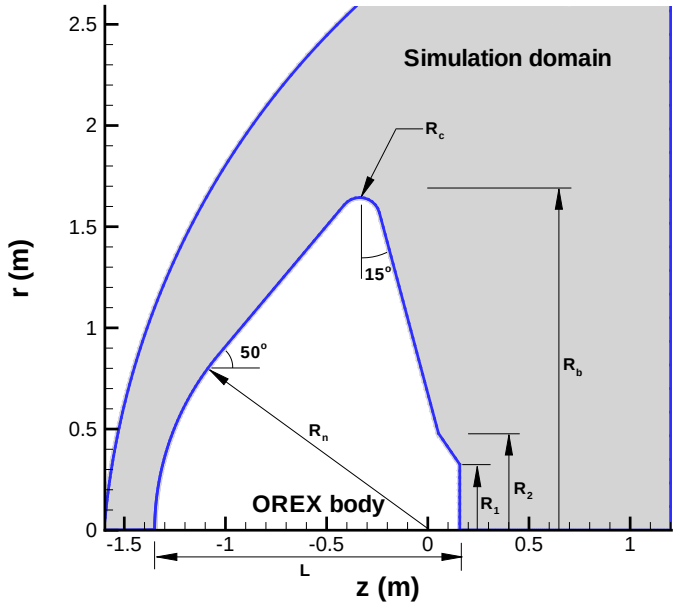

Figure 3.3: The geometry for the OREX re-entry vehicle.

ment [4]. For the hypersonic flow simulation, an eleven-species (N, O, N_2, O_2, NO, N^+, O^+, N_2^+, O_2^+, NO^+, and electron) reacting air chemistry model is employed. In this simulation, thermochemical nonequlibrium effects are included by solving a separate vibrational energy equation, as well as individual species conservation equations. The mesh employed for the computation is shown in Figure 3.4.

Contours of translational temperature at 92.82 km altitude are presented in Fig-

Table 3.1: Inflow conditions for OREX at several altitudes

Altitude (km)	Velocity V_∞ (m/sec)	Temperature T_∞ (K)	Pressure P_∞ (Pa)
92.82	7454.1	188.7	0.163
79.90	7360.2	198.64	1.0524
59.60	5561.6	248.12	23.60
48.40	3000.0	270.65	98.5

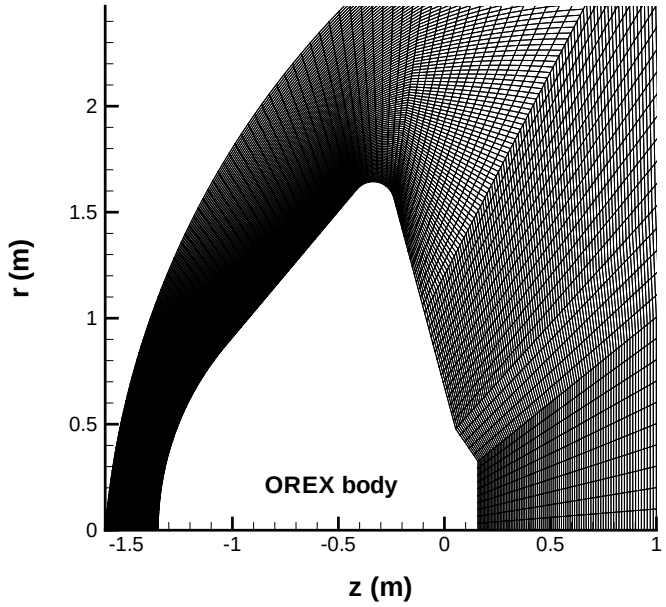

Figure 3.4: Computational mesh for the hypersonic flow simulation of OREX.

ure 3.5. As can be seen, the maximum temperature is about 20,000 K, which allows the creation of the plasma layer around the vehicle. In order to compare the electron number densities in the plasma layer, several locations along the vehicle surface are chosen as indicated in Figure 3.5. Knowledge of the electron densities can help to determine the location of the ExB layer on the vehicle for the re-entry telemetry.

The creation of the plasma layer that prevents communication is an effect of the ionization of air. The ionization of air near a hypersonic vehicle flying in the atmosphere at a velocity of $4 \sim 8$ km/s is a complicated process that requires the consideration of various factors. For the case of air, the main ionization mechanism is associative-ionization for a speed below 9 km/s. When the velocity is higher, electron-impact ionization will dominate [14]. The freestream velocity of OREX is about $3 \sim 8$ km/s through the entire trajectory as presented in Table 3.1. Thus, under the OREX re-entry condition, the main ionization mechanism is the following

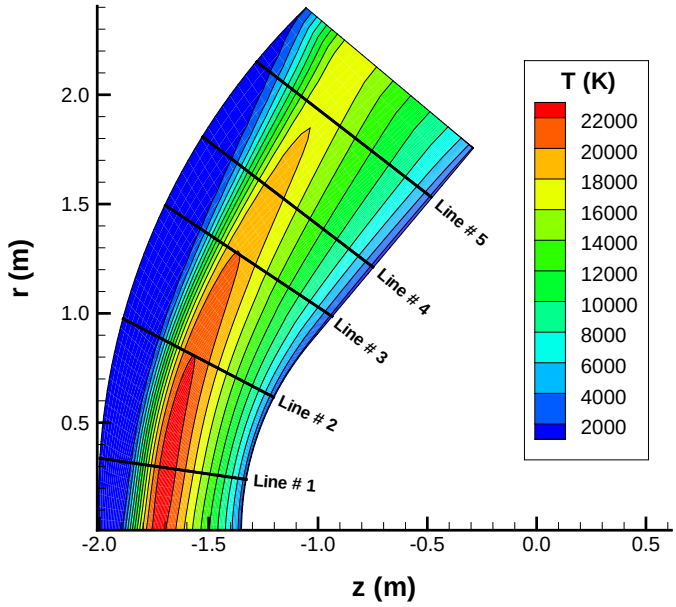

Figure 3.5: Contours of translational temperature (K) predicted by the CFD code at 92.82 km

chemical reaction:

$$N + O \leftrightharpoons NO^+ + e^- \tag{3.1}$$

$$N + N \leftrightharpoons N_2^+ + e^- \tag{3.2}$$

$$O + O \leftrightharpoons O_2^+ + e^- \tag{3.3}$$

Since electrons primarily interact with radio waves, the electron number density is the most important parameter for re-entry blackout. The calculated density distribution for electrons is presented in Figure 3.6. Profiles of electron number density at several locations of OREX are presented in Figure 3.7. The predicted electron number density is in the range of $10^{16} \sim 10^{18}$ m^{-3} depending on the location along the vehicle. Since quasi-neutral plasma is assumed, the electron number density is the same as the plasma density. According to the OREX simulation, the location

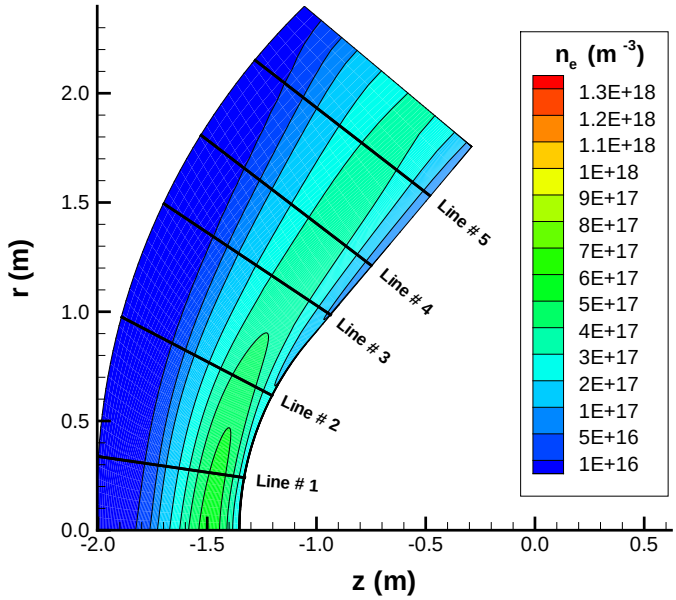

Figure 3.6: Electron number density of OREX at 92.82 km

of the plasma density peak is located close to the wall in the case of 92.82 km, as demonstrated in Figure 3.6.

Figure 3.8 presents the calculated maximum electron number densities for several altitude conditions. The figure shows that the electron number density also depends on the altitude of the vehicle because the freestream conditions are different. As can be seen, the peak electron number density increases at low altitude, exactly matching the sequence of the radio blackout. During re-entry, the vehicle first loses low-frequency radio band communication, such as VHF and UHF. The vehicle then progressively loses higher frequency radio band communication because the electron number density increases as the re-entry vehicle travels through the atmosphere. This indicates that the configuration of the ExB layer should be determined in terms of used radio wave band and altitude.

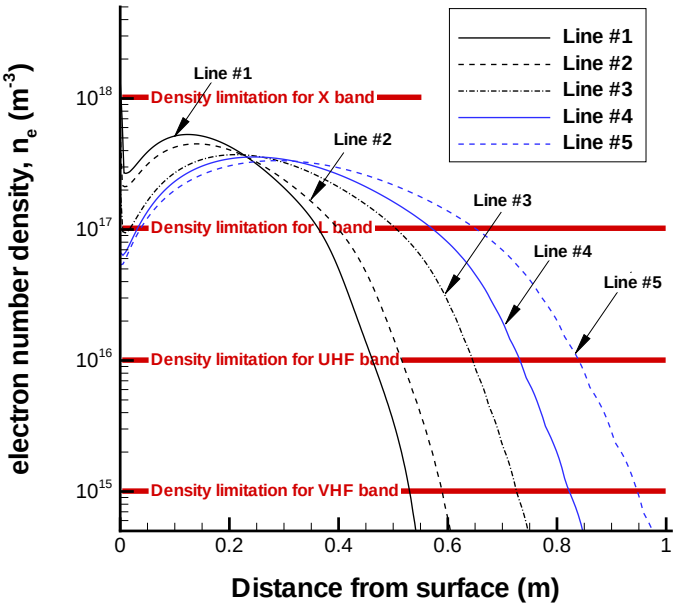

Figure 3.7: Electron number density at several locations of the OREX at 92.82 km

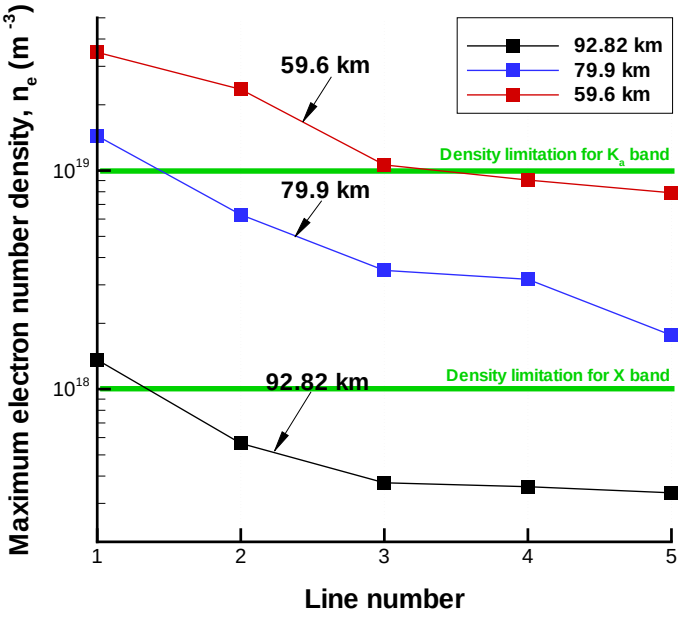

Figure 3.8: Maximum electron number density of OREX at several altitudes

3.3 One-dimensional Model of an ExB Layer

This section presents the mathematical model of an ExB layer that can be used to demonstrate its effectiveness as a mitigation scheme and primarily focuses on a one-dimensional case. The suggested ExB layer configuration is schematically shown in Figure 3.2. Although the configuration is slightly different, plasma acceleration across the ExB layer is similar to that in a Hall-effect thruster, in which a large electric field can be maintained in the quasi-neutral plasma across the magnetic field [12]. Therefore, a Hall-effect thruster model can be employed to describe the ExB layer.

A hydrodynamic model is used to describe the ExB layer with the following general assumptions:

1. **The plasma is quasi-neutral.**

   This assumption is physically reasonable because the physical size of the plasma, which is the inter-electrode length of the ExB layer, is large compared to the Debye screening length, which is related to the electron number density as shown in Eq. 3.4. As demonstrated in Section 3.2, the electron number density of the flow field is about $10^{17} \sim 10^{20}$ m^{-3}. Thus, the Debye length of a typical hypersonic plasma layer region is on the order of 10^{-4} m, which is much smaller than the characteristic length of the flow as shown in Figure 3.9. When the Debye length is much smaller than the characteristic length of the plasma, the plasma can be considered as quasi-neutral because interactions in the bulk of the plasma are more important than those at its edges, where boundary effects may take place [46, 43]. Therefore, the hypersonic flow regime satisfies the criterion for a quasi-neutral plasma.

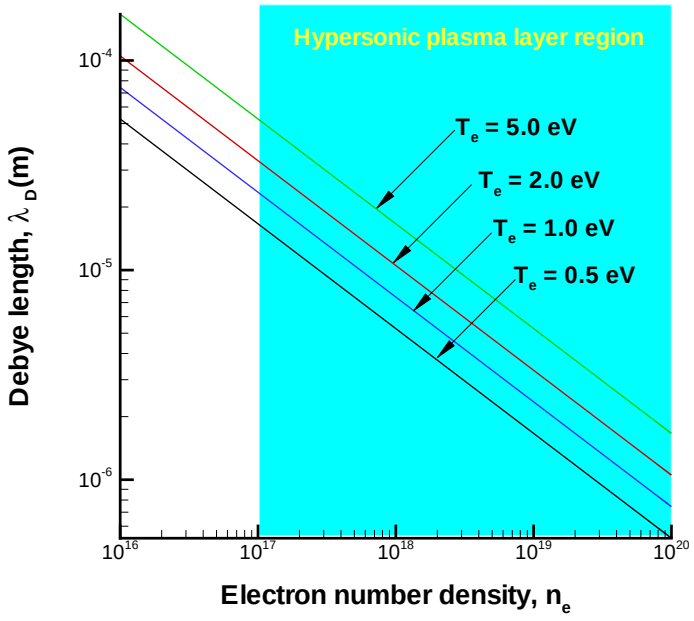

Figure 3.9: Debye length as a function of electron number density and electron temperature.

$$\lambda_D = \sqrt{\frac{\epsilon_0 k T_e}{n_e q^2}} \tag{3.4}$$

2. **The neutrals are at rest.**

   Although strictly speaking the neutrals are not at rest with the presence of the incoming hypersonic flow condition, this assumption gives the maximized collision drag term in the model. This provides the maximum estimate for the ion drag force, thus allowing the worst case to accelerate the plasma. Furthermore, the boundary layer around the vehicle results in relatively slow neutral velocity compared to the vehicle velocity [57], and it is in this stagnation layer that the plasma density that is to be manipulated is the highest.

3. **The magnetic field is one-dimensional and has a low magnetic Reynolds**

number.

The magnetic Reynolds number, a dimensionless parameter that occurs in magnetohydrodynamics, gives an estimate of the effects of magnetic advection compared to magnetic diffusion, and is typically defined by [58]:

$$R_m = \frac{magnetic\ advection}{magnetic\ diffusion} = \frac{VL}{\eta} \tag{3.5}$$

where V is the typical velocity scale of the flow, L is the typical length scale of the flow, and η is the magnetic diffusivity. Under the low magnetic Reynolds number assumption, magnetic advection is relatively unimportant compared to magnetic diffusion. Thus, the magnetic field will tend to relax towards a purely diffusive state, which is determined by the boundary conditions rather than the flow. This means that the magnetic field is only determined by the applied electromagnet or permanent magnet and is not changed by the flow field. In hypersonic flow, the magnetic Reynolds number is smaller than 10^{-3} when the ionization rate is less than 1 % [59]. In the OREX case at 59.6 km altitude condition, the maximum ionization rate is 0.3 %.

4. **Ionization is not considered.**

As presented in Section 3.2, the dominant mechanism of ionization in the reentry flow field is associative ionization, which is a gas phase reaction in which two atoms interact to form a single product ion [60], when the velocity is approximately $4 \sim 8$ km/s. Figure 3.10 compares reaction rates of associative ionization and electron impact ionization in terms of collision energy. Since the plasma is accelerated in the ExB layer, electron impact ionization will be the dominant ionization mechanism in the ExB layer region. In this case, the maximum ionization rate corresponds to unperturbed conditions because the

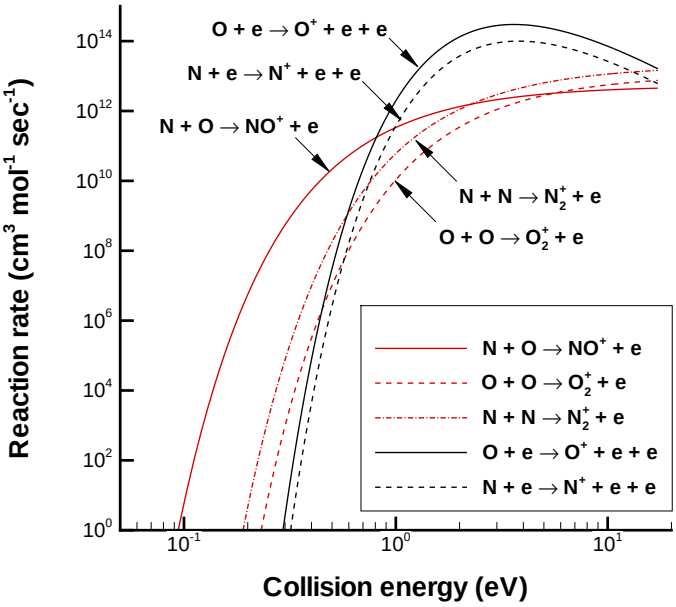

Figure 3.10: Reaction rates for ionization

electron impact ionization rate is proportional to the electron number density. The electron-impact ionization rate of the undisturbed condition can be calculated from Gryzinski's model [61].

$$\sigma_{ionization}\left(\varepsilon\right) = 4\pi a_0 \left(\frac{E_H}{E_I}\right)^2 \cdot g\left(\chi\right) \tag{3.6}$$

where $\sigma_{ionization}$ is the ionization cross section, a_0 is the Bohr radius, 0.529×10^{-10} m, E_H is the Rydberg energy, 13.6 eV, E_I is the ionization energy, and χ is defined as $\chi = \frac{\varepsilon}{E_I}$. The electron-impact ionization rate, $k_{ion}\left(T_e\right)$, is obtained from

$$k_{ion}\left(T_e\right) = \int_0^\infty f\left(\varepsilon\right)\left(\frac{2\varepsilon}{m_e}\right)^{1/2} \sigma_{ionization}\left(\varepsilon\right) d\varepsilon \tag{3.7}$$

where $f\left(\varepsilon\right)$ is a Maxwell-Boltzmann distribution function. The collision cross

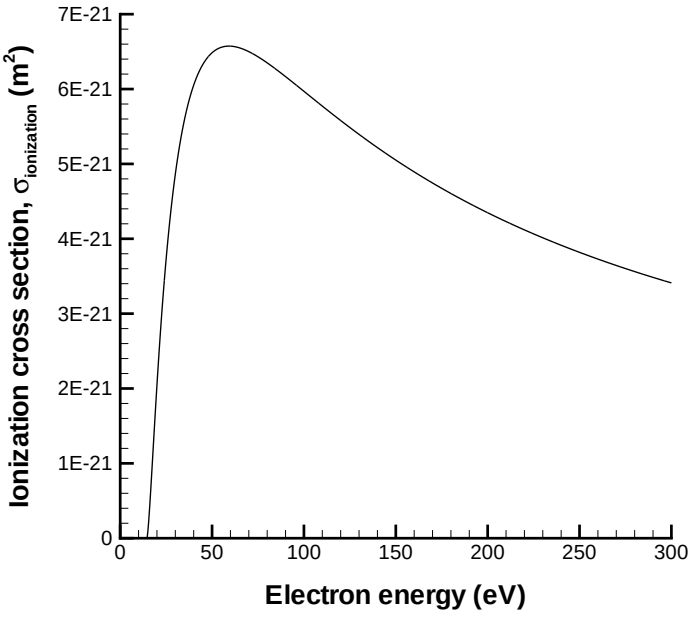

Figure 3.11: Collision cross section for ionization of nitrogen, N.

sections of the electron impact ionization for nitrogen and oxygen are presented in Figures 3.11 and 3.12, respectively and the corresponding electron impact ionization rates are shown in Figures 3.13 and 3.14, respectively. As can be seen, the electron impact ionization rate of nitrogen and oxygen is small under the low electron temperature. Therefore, the electron creation by electron impact ionization of air is relatively small compared to the electron number density of the ExB layer regime because of the cold plasma condition [62]. For argon which is used for the experiment of the ExB layer mitigation scheme, the collision cross section of the electron impact ionization is presented in Figure 3.15 and the electron impact ionization rate of argon is shown in Figure 3.16. As can be seen, the ionization rate of argon is relatively small for a cold plasma condition.

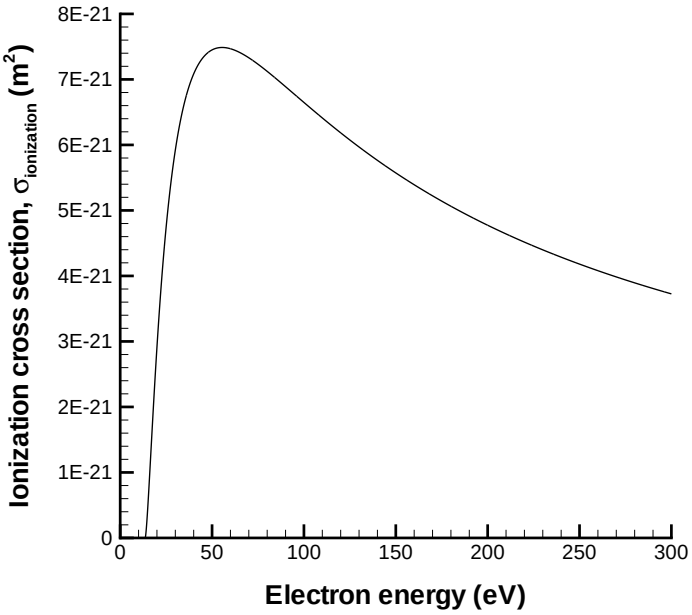

Figure 3.12: Collision cross section for ionization of oxygen, O.

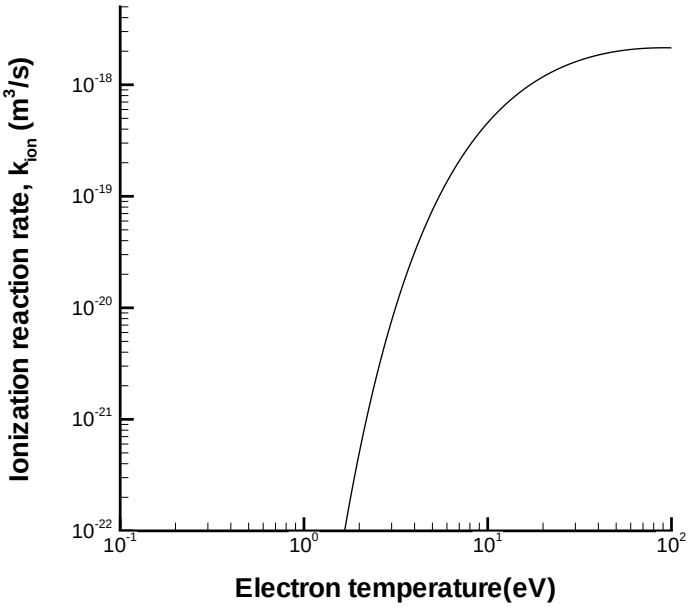

Figure 3.13: Ionization rate of nitrogen, N.

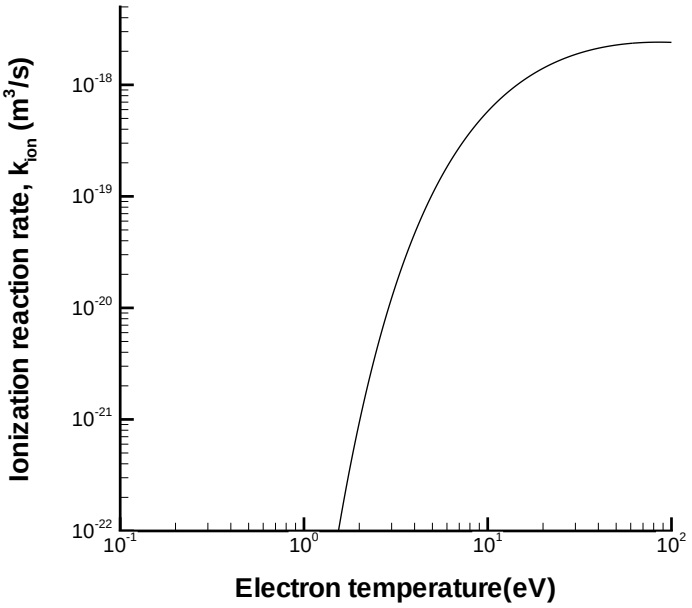

Figure 3.14: Ionization rate of oxygen, O.

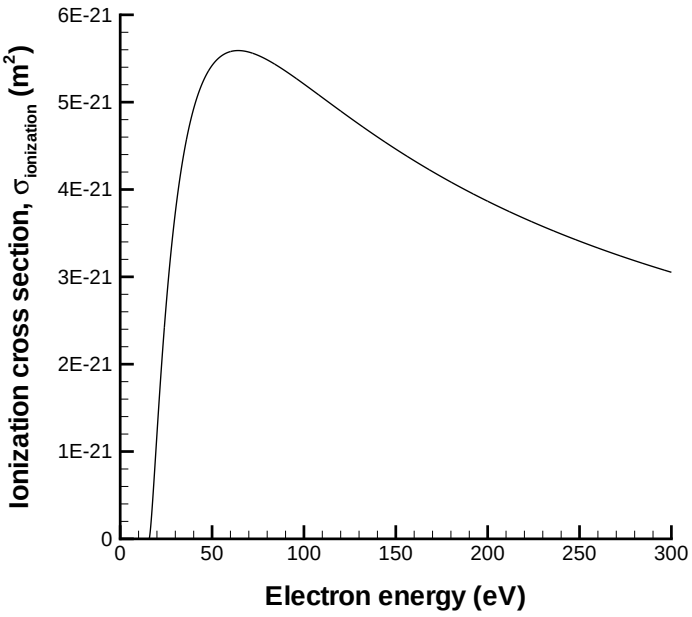

Figure 3.15: Collision cross section for ionization of argon, Ar.

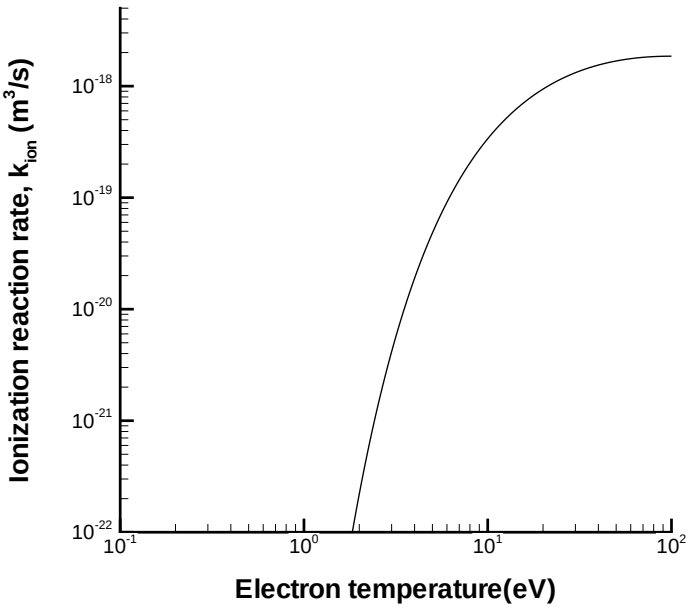

Figure 3.16: Ionization rate of argon, Ar.

5. **The electron temperature, T_e is constant.**

   The simulation and experimental data of the RAM-C test vehicle show the electron temperature in the plasma layer is almost constant [48, 49, 63, 64, 65]. An experimental study also shows a constant electron temperature for the argon plasma which was used to simulate hypersonic plasma layer [66].

In this chapter, the ExB layer model employs two different limitations: the plasma-optic regime and the magneto-hydro-dynamic (MHD) regime, each of which has a different electron drift mechanisms. The plasma-optic regime has an ExB drift to achieve plasma acceleration and the MHD regime has a JxB drift. A Comparison of these two regimes can reveal which is more reasonable under the given initial flow conditions.

3.3.1 Plasma-Optic Regime

As a first approach of the ExB layer model, the plasma-optic regime is considered. This regime involves a partially magnetized plasma, which means the electrons are magnetized and the ions are unmagnetized. For this case, the magnetization of the species is determined from the Larmor radius, Eq. 3.8.

$$r_{Larmor} = \frac{mv}{|q|\,B} \tag{3.8}$$

When the Larmor radius is smaller than a characteristic length, which is the inter-electrode length for our case, the species is considered magnetized. As can be seen in Eq. 3.8, the Larmor radius depends on the magnetic field and the mass of the species. Since ions are much heavier than electrons, the electrons are more easily magnetized. In the plasma-optic regime, the electrons are considered as the only magnetized species. This indicates that $r_e \ll L \ll r_i$, where r_e and r_i are the Larmor radii for the electrons and ions, respectively, and L is the distance between the electrodes. As shown in Figure 3.17, the plasma-optic regime is physically valid when the magnetic field is lower than 0.08 T for 10 cm inter-electrode length. Since the ions are not magnetized in this regime, they are accelerated only by the applied electric field. Therefore, the main acceleration mechanism of the plasma-optic regime is an ExB drift.

For the plasma-optic regime, a simplified one-dimensional model of the magnetized layer is developed based on a hydrodynamic model for the Hall-effect thruster [47]. The main issue to be addressed in this regime is maintaining a strong electric field. The strong electric field can be maintained across the magnetic field because the considered ExB layer configuration leads to an electron drift in the ExB direction

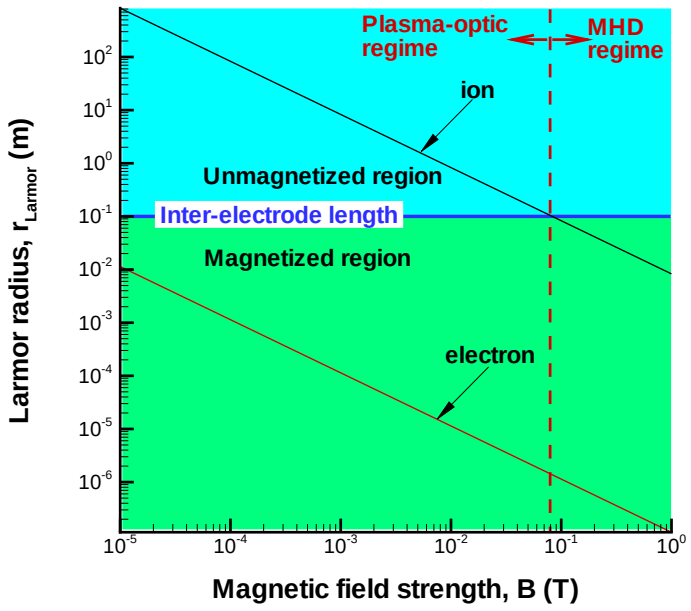

Figure 3.17: Larmor radius of electrons and argon ions.

and provides plasma quasi-neutrality across the layer. Maintaining a strong electric field causes ion acceleration leading to plasma density decrease. Assuming a steady state, the following system of equations can be used to describe the ExB layer in the plasma-optic regime:

$$\nabla \cdot (nV_i) = 0 \tag{3.9}$$

$$m_i n \left(V_i \cdot \nabla V_i\right) = enE - nm_i \nu_c V_i \tag{3.10}$$

$$m_e n \left(V_e \cdot \nabla V_e\right) = -en \left(E + V_e \times B\right) - kT_e \nabla n - nm_e \nu_e \left(V_e - V_i\right) \tag{3.11}$$

where m_i is the mass of the charged particle, ν_c is the ion collision frequency, ν_e is the electron collision frequency, e is the charge of the particle, E is the electric field,

and B is the constant magnetic field. Equation 3.9 presents ion mass conservation and Eqs. 3.10 and 3.11 are the momentum conservation equations of ions and electrons, respectively. Since the inertia term of the electron is not important, it can be neglected [67, 68]. Therefore, Eq. 3.11 can be simplified as:

$$0 = -en\left(E + V_e \times B\right) - kT_e \nabla n - nm_e \nu_e \left(V_e - V_i\right) \tag{3.12}$$

In this case, the charge exchange collisional cross section is used to obtain the collision rate of the ions because it is larger than the ion-neutral collsional cross section. The larger collisional cross section provides stronger collision drag term thus allowing a worst case for mitigation. The charge exchange collisional cross section can be approximately represented by an expression of the form [69]:

$$\sigma_{CEX}^{1/2} = a - b \ln \varepsilon \tag{3.13}$$

where a is 7.49×10^{-8} cm and b is 0.73×10^{-8} cm for argon. The charge exchange collision frequencies can be calculated from

$$\nu_{CEX} = n_n \int_0^\infty f\left(\varepsilon\right) \left(\frac{2\varepsilon}{m_e}\right)^{1/2} \sigma_{CEX}\left(\varepsilon\right) d\varepsilon \tag{3.14}$$

where n_n is the neutral number density and $f\left(\varepsilon\right)$ is the Maxwell-Boltzmann distribution function.

For the one-dimensional case, Eqs. 3.9, 3.10, and 3.12 can be expressed in component form:

$$\frac{d}{dx} nmV_{ix} = 0 \tag{3.15}$$

$$nmV_{ix}\frac{V_{ix}}{dx} = enE_x - nm_i\nu_c V_i \tag{3.16}$$

$$0 = -enE_x + enV_{ey}B_z - kT_e\frac{dn}{dx} - nm_e\nu_e\left(V_{ex} - V_{iz}\right) \tag{3.17}$$

Equation 3.17 can be expressed as a generalized Ohm's law by using the definition of current density, $j = en\left(V_{ix} - V_{ex}\right)$ and electrical conductivity, $\sigma = \frac{e^2 n}{\nu_e m_e}$. Therefore, the following expression for Ohm's law can be derived in this particular case.

$$E_x = -kT_e\frac{dn}{dx} + V_{ey}B_z + \frac{j}{\sigma} \tag{3.18}$$

The electron drift velocity,V_{ey}, in the ExB direction can be obtained from [12, 67]

$$V_{ey} = -V_{ex}\frac{\omega_e}{\nu_e} = -V_{ex}\beta \tag{3.19}$$

where ω_e is the electron cyclotron frequency and β is the Hall parameter. Thus, the electric field across the ExB layer can be calculated as:

$$E_x = -kT_e\frac{dn}{dx} - V_{ex}\beta B_z + \frac{j}{\sigma} \tag{3.20}$$

The system of Eqs. 3.15, 3.16, and 3.20 are used to describe the plasma flow across the magnetized region for the one-dimensional case with the plasma-optic approximation. For this particular one-dimensional case, the analytical solution of the plasma density reduction can be found as

$$N = \frac{n_0 V_{i,0}}{V_{i,0} + \left(\frac{m_e}{m_i}\cdot\frac{\nu_e}{e}\cdot\frac{j}{n_0 V_{i,0}} + \omega_i\beta\left(1 - \frac{j}{e}\cdot\frac{1}{n_0 V_{i,0}}\right)\right)\cdot L} \tag{3.21}$$

where N is the plasma density reduction, n/n_0, and L is the inter-electrode length. The detailed derivation of the analytical solution is presented in Appendix A.

3.3.2 MHD Regime

In a dense plasma condition, plasma density reduction is still possible, but a higher magnetic field is required [12]. As shown in Figure 3.17, a higher magnetic field results in a smaller Larmor radius of the ion. When the Larmor radius of the ion becomes smaller then the characteristic length of the ExB layer, $r_e \ll r_i \ll L$, the ion is also magnetized. This is called the MHD (magneto-hydrodynamics) regime. As shown in Figure 3.17, this regime is physically valid when the magnetic field is higher than 0.8 T for 10 cm inter-electrode length.

In the MHD regime, a hydrodynamic model with magnetized ions applies. For this case, the ions and electrons can be described as follows:

$$\nabla \cdot (nV_i) = 0 \tag{3.22}$$

$$m_i n \left(V_i \cdot \nabla V_i\right) + kT_i \nabla n = en \left(E + V_i \times B\right) - nm_i \nu_c V_i \tag{3.23}$$

$$\nabla \cdot (nV_e) = 0 \tag{3.24}$$

$$m_e n \left(V_e \cdot \nabla V_e\right) + kT_e \nabla n = -en \left(E + V_e \times B\right) - nm_e \nu_e \left(V_e - V_i\right) \tag{3.25}$$

Equations 3.22 and 3.23 are the ion conservation equations of mass and momentum, respectively. Equations 3.24 and 3.25 are the electron conservation equations of mass and momentum, respectively. To simplify the system of equations, the plasma velocity is defined as

$$V = \frac{m_i V_i + m_e V_e}{m_i + m_e} \tag{3.26}$$

Since the ion mass is much heavier than the electron mass, the plasma velocity is approximately the same as the velocity of the ions, $V \approx V_i$. Thus, Eq. 3.22 gives the equation of the mass conservation for the MHD regime.

$$\nabla \cdot (nV) = 0 \tag{3.27}$$

In the MHD regime, the current density in the ExB drift direction is small enough to be negligible in comparison with the current density in the x-direction [47]. Therefore, the current generation due to the JxB drift can be assumed to be zero. Under this assumption, the electron collision term can be neglected. Thus, the sum of Eqs. 3.23 and 3.24 provides the following momentum equation for the MHD regime as

$$m_i n \left(V \cdot \nabla V\right) + k \left(T_e + T_i\right) \nabla n = J \times B - n m_i \nu_c V_i \tag{3.28}$$

where the definition of the current density, $J = en \left(V_i - V_e\right)$ is used to simplify the equation.

Equations 3.27 and 3.28 describe plasma motion in the MHD regime. The MHD approximation allows the plasma to be treated as a single fluid that can carry an electric current. Since for a single fluid there is only one density and velocity, it is not necessary to treat the electrons and ions separately. In Eq.3.28, the Lorenz force, $J \times B$, appears as the main acceleration mechanism.

The potential distribution in the ExB layer can be calculated from current density conservation and the generalized Ohm's law, which includes the Hall effect.

$$\nabla \cdot (J) = 0 \tag{3.29}$$

$$J = \sigma \left(E + \frac{kT_e}{e} \nabla \ln n_e - \frac{J \times B}{en} + V \times B \right) \tag{3.30}$$

For the one-dimensional case, Eq. 3.29 makes it possible to use a constant current density assumption.

The system of Eqs. 3.27, 3.28, 3.29, and 3.30 are used to describe the plasma flow across the magnetized region for the one-dimensional case with the MHD approximation. For this particular one-dimensional case, the analytical solution of the plasma density reduction can be found as

$$N = \frac{2V_{i,0}}{\left(\frac{k(T_i+T_e)}{m_i V_{i,0}} - V_{i,0} + \left(\frac{jB_z}{m_i} \frac{L}{n_0 V_{i,0}} \right) \right) + \sqrt{\left(-\frac{k(T_i+T_e)}{m_i V_{i,0}} + V_{i,0} - \left(\frac{jB_z}{m_i} \frac{L}{n_0 V_{i,0}} \right) \right)^2 - 4\frac{k(T_i+T_e)}{m_i}}} \tag{3.31}$$

where N is the plasma density reduction, n/n_0, L is an inter-electrode length in m. The detailed derivation of the analytical solution is presented in Appendix A.

3.4 Simulation Result

This section presents the numerical solutions of the plasma-optic and MHD regimes. In the plasma-optic regime, the system of Equations 3.15, 3.16 and 3.20 is solved numerically using a finite volume method with the HLLC (Harten-Lax-van Leer contact wave) Riemann solver [44, 70]. The simulation uses a constant current density, because of the current density conservation, which makes it possible to calculate the electric field distribution. The MHD regime is solved with a similar numerical method as used in the plasma-optic regime.

In this section, the plasma density reduction is defined as the ratio between the local plasma density and initial plasma density in the flow field. This is a useful

variable to demonstrate the possibility of the ExB layer mitigation scheme. The required plasma density reduction to solve the radio blackout should be determined by considering the initial plasma density and the radio wave band that is used for communication.

The simulation mainly considers an experimental condition, with an initial plasma density of 4.6×10^{16} m^{-3} with 1 mTorr pressure in argon [71], in order to make comparisons with the measured data. However, several high altitude atmospheric conditions are also simulated to assess the possibility of the ExB layer mitigation scheme under re-entry conditions.

The effectiveness of the electric and magnetic fields should be investigated in order to optimize the configuration of the ExB layer. The magnetic field can be easily set to a desired value because it is an external variable with the low magnetic Reynolds number assumption. However, the potential drop, which is related to the electric field, cannot be set to a desired value because of the limitation of the one-dimensional analysis. Therefore, the simulation changes the current density instead of the potential drop.

3.4.1 Re-entry Conditions

A re-entry or hypersonic vehicle flies at several altitude conditions, each of which has different initial plasma and neutral densities. Plasma densities at several altitude conditions are listed in Table 3.2. In this section, in order to consider the general altitude conditions, 10^{18} m^{-3} initial plasma density with 10^{21} m^{-3} neutral density is used for 81 km, 10^{19} m^{-3} initial plasma density with 10^{22} m^{-3} neutral density is used for 61 km, and 10^{21} m^{-3} initial plasma density with 10^{24} m^{-3} neutral density is used for 41 km. The electrical conductivity of air is evaluated using an empirical

Table 3.2: Boundary condition for plasma density dependent on altitude

Vehicle	Altitude (km)	Initial plasma density $n_{i,0}$ (m^{-3})	Reference
RAM-C	61	10^{20}	[73]
RAM-C	71	4×10^{19}	[73]
RAM-C	81	2×10^{18}	[73]
RAM-C II	64.6	6×10^{17}	[74]
RAM-C II	61	2.5×10^{19}	[74]
SARA	61	7×10^{20}	[75]
SARA	41	8×10^{19}	[75]
RAM-C II	61	10^{20}	[76]
RAM-C II	71	2×10^{19}	[76]
RAM-C II	81	10^{18}	[76]
OREX	71	10^{19}	[4]
OREX	81	3×10^{18}	[4]
OREX	91	2×10^{17}	[4]

model, suggested by Otsu *et al* [72].

Figure 3.18 shows the plasma density reduction as a function of altitude in the plasma-optic regime. As can be seen, the applied ExB layer can significantly reduce the plasma density at 81 km, which is a relatively rarefied plasma condition. In this case, a 0.5 T magnetic field gives a density reduction of about 0.05. Even for 0.15 T, which is the maximum magnetic field technically reasonable , the density reduction is almost 0.4, which is enough to solve the X-band radio blackout. However, the density reduction becomes less strong at lower altitude. At 41 km, the density reduction is very weak even for the 0.5 T condition. This fact indicates that collisionality of

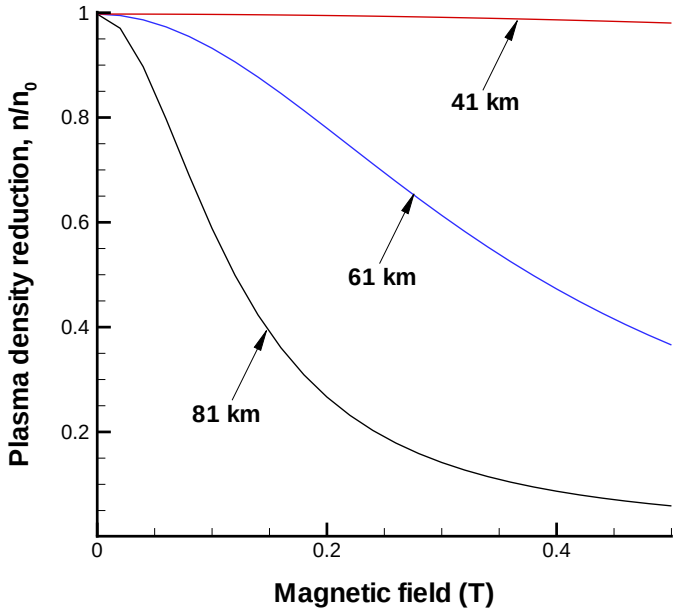

Figure 3.18: Plasma density reduction for three different altitude conditions in the plasma-optic regime. The applied current density is 100 A/m^2 and the inter-electrode length is 4 cm.

plasma and neutrals is very important and the ExB drift is negligible in the high plasma density.

As shown in Figure 3.19, the MHD regime predicts nearly the same result as the plasma optic approximation at the high altitude condition, 81 km. However, the MHD regime predicts a much stronger plasma density reduction in the low altitude case. At 41 km, the MHD regime shows the ExB layer can reduce the plasma density. This fact demonstrates that the JxB drift is an effective way to achieve plasma density reduction at low altitude conditions.

As shown in Figures 3.18 and 3.19, a strong plasma density reduction can be obtained with a low magnetic field strength at high altitude condition, 81 km. Therefore, the plasma-optic regime is physically more accurate at this altitude condition. At a low altitude condition, 41 km, a high magnetic field is required to achieve a

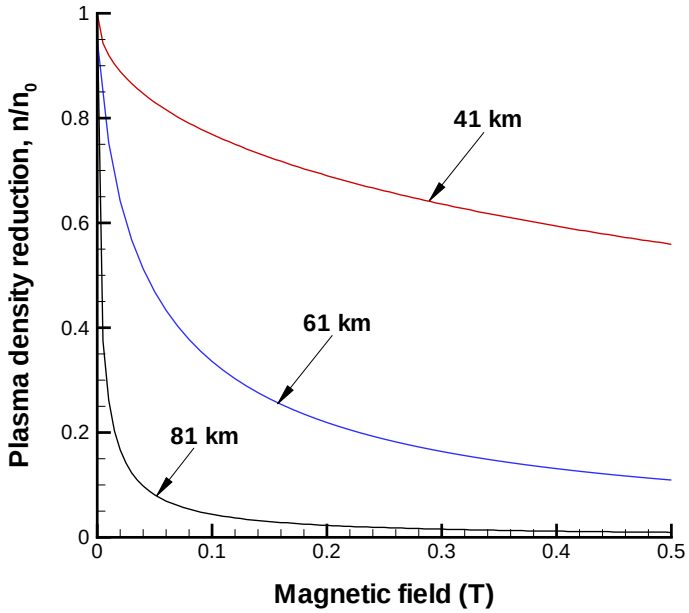

Figure 3.19: Plasma density reduction for three different altitude conditions in the MHD regime. The applied current density is 100 A/m^2 and the inter-electrode length is 4 cm.

strong plasma density reduction. Since both ions and electrons should be magnetized at a high magnetic field, which is higher than 0.08 T, the MHD regime is physically more accurate to simulate the ExB layer as a mitigation scheme. However, even for a high altitude condition, the MHD regime should be applied when a higher than 0.08 T magnetic field is imposed.

3.4.2 Effectiveness of Magnetic Field Strength

The magnetic field affects the plasma density reduction because it generates a Lorenz force in the plasma and helps to maintain a strong electric field. As expected, a high magnetic field provides a strong plasma density reduction. However, a high magnetic field is not a practical solution of blackout because extra weight is necessary to generate the high magnetic field. Therefore, the effectiveness of the magnetic field should be investigated to minimize the weight. In this section, an experimental condition is used for comparison of the model with measured data.

Figures 3.20 and 3.21 show the influence of the magnetic field on the plasma density reduction in the plasma-optic and MHD regimes. As shown, a significant plasma density reduction occurs under a high magnetic field. However, the rate of the plasma density reduction becomes lower at the strong magnetic field condition. The plasma density reduction of the MHD regime is almost maximized with 0.2 T. At a low magnetic field, the plasma-optic regime is more valid. However, the MHD regime is physically more valid for a high magnetic field condition, 0.08 T.

The potential drop between the two electrodes is also indicated in Figures 3.20 and 3.21. As can be seen, the strong magnetic field is concomitant with a high potential drop. The high potential drop is a result of the assumption of a constant current density. The potential drop should be limited because a higher than 10^4 V

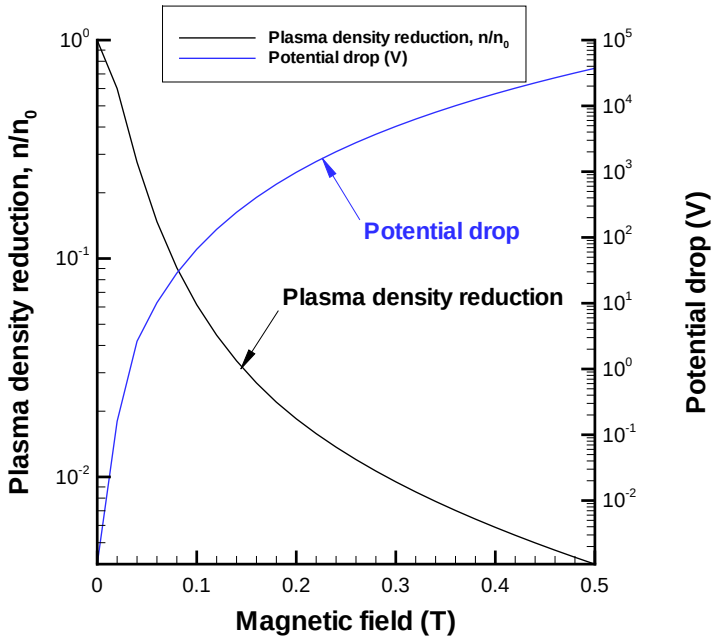

Figure 3.20: Plasma density reduction as a function of applied magnetic field in the plasma-optic regime. Applied current density is 100 A/m^2 and the experimental condition is used, which is 4.2×10^{16} m^{-3} initial plasma density with 1 mTorr pressure for argon.

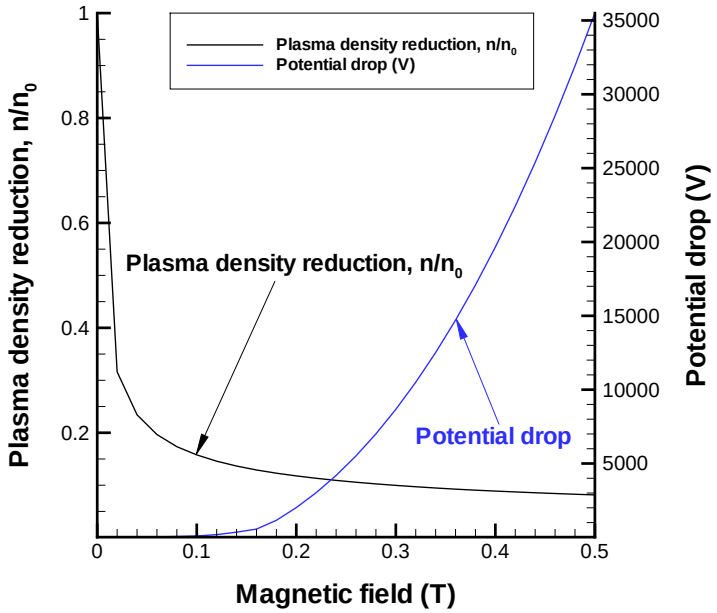

Figure 3.21: Plasma density reduction as a function of applied magnetic field in the MHD regime. Applied current density is 100 A/m^2 and the experimental condition is used, which is 4.2×10^{16} m^{-3} initial plasma density with 1 mTorr pressure for argon.

potenial is difficult to achieve in a real application.

3.4.3 Effectiveness of Current Density

The current density is another important parameter that can affect the plasma density reduction. A high current density leads to higher ExB and JxB drifts, which then cause the plasma density reduction to become strong in the ExB layer. The current density cannot be controlled in a real system. However, the current density is a useful variable to investigate the effectiveness of the electric field in the one-dimensional analysis because it is related to the potential drop across the ExB layer [53].

The effect of the current density on the plasma density reduction for the experimental chamber condition is shown for the plasma-optic regime in Figures 3.22. As can be seen, a higher current density across the ExB layer leads to stronger plasma density reduction.

The plasma density reduction for several current densities in the experimental condition is shown for the MHD regime in Figures 3.23. As can be seen, a high current density provides a strong density reduction under the same magnetic field condition.

3.4.4 Possible Solution Map

A strong plasma density reduction is required to solve radio blackout but this is only possible with a high magnetic field and potential drop. However, the possibility of achieving the appropriate magnetic field and potential drop is limited because of the weight of the magnet and the electrode arcing problem. A reasonable magnetic field is about 0.15 T with the weight limitation and the potential drop should be limited below 10 kV in order to prevent an arc between the two electrodes. These

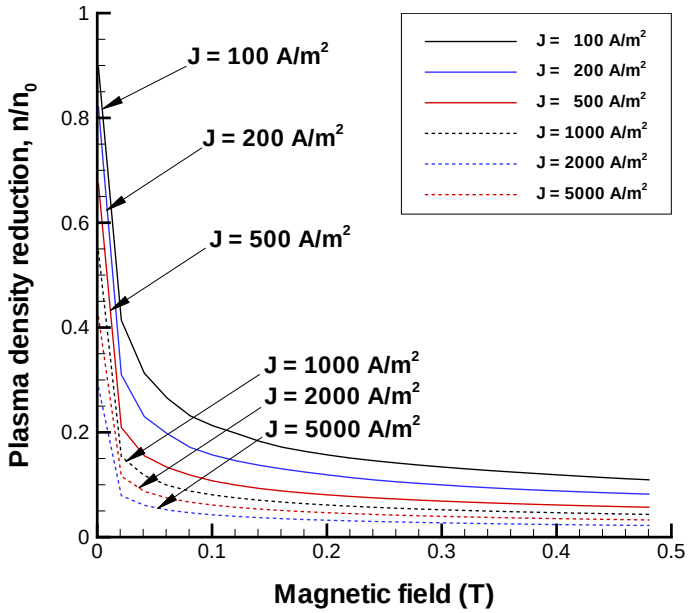

Figure 3.22: Plasma density reduction as a function of applied current density in the plasma-optic regime. In this case the experimental condition is used, which is 4.2×10^{16} m^{-3} initial plasma density with 1 mTorr pressure for argon.

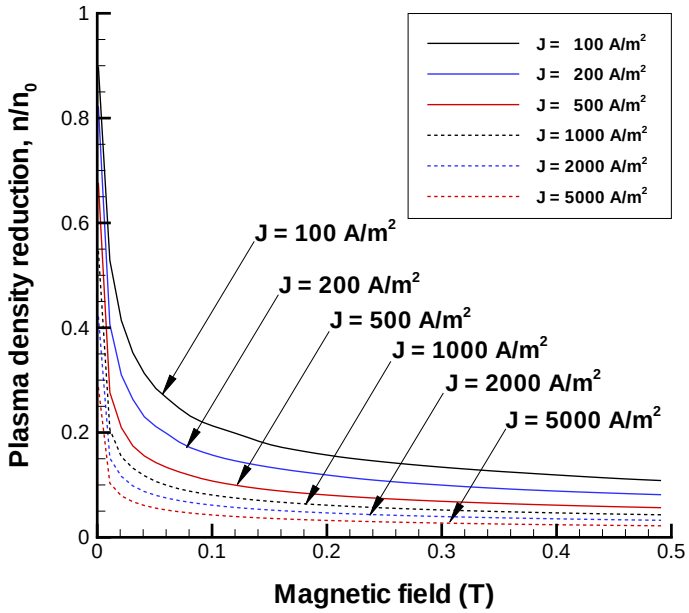

Figure 3.23: Plasma density reduction as a function of applied current density in the MHD regime. In this case the experimental condition is used, which is 4.2×10^{16} m^{-3} initial plasma density with 1 mTorr pressure for argon.

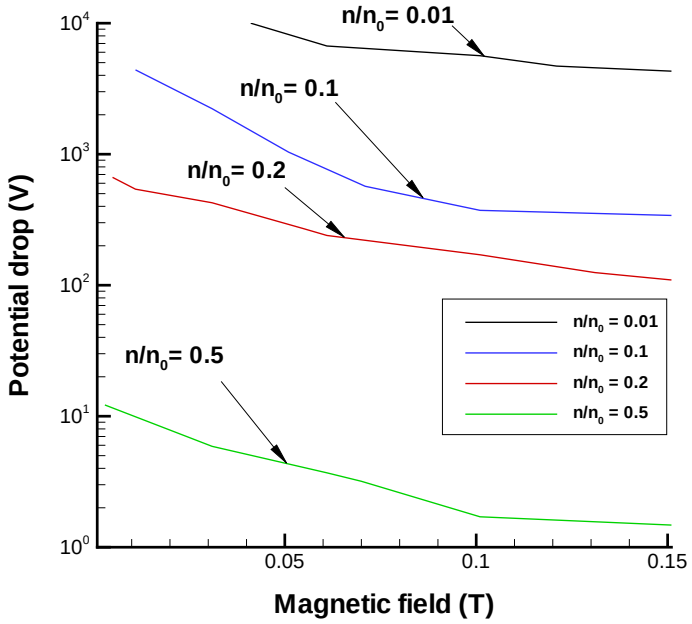

Figure 3.24: Solution map in the plasma-optic regime. The initial plasma density is 4.2×10^{16} m^{-3} with 1 mTorr pressure of argon.

ranges provide a possible configuration of the ExB layer in order to achieve a desired plasma density reduction.

Figures 3.24 and 3.25 show possible configurations of the ExB layer to achieve a desired density reduction in the the two regimes.

The desired density reduction for blackout mitigation should be based on the peak plasma density and the radio-wave frequency used for communication. As shown in Chapter 1.3, various radio-wave frequencies are used for different applications. This means that each application requires a different plasma density reduction to solve radio blackout. Figure 3.26 shows the required plasma density reduction for each radio wave frequency. As shown in the figure, when the density reduction ratio is about 0.2 with 4.2×10^{16} m^{-3} initial plasma density, the vehicle loses the VHF signal which is used for voice communication, but the vehicle can receive an L-band signal,

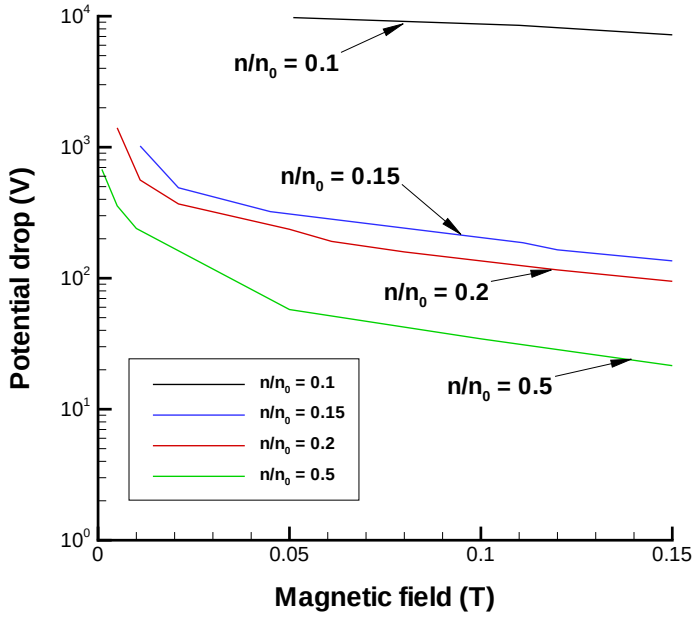

Figure 3.25: Solution map in the MHD regime. The initial plasma density is 4.2×10^{16} m^{-3} with 1 mTorr pressure of argon.

used for data telemetry.

3.5 Conclusion

In this chapter, application of electric and magnetic fields was proposed to produce a significant reduction in the plasma density allowing radio communication through a hypersonic plasma layer. The proposed ExB layer is described by a hydrodynamic plasma model with two approximations, namely the plasma-optic and MHD limits. The plasma-optic regime focuses on the ExB drift and the MHD regime concentrates on the JxB drift. Both regimes are solved numerically with a finite volume method and the results show that the plasma density can be effectively reduced by using an ExB layer.

Both the plasma-optic and MHD regimes show that the plasma density can be

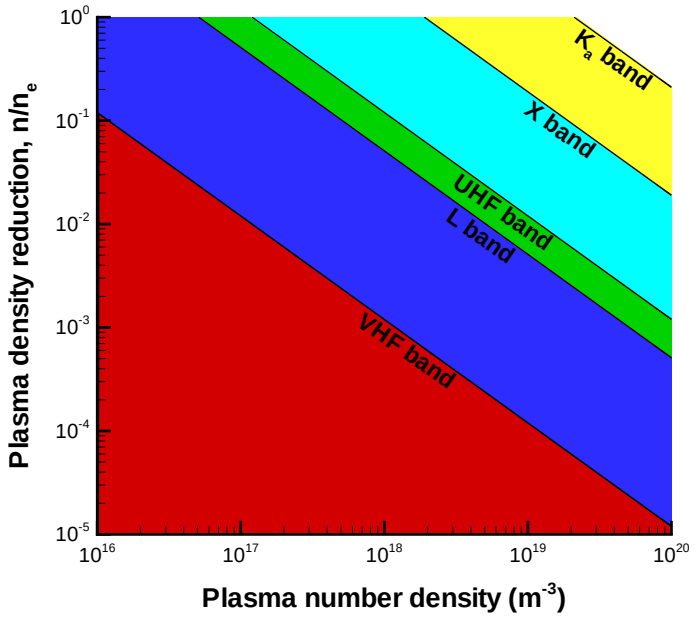

Figure 3.26: Required plasma density reduction ratio for each radio wave frequency

significantly reduced in the weak plasma generated at high altitude conditions such as 81km. In dense plasma, low altitude conditions such as 41 km, the plasma acceleration in the plasma-optic regime is negligible, but the MHD regime shows that it can effectively accelerate the plasma. This means that the JxB drift is useful for accelerating the plasma when the ion-neutral collisions become important.

The numerical results show that a strong density reduction can be obtained with high magnetic field and potential drop. However, the maximum magnetic field and potential drop are limited by technical aspects which include the weight of the magnet and the electrode arcing problem. The applicable ranges of the magnetic field and potential drop make it possible to create a solution map which provides a possible configuration of the ExB layer. The configuration of the ExB layer can be determined for the desired density reduction. The required density reduction varies with the radio wave frequency. For instance, an ExB layer with 0.1 T gives almost 0.1 density

reduction. This density reduction is still too weak to address communication blackout of the VHF or L-band but it is strong enough to solve the radio blackout of the UHF band.

CHAPTER IV

Two-dimensional Model of an Electromagnetic Layer

The one-dimensional ExB layer model using the plasma-optic and MHD regimes was presented in Chapter III. This model, however, cannot determine the size of the communications window that is created by the manipulated plasma density. Therefore, this chapter mainly focuses on a two-dimensional ExB layer model that can estimate the size of the window created for communication. The estimation of the size of the window is very important for the possibility of communication through the plasma layer, because it must be larger than the size of the communication antenna. The communications window created by the reduced plasma density also must extend far enough from the surface to affect the plasma density peak, which occurs at 1-2 cm above the vehicle surface in the RAM-C flight test [48, 49]. In order to determine the size of the communications window, a two-dimensional approach should be employed for the applied ExB layer. The main issue of the two-dimensional ExB layer model is the potential distribution, which introduces an electric field into the ExB layer. This chapter uses two different potential distribution models to calculate the potential: the thermalized potential model and a Poisson-like model.

4.1 Mathematical Modeling of an ExB Layer

This chapter uses a two-dimensional ExB layer MHD model which is schematically shown in Figure 4.1. As can be seen, the xz-plane is the main area of focus for demonstrating the region of effectiveness of the ExB layer mitigation scheme. The ExB layer approach requires a high magnetic field for a strong plasma density reduction, thus the MHD regime is more useful than the plasma-optic regime. The two-dimensional ExB layer MHD model is based on a two-dimensional steady-state fluid plasma model with the following general assumptions[77]:

1. The E x B layer is quasi-neutral.
2. The neutrals are at rest.
3. There is no ionization in the E x B layer.
4. The electron temperature Te is constant.
5. The ions are cold in hypersonic flow.
6. The magnetic Reynolds number is smaller than 1.

The assumptions used are similar to those of the one-dimensional ExB layer MHD model in Chapter III and are physically reasonable. First, quasi-neutrality is consistent with measured data from re-entry vehicles [8]. The measured data show the Debye length is typically on the order of 10^{-6} m, so the sheath region is very small compared with the plasma region. Although strictly speaking the neutrals are not at rest with an incoming hypersonic flow condition, the stationary neutral assumption will maximize the effect of the ion-neutral drag term in the model, thus rendering the calculations for a worst-case scenario. Furthermore, the boundary layer

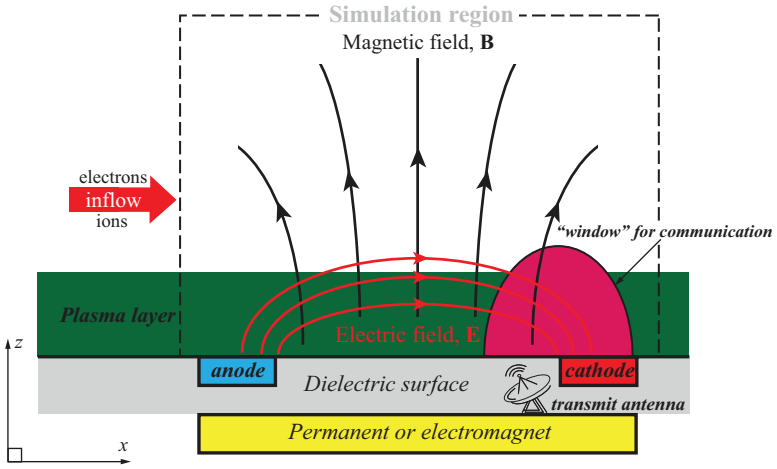

Figure 4.1: A schematic of the ExB layer for the two-dimensional approach.

around the vehicle results in a neutral velocity that is relatively slow compared to the vehicle velocity [12, 57], and it is in this stagnation layer that the plasma density to be mitigated is highest. In the ExB layer model, the plasma is already created by associative and electron-impact ionization, which are the two production mechanisms of electrons in a hypersonic flow [14, 78]. Therefore, additional plasma creation by ionization does not need to be considered. Therefore, the two-dimensional steady-state ExB layer model can be described by:

$$\nabla \cdot \left(n_i \vec{\mathbf{V}}_i \right) = 0 \tag{4.1}$$

$$m_i n_i \left(\vec{\mathbf{V}}_i \cdot \nabla \vec{\mathbf{V}}_i \right) = e n_i \left(\vec{\mathbf{E}} + \vec{\mathbf{V}}_i \times \vec{\mathbf{B}} \right) - \nabla p_i + \vec{\mathbf{R}}_i \tag{4.2}$$

$$\nabla \cdot \left(n_e \vec{\mathbf{V}}_e \right) = 0 \tag{4.3}$$

$$0 = -e n_i \left(\vec{\mathbf{E}} + \vec{\mathbf{V}}_e \times \vec{\mathbf{B}} \right) - \nabla p_e + \vec{\mathbf{R}}_e \tag{4.4}$$

where $\vec{\mathbf{R}}_i$ is the friction force for the ions and $\vec{\mathbf{R}}_e$ is the friction force for the electrons. Equations 4.1 and 4.2 are mass and momentum conservation for the ions, respectively. Equations 4.3 and 4.4 are mass and momentum conservation for the electrons, respectively.

The quasi-neutral plasma assumption with one-species ions makes it possible to write:

$$n_i = n_e = n \tag{4.5}$$

In order to simplify Eqs. 4.1 - 4.4, the plasma velocity, $\vec{\mathbf{V}}$, and the electric current density, $\vec{\mathbf{J}}$, are employed.

$$\vec{\mathbf{V}} = \frac{m_i \vec{\mathbf{V}}_i + m_e \vec{\mathbf{V}}_e}{m_i + m_e} \tag{4.6}$$

$$\vec{\mathbf{J}} = en\left(\vec{\mathbf{V}}_i - \vec{\mathbf{V}}_e\right) \tag{4.7}$$

Since ions are much heavier than electrons, the ion velocity becomes the plasma velocity.

$$\vec{\mathbf{V}}_i \approx \vec{\mathbf{V}} \tag{4.8}$$

Therefore, the ion mass conservation equation, Eq. 4.1, provides a continuity equation for the plasma flow:

$$\nabla \cdot \left(n\vec{\mathbf{V}}\right) = 0 \tag{4.9}$$

The momentum equation of the plasma flow is obtained from the summation of the momentum equations, Eqs. 4.2 and 4.4.

$$m_i n \left(\vec{\mathbf{V}} \cdot \nabla \vec{\mathbf{V}}\right) = \left(\vec{\mathbf{J}} \times \vec{\mathbf{B}}\right) - \nabla p + \vec{\mathbf{R}} \tag{4.10}$$

where p is the total plasma pressure term, $p = p_i + p_e$, and $\vec{\mathbf{R}}$ is a collision drag term of the plasma flow. Therefore, Eqs. 4.9 and 4.10 describe the plasma flow in the ExB layer. In Eq. 4.10, the $\vec{\mathbf{J}} \times \vec{\mathbf{B}}$ term is the Lorentz force accelerating the plasma.

The ExB layer model, Eqs. 4.9 and 4.10, needs a description for the current density, $\vec{\mathbf{J}}$, in order to close the system of equations. The current density is calculated from the generalized Ohm's law, which can be expressed in a matrix form as follows:

$$\vec{\mathbf{J}} = \tilde{\sigma} \left(\vec{\mathbf{E}} + \vec{\mathbf{V}} \times \vec{\mathbf{B}}\right) \tag{4.11}$$

where $\tilde{\sigma}$ is the conductivity tensor:

$$\tilde{\sigma} = \frac{\sigma}{1+\beta^2} \begin{bmatrix} 1+\beta_x^2 & \beta_x\beta_y & \beta_x\beta_z \\ \beta_y\beta_x & 1+\beta_y^2 & \beta_y\beta_z \\ \beta_z\beta_x & \beta_z\beta_y & 1+\beta_z^2 \end{bmatrix} \tag{4.12}$$

where, $\beta_x = \beta_e \frac{B_x}{B}$, $\beta_y = \beta_e \frac{B_y}{B}$, $\beta_z = \beta_e \frac{B_z}{B}$, β is the Hall parameter, and σ is the DC conductivity.

The conductivity tensor, Eq. 4.12, can be simplified for an xz plane because the applied magnetic field has no y-direction component. The conductivity tensor becomes

$$\tilde{\sigma} = \frac{\sigma}{1+\beta^2} \begin{bmatrix} 1+\beta_x^2 & 0 & \beta_x\beta_z \\ 0 & 1 & 0 \\ \beta_z\beta_x & 0 & 1+\beta_z^2 \end{bmatrix} \tag{4.13}$$

The system of equations, Eqs. 4.9, 4.10, and 4.11, describes the two-dimensional ExB layer. In this chapter, the two-dimensional ExB layer model uses two different potential distribution models, which are the thermalized potential model and the Poisson-like model.

4.1.1 Thermalized Potential Model

As a first approach, the thermalized potential model is employed. The thermalized potential concept was proposed by Morozov to describe the potential distribution of the stationary plasma thruster [79, 80]. This concept reduces the two-dimensional potential distribution problem to a quasi one-dimensional problem.

In the two-dimensional magnetic field condition, the electron mobility is not a simple scalar. The value of the electron mobility is much larger for electron transport along magnetic field lines than for transport across the magnetic field. However, the electron flux is not much larger along magnetic field lines than across the magnetic field because of the current conservation. Therefore, along each magnetic field line there is a balance between the electrostatic pressure and the electron thermal pressure, that can be calculated as

$$-\mu E_{\perp} n - \mu T_e \nabla n = 0 \tag{4.14}$$

where $E_{\perp}$ is the electric field across the magnetic field.

Equation 4.14 can reduce the two-dimensional electric field problem to a quasi one-dimensional problem. This simplifies the electrostatic field calculation, which is known as the thermalized potential or equipotential along the magnetic field line [79, 81]. The thermalized potential concept defines a constant for each individual magnetic field line, which is the thermalized potential. The thermalized potential,

ϕ^*, is defined as

$$\phi^* = \phi - T_e \ln\left(\frac{n\,(x,z)}{n_0}\right) \tag{4.15}$$

where n_0 is a reference plasma number density. The detailed derivation of Eq. 4.15 is presented in Appendix B. Along the given magnetic field line, the potential and density vary to maintain a constant thermalized potential while from a given field line to a different field line, the value of the thermalized potential may vary.

The magnetic field lines are plasma equi-potentials within an accuracy of the order of the electron temperature, T_e, that is, within an accuracy in V on the order of the electron temperature in eV. Since the electron temperature in the ExB layer is not very high, the plasma equi-potentials cannot depart significantly from the magnetic field lines.

4.1.2 Poisson-like Potential Model

When a high potential drop is applied between the two electrodes, the thermalized potential concept is not useful because the thermalized potential departs from the magnetic field lines on the order of the electron temperature. Since the electron temperature is relatively small compared to the applied voltage, the potential is almost the same as the magnetic field line. According to the thermalized potential model, the magnetic field line from the cathode, which is called the cathode line, has the highest negative potential. When there is a high voltage on the cathode, the cathode line will have a high negative thermalized potential which is much larger than the electron temperature. Since the second term on the right side of Eq. 4.15 is much smaller than the high negative thermalized potential, the potential of the ExB layer varies only slightly from the thermalized potential. For instance, even if the density reduction ratio is less than 0.001, the second term is just on the order of

10 V.

The thermalized potential concept was originally proposed for the Hall-effect thruster which has a simple magnetic field configuration [47, 81]. However, the magnetic field configuration of the ExB layer mitigation scheme is more complicated than for the Hall-effect thruster. As shown in Figure 4.2(a), the magnetic field lines of the ExB layer mitigation scheme are directed out of the inter-electrode gap but a Hall thruster has magnetic field lines parallel with an anode. For a Hall thruster case, anode and cathode lines are closed and the potential difference across the magnetic field lines is smaller than the configuration of the ExB layer mitigation scheme. In addition, the applied potentials of a Hall thruster are lower than the ExB layer approach. When a high voltage is applied at the cathode, the potential difference across the magnetic field lines becomes large compared to the electron temperature in the ExB layer configuration for the mitigation scheme. In this case, the thermalized potential model does not allow a large potential difference across the magnetic field lines.

In this case, the potential can be calculated using a Poisson-like model that is based on the current density conservation. Current density conservation indicates that no current is generated in the ExB layer.

$$\nabla \cdot \vec{\mathbf{J}} = 0 \tag{4.16}$$

The current density can be calculated from the generalized Ohm's law, Eq. 4.11 and the component forms of the current density become

$$J_x = \frac{\sigma}{1+\beta^2}\left[\left(1+\beta_x^2\right)E_x + \beta_x\beta_z E_z\right] \tag{4.17}$$

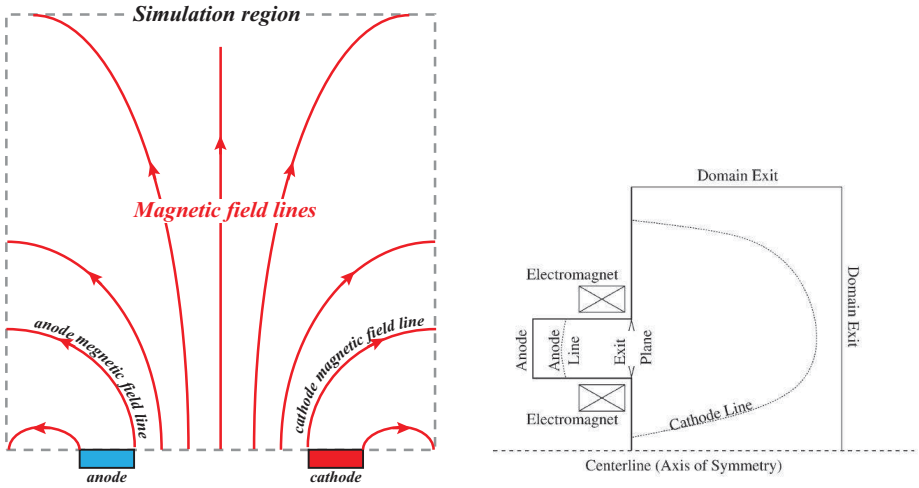

(a) (b)

Figure 4.2: (a) A schematic of the potential problem of the thermalized potential model with a high potential drop. (b) Magnetic field lines of a Hall thruster [82]

$$J_z = \frac{\sigma}{1+\beta^2}\left[\beta_z\beta_x E_x + \left(1+\beta_z^2\right)E_z\right] \tag{4.18}$$

Equations 4.17 and 4.18 give a Poisson equation for the potential distribution with the current density conservation, Eq. 4.16, and the definition of the electric field, $E = -\nabla\phi$.

$$\begin{aligned}\left(\frac{1+\beta_x^2}{1+\beta^2}\sigma\right)\frac{\partial^2\phi}{\partial x^2} &+ \left(\frac{1+\beta_z^2}{1+\beta^2}\sigma\right)\frac{\partial^2\phi}{\partial z^2} + \left(\frac{2\beta_x\beta_z}{1+\beta^2}\sigma\right)\frac{\partial^2\phi}{\partial x\partial z} \\ &+ \left(\frac{\partial}{\partial x}\left(\frac{1+\beta_x^2}{1+\beta^2}\sigma\right) + \frac{\partial}{\partial z}\left(\frac{\beta_x\beta_x}{1+\beta^2}\sigma\right)\right)\frac{\partial\phi}{\partial x} \\ &+ \left(\frac{\partial}{\partial x}\left(\frac{\beta_x\beta_z}{1+\beta^2}\sigma\right) + \frac{\partial}{\partial z}\left(\frac{1+\beta_z^2}{1+\beta^2}\sigma\right)\right)\frac{\partial\phi}{\partial z} = 0\end{aligned} \tag{4.19}$$

Generally, Eqn. 4.19 can be expressed as

$$\nabla\cdot(\tilde{\sigma}\nabla\phi) = \nabla\cdot\left(\tilde{\sigma}\left(\vec{\mathbf{V}}\times\vec{\mathbf{B}}\right)\right) \tag{4.20}$$

where $\tilde{\sigma}$ is the conductivity tensor. The conductivity tensor can include the ion-slip and the Hall effect. When these effects are not important, the conductivity tensor

becomes a simple scalar.

Equation 4.19 is a non-linear 2nd order Elliptic PDE (Partial Differential Equation). Solving Eqn. 4.19 gives the potential distribution of the ExB layer. Since the coefficient of the last two terms of Eq. 4.19, which are

$$\left(\frac{\partial}{\partial x}\left(\frac{1+\beta_x^2}{1+\beta^2}\sigma\right)+\frac{\partial}{\partial z}\left(\frac{\beta_x\beta_x}{1+\beta^2}\sigma\right)\right)\frac{\partial\phi}{\partial x}$$

$$\text{and}\quad \left(\frac{\partial}{\partial x}\left(\frac{\beta_x\beta_z}{1+\beta^2}\sigma\right)+\frac{\partial}{\partial z}\left(\frac{1+\beta_z^2}{1+\beta^2}\sigma\right)\right)\frac{\partial\phi}{\partial z}=0$$

may be much larger than the other terms, Eq. 4.19 should be carefully discretized. In this case, the upwind discretization scheme is useful.

4.2 Domain Configuration and Boundary Condition

The configuration of the ExB layer is presented in Figure 4.3. The electromagnet is located below a mica sheet, which is a dielectric material, and provides the magnetic field for the ExB layer. As can be seen, the ExB layer has two 5 mm electrodes which are separated by 4 cm that provide the electric field for the system. A negative potential is applied on the cathode and the anode is grounded at a potential of 0 V .

The ExB layer model is solved numerically with an iterative scheme. The solution begins by assuming an initial potential distribution, ϕ^0, which is obtained by solving the Laplace equation. The estimated potential distribution is differentiated to give the initial electric field. The calculated electric field is used to solve the ion transport equations, Eqs. 4.9 and 4.10. The ion transport equation is solved by using the finite volume method with the Harten-Lax-van Leer contact wave (HLLC) solver and gives the plasma number density and velocity. The obtained plasma number density and velocity distributions are used to calculate the new potential distribution. The potential distribution is obtained from the thermalized potential model or the

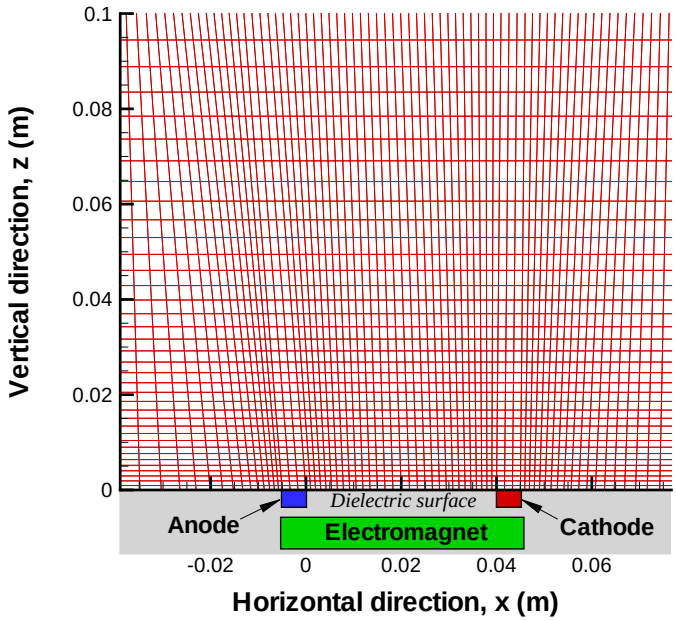

Figure 4.3: Computational mesh for the ExB layer mitigation scheme.

Poisson-like model.

Figure 4.4 shows the grid convergence behavior of the ExB layer model. In this chapter, a 50×50 structured grid is used for the ExB layer simulation.

Figure 4.5 shows the boundary conditions applied in the two-dimensional ExB layer MHD model. An inflow boundary condition is applied on the left side and uses the initial plasma number density and the constant neutral number density. In this case, the bulk plasma velocity is assumed to be 1000 m/s with only an x direction component. The right and upper side boundaries use the outflow boundary condition and a zero potential variation across the boundary is assumed. The bottom boundary uses a dielectric boundary condition in which no ions are neutralized, which means that the wall fully absorbs ions and thus acquires charge.

An applied potential boundary condition at the electrodes is shown in Figure 4.6. As can be seen, the boundary condition of the potential uses a linear distribution

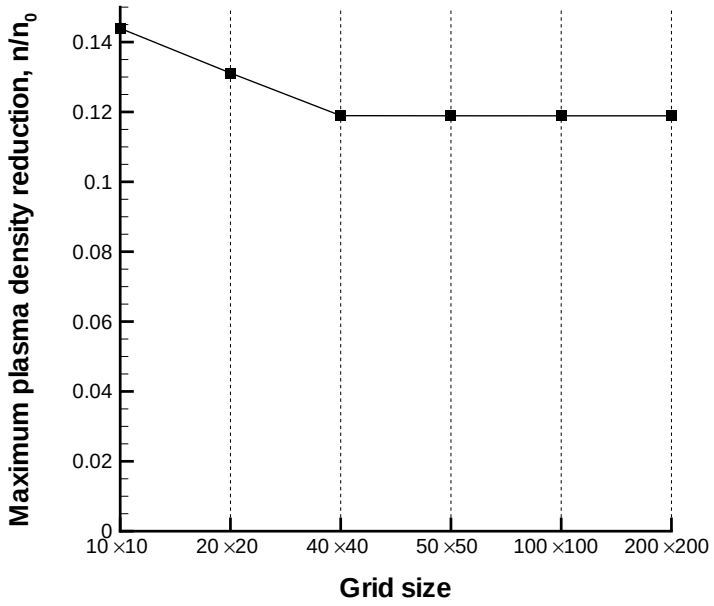

Figure 4.4: Grid convergence of the ExB layer model.

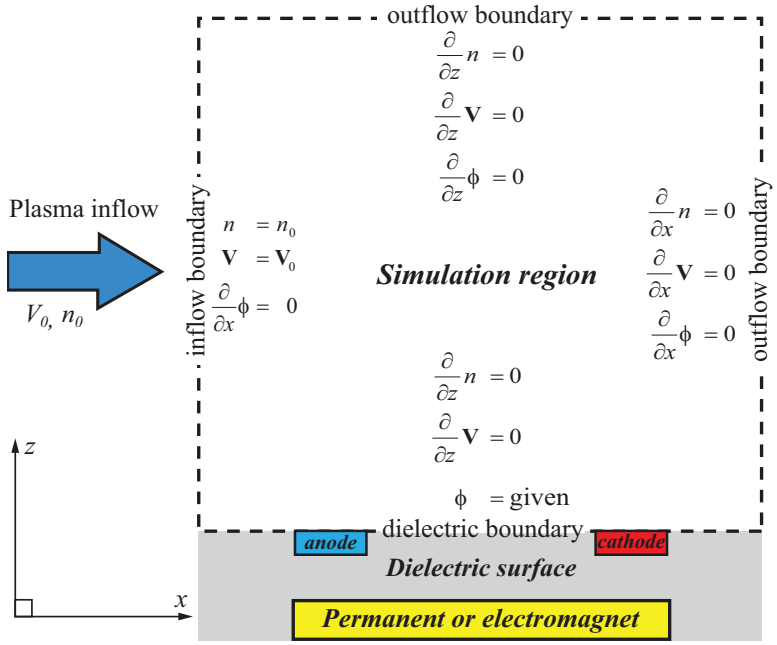

Figure 4.5: Applied boundary conditions for the two-dimensional ExB layer MHD model with a schematic of the simulation domain.

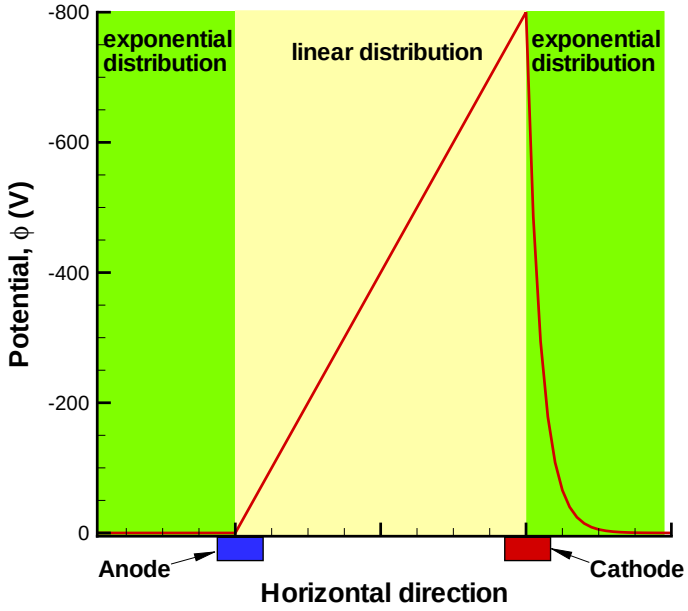

Figure 4.6: Applied potential boundary condition between the two electrodes.

between the two electrodes and an exponential distribution beyond the electrodes for numerical stability. Since the potential is zero beyond the cathode, this region does not affect the plasma flow of the ExB layer [83].

4.3 Magnetic Field Configuration

The applied magnetic-field is generated by an electromagnet with a low magnetic Reynolds number assumption. The magnetic Reynolds number, R_M, is a measure of the coupling between the motion of the magnetic field line and the motion of the conducting fluid. The typical magnetic Reynolds number is order of 10^{-3} in a weakly ionized gas, when the ionization rate is less than 1 % [59]. When the magnetic Reynolds number is much smaller than unity, the magnetic field is not greatly affected by the fluid motion [43, 83]. This means the magnetic field induced by current is negligible compared with the imposed magnetic field. Therefore, the

magnetic field is entirely determined by the applied electromagnet.

The applied magnetic field must satisfy a divergence free magnetic field condition [84]:

$$\nabla \cdot \vec{\mathbf{B}} = 0 \tag{4.21}$$

This constraint expresses the absence of magnetic monopoles. In order to calculate the magnetic field from Eq. 4.21, a magnetic field stream function, λ, is employed which is calculated from

$$\vec{\mathbf{B}} = \nabla \times \vec{\lambda} \tag{4.22}$$

where $\vec{\lambda} = (0, \lambda, 0)$. For the two-dimensional case,

$$B_x = -\frac{\partial \lambda}{\partial z} \text{ and } B_z = \frac{\partial \lambda}{\partial x} \tag{4.23}$$

The magnetic stream function is constant along a magnetic field line. In other words, the magnetic stream function indicates the direction of the magnetic field. The definition of the magnetic stream function gives a Poisson equation from the divergence free condition, Eqn. 4.21 as follows:

$$\begin{aligned} \nabla \cdot \vec{\mathbf{B}} &= \nabla \cdot \left(\nabla \times \vec{\lambda} \right) \\ &= \frac{\partial^2}{\partial x^2}\lambda + \frac{\partial^2}{\partial z^2}\lambda = 0 \end{aligned} \tag{4.24}$$

Solving Eq. 4.24 gives the magnetic-field distribution for the ExB layer.

Equation 4.24 is solved using the alternating direction implicit (ADI) method. The boundary conditions for Eq. 4.24 are taken from magnetic-field data measured in the Plasmadynamics and Electric Propulsion Laboratory (PEPL) at the University of Michigan. Figure 4.7 shows the configuration of the applied two-dimensional

magnetic-field which is normalized by the maximum magnetic field strength. As can be seen, the maximum magnetic-field strength occurs near the two electrodes. In this case, the magnetic field strength can be controled by changing the coil current but the configuration of the magnetic field does not depend on the magnetic-field strength [85].

4.4 Simulation Results of the Two-dimensional ExB layer

This section presents simulation results from the two-dimensional ExB layer model. The ExB layer model uses a calculated magnetic field configuration which is based on experimental data. The applied magnetic configuration is presented in Section 4.3. The plasma number density is normalized by the plasma density of the flow field, n_0, and this ratio is called the plasma density reduction. A strong plasma density reduction indicates a large effect of the applied ExB layer.

The purpose of this simulation is the estimation of the maximum density reduction and the size of the effectiveness region of the ExB layer. The simulation uses a plasma of argon with a constant background neutral pressure of 1 mTorr and 4.2×10^{16} m^{-3} bulk plasma number density with 1000 m/s bulk velocity. This condition corresponds to a condition of the ExB layer mitigation scheme investigated experimentally [71]. In the ExB layer experiment, the test chamber is filled with a helicon plasma, thus the entire chamber can be considered a plasma layer. In order to analyze the experimental condition, the generation of a plasma layer is not considered and the entire simulation domain is assumed to be a plasma layer. This situation is quite different from a hypersonic flow condition because the plasma layer is typically about $1 \sim 2$ cm, as presented in Chapter III. However, the simulation of the ExB layer will still give results on the effectiveness area of the ExB layer.

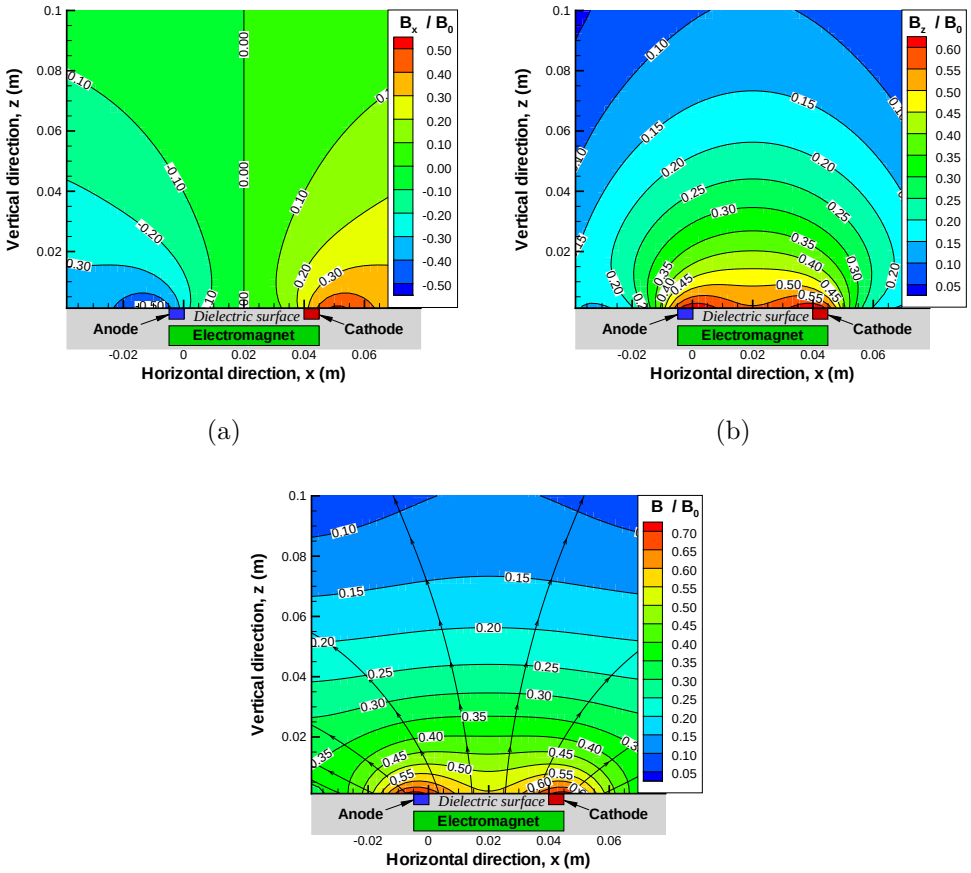

(a)

(b)

(c)

Figure 4.7: The applied magnetic field configuration which is normalized by the maximum magnetic field strength B_0 (a)Horizontal direction magnetic field configuration, B_x/B_0 (b)Vertical direction magnetic field configuration, B_z/B_0 (c)Normalized magnetic field strength configuration with the magnetic field lines.

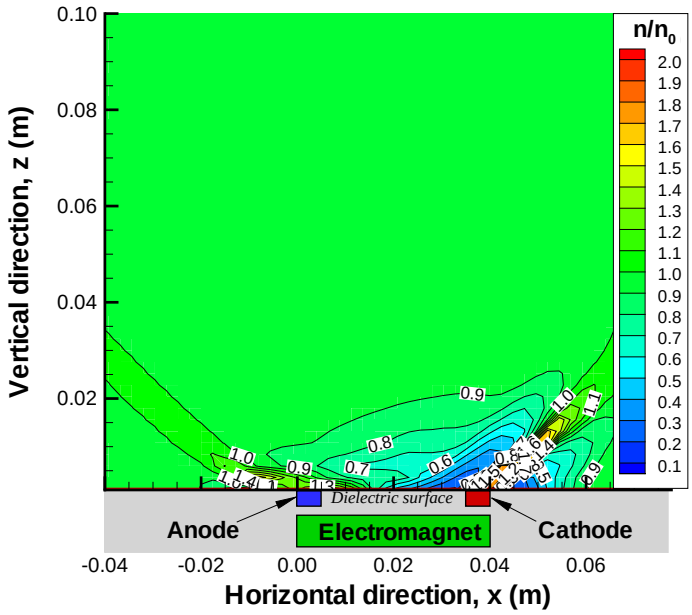

Figure 4.8: A distribution of plasma density reduction ratio. The initial plasma density, n_0 is 4.2×10^{16} m^{-3} and the initial neutral pressure is 1 mTorr. A -800 V potential is applied with 0.07 T magnetic field strength

When the effectiveness area is larger than the plasma layer, the applied ExB layer can penetrate the plasma layer to allow for communication during radio blackout.

The distribution of the plasma density reduction in the ExB layer is shown in Figure 4.8 which has two increased density regions, beyond the anode and the cathode. The increased density region of the cathode is primarily caused by the potential beyond the cathode. The potential beyond the cathode is assumed to exponentially drop to 0 V. This is quite reasonable because the area beyond the cathode is assumed to be a vacuum condition. The sharp drop in potential of this area creates a large negative electric field along the x- direction. Because of the negative electric field, the ions are decelerated in this direction and the plasma density is increased. The increased density region near the anode is due to the divergence of the applied magnetic field.

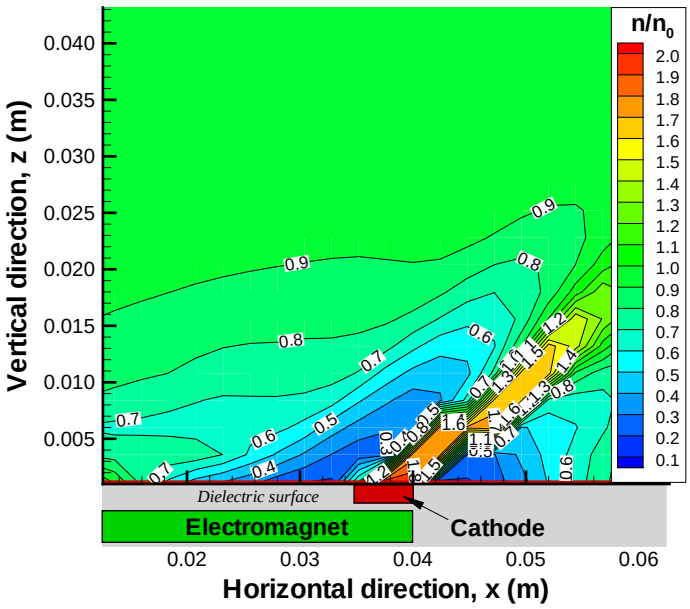

Figure 4.9: A close-up of the distribution of plasma density reduction ratio near the cathode.

Figure 4.8 and 4.9 show that the strongest plasma density reduction occurs near the cathode, which provides the optimal location for the antenna. In this case, the required electrical power for the ExB layer is about 46.2 W when a permanent magnet is used to provide a magnetic field. As can be seen in Figure 4.8, the effects of the plasma density reduction decrease with distance from the wall.

Figure 4.10 shows the plasma density reduction profile in greater detail. The strongest plasma density reduction occurs near the cathode and the ExB layer can effectively reduce the plasma density up to approximately 2 cm above the surface. This demonstrates a possibility for mitigating the radio blackout problem, because the plasma density peak in the RAM-C flight is at about 1.2 cm from the vehicle surface.

Figures 4.8 and 4.10 also show that the applied ExB layer only affects the plasma

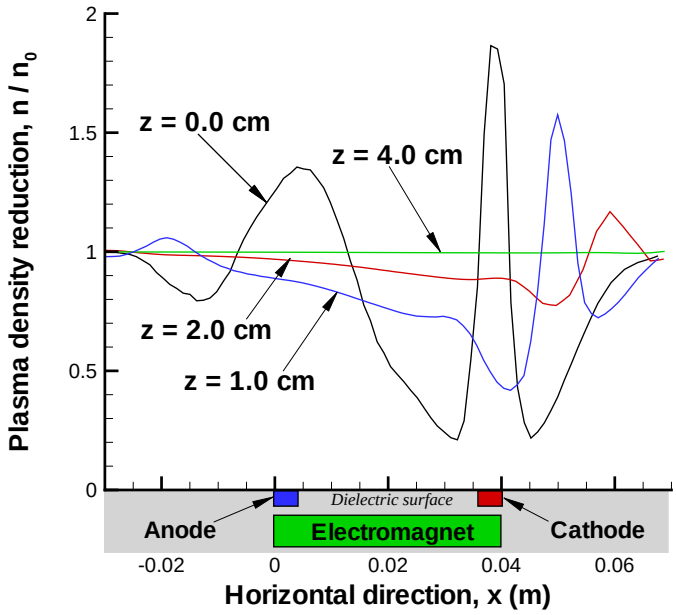

Figure 4.10: The distributions of the plasma density reduction ratios at several vertical positions: z = 0.0 cm, 2.0 cm, and 4.0 cm.

density near the cathode because of the potential distribution as shown in Figures 4.11 and 4.12. The potential sharply changes near the cathode, thus giving a strong electric field for ion acceleration. This means the ExB layer will not disturb the entire flow. This is an important fact for practical application because the applied ExB layer gives a window for communication without any effect on the vehicle's aerodynamics.

As a mitigation scheme, the ExB layer has two important parameters in terms of communication through a plasma layer, namely plasma density reduction and the size of the communications window. First, the density reduction required to manipulate a plasma layer is based on the peak plasma density and the radio-wave frequency used for communication. As shown in Chapter I, various radio-wave frequencies are used for different applications. This means that each application requires a different

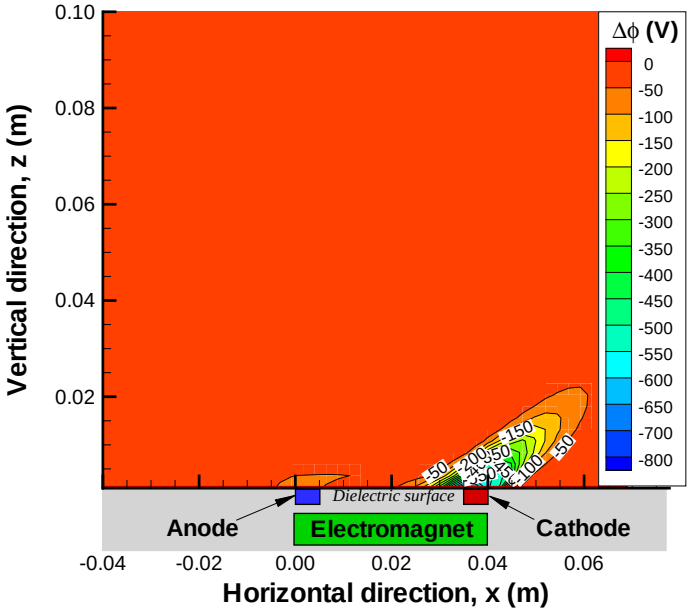

Figure 4.11: Potential distribution of the ExB layer. The initial plasma density, n_0 is 4.2×10^{16} m^{-3} and the initial neutral pressure is 1 mTorr. A -800 V potential is applied with 0.07 T magnetic field strength.

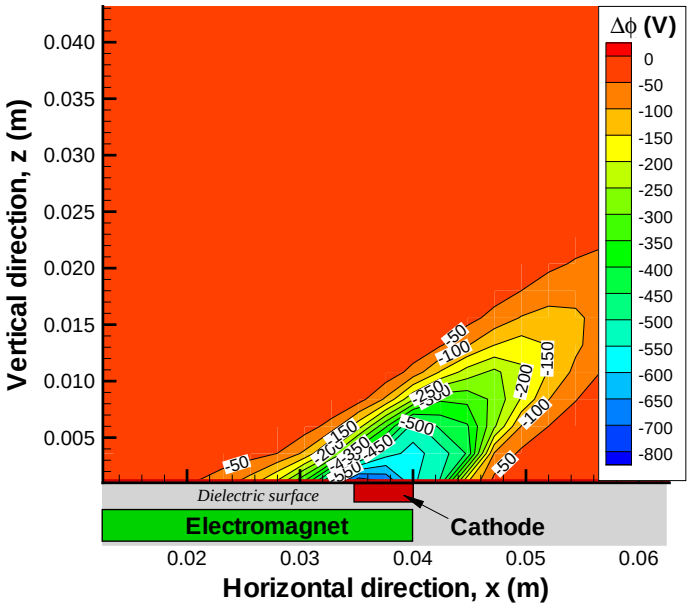

Figure 4.12: A close-up of potential distribution near the cathode.

plasma density reduction to solve radio blackout. When the plasma number density is higher than the critical number density, a radio-wave has infinite attenuation in the plasma layer. Therefore the plasma number density should be reduced at least below the critical number density [5, 6, 7, 12].

Another important parameter is the size of the communications window and in particular, the thickness of the plasma layer which is effectively manipulated by the ExB layer. The boundary of the communications window is determined by the required plasma-density reduction. The region effectively manipulated by an ExB layer should be larger than the thickness of the plasma layer that prevents communication. As a mitigation scheme, the effective area of an ExB layer, which is the communications window, can be found from Figures 4.8 and 4.10 which show the plasma density reduction in the ExB layer. For a 1.5 GHz GPS signal, the required density reduction is about 0.7 for a 4.2×10^{16} m^{-3} plasma density of the flow field. Therefore, the simulation result shows that the applied ExB layer can effectively reduce the plasma density up to approximately 2 cm above the surface to solve radio blackout of GPS navigation. When the thickness of the plasma layer is smaller than 2cm, the created "window" can penetrate the plasma layer for GPS communication. For the RAM-C flight test, the thickness of the plasma layer is approximately $1 \sim 2$ cm, but this depends on the altitude [14, 15]. For the low-altitude case, the plasma layer is thin and has a high peak plasma density. At high altitudes, the plasma layer is thicker and the peak plasma density is lower than for the low-altitude case.

4.4.1 Magnetic Field Effectiveness

In this section, the effectiveness of the magnetic field is studied in terms of the plasma density reduction. A comparison is provided for results obtained with the

one-dimensional constant magnetic field and the two-dimensional magnetic field. The two-dimensional magnetic field uses a calculated configuration which is based on experimental data as presented in Section 4.3.

Figure 4.13 shows the plasma density reduction ratio profiles obtained with the two different magnetic fields. As shown, the one-dimensional magnetic field predicts a stronger plasma density reduction than the two-dimensional magnetic field configuration. This difference is due to the difference in the magnetic field strength between the two configurations, as shown in Figure 4.14. The strength of the two-dimensional magnetic field configuration decreases with distance from the wall surface. However, the magnetic-field is constant in the one-dimensional case.

As discussed in Chapter III, the one-dimensional ExB layer model predicts a stronger plasma density reduction with a higher magnetic field. The two-dimensional ExB layer MHD model gives similar results. However, the maximum magnetic field strength is limited because of the weight of the permanent magnet. Although the higher magnetic field guarantees a larger window for communication, it has a negative effect on vehicle performance due to the heavy weight. Figure 4.15 shows the plasma density reduction in the ExB layer as a function of magnetic field strength. The plasma density reduction ratio grows stronger with magnetic field strength. However, the rate of increase in the plasma density reduction becomes smaller at higher magnetic fields. In this case, the optimal field strength is around 0.2 T.

4.4.2 Electric Field Effectiveness

The electric field is another parameter that affects the plasma density reduction in the applied ExB layer. As discussed in Chapter III, the one-dimensional ExB layer model demonstrated that a higher potential drop gives a stronger plasma density

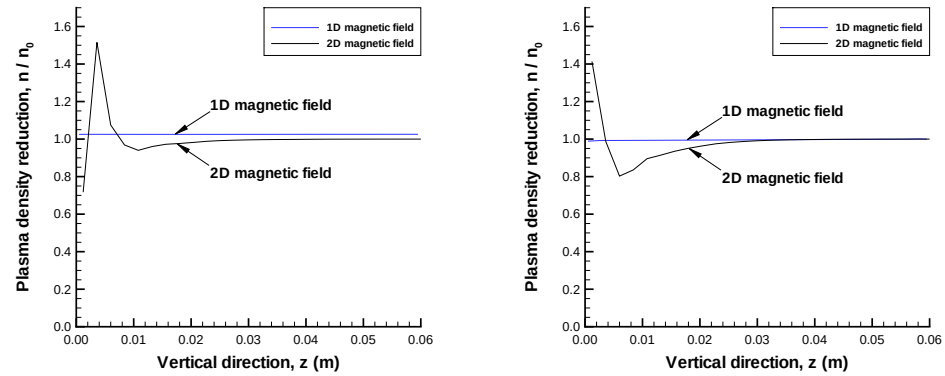

(a)

(b)

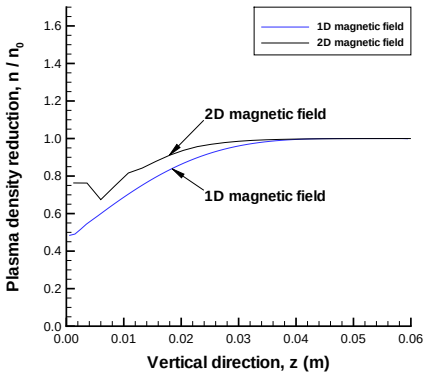

(c)

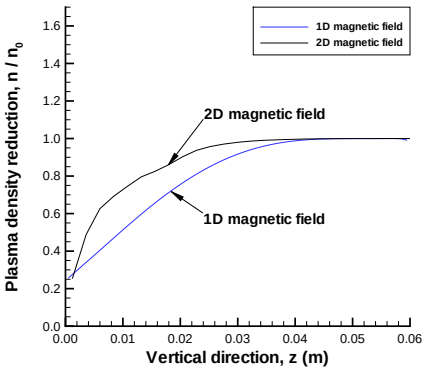

(d)

Figure 4.13: Effectiveness of the magnetic field configuration of 1D and 2D magnetic fields (a) z = 0.1 cm (b) z = 1.4 cm (c) z = 2.7 cm (d) z = 4.0 cm

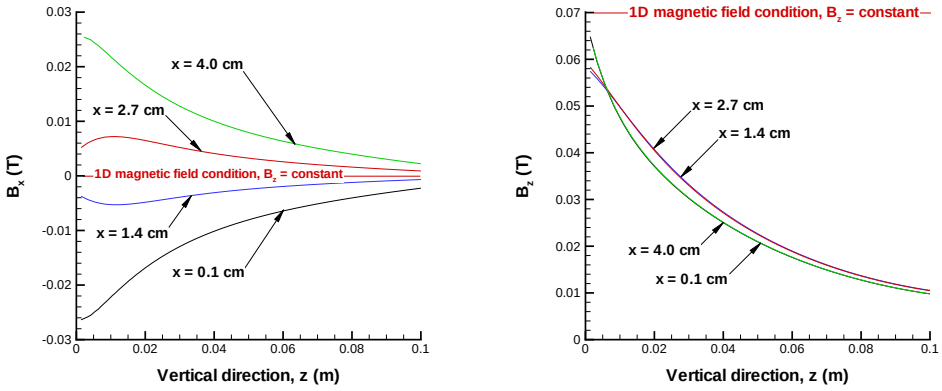

(a) (b)

Figure 4.14: Magnetic field distributions for the 1D and 2D magnetic fields for the B = 0.07 T case: (a) x-direction magnetic field strength, B_x (b) z-direction magnetic field strength, B_z

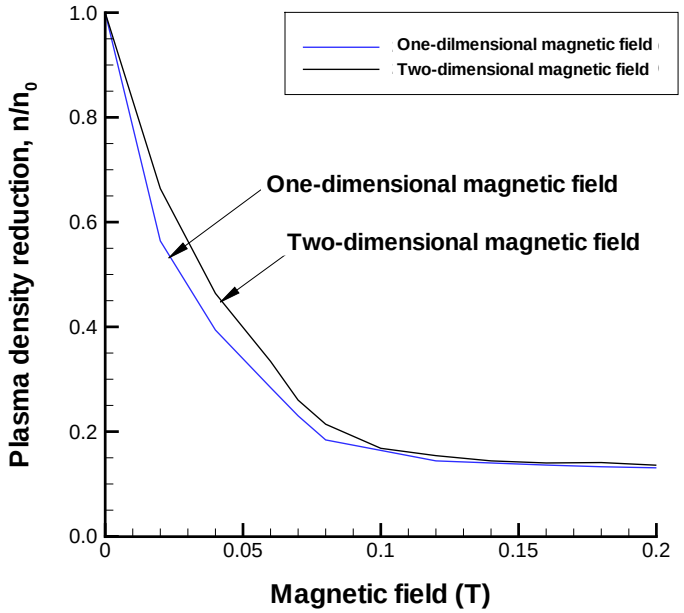

Figure 4.15: Plasma density reduction ratio as a function of the magnetic field strength. The initial plasma density, n_0 is 4.2×10^{16} m^{-3} and the initial neutral pressure is 1 mTorr. A -800 V potential drop is applied.

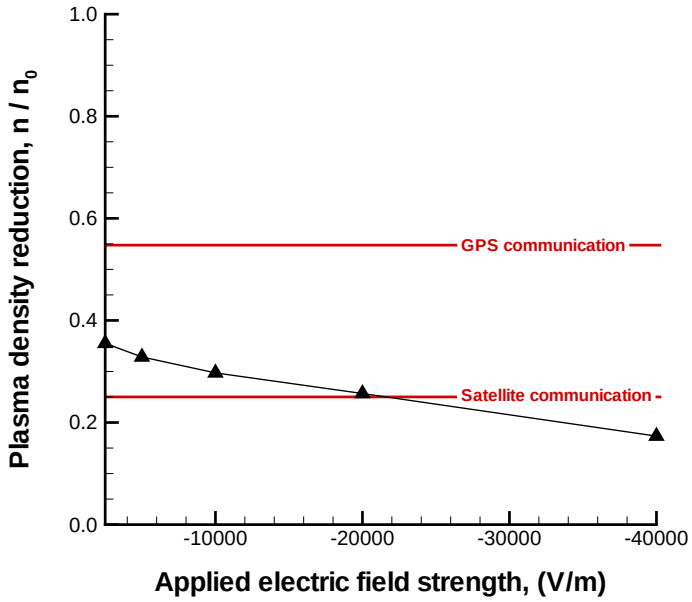

Figure 4.16: The plasma density reduction as a function of the applied electric field at the cathode. The initial plasma density, n_0 is 4.2×10^{16} m^{-3} and the initial neutral pressure is 1 mTorr. A 0.07 T magnetic field strength is applied.

reduction but the maximum applicable potential drop is limited due to the electrode arcing problem. For the two-dimensional ExB layer MHD model, the effectiveness of the electric field is shown in Figure 4.16.

As can be seen, density reduction is improved by a higher electric field. Furthermore, Figure 4.16 shows that the change in the plasma density reduction becomes smaller at higher electric fields. Thus, there is an optimum value for the electric field in order to enable communication through the plasma layer.

4.5 Conclusion

This chapter proposed a two-dimensional ExB layer model and further demonstrated the possibility of the ExB layer as a blackout mitigation scheme. The two-

dimensional approach is important because it shows the optimal location of the transmit antenna and the effective area of the ExB layer.

The optimal location of the antenna can be determined using the distribution of the plasma density reduction. The numerical result shows the maximum density reduction occurs near a cathode. The density reduction should be stronger than the critical density reduction which was presented in Chapter III. To communicate through the plasma layer, the effective area of the applied ExB layer must be larger than the size of the antenna and at a distance greater than that of the peak plasma density in the plasma layer from the vehicle surface. The simulation results show that the applied ExB layer can effectively reduce the plasma number density outwards to approximately 2 cm from the surface. These are very promising results for mitigating radio blackout, since the plasma density peak in the RAM-C flight is at about $1 \sim 2$ cm from the vehicle surface [14, 15].

The overall efficiency of the electromagnetic scheme for re-entry telemetry is affected by the magnetic and electric fields. The reduced plasma density and area can be controlled by changing magnetic field strength and electric field. Significant density reduction can be obtained with a high magnetic field and electric field. Therefore, the application of electric and magnetic fields could allow radio communication through a hypersonic plasma layer.

CHAPTER V

Model Results and Experimental Comparisons

This chapter assess the simulation results through comparison with experimental data and with analytical solutions, which were presented in Chapter III. Experimental study of the ExB layer mitigation scheme was carried out by the Electro-Dynamic Applications (EDA) in the Plasmadynamics and Electric Propulsion Laboratory (PEPL) at the University of Michigan with a helicon plasma source running argon. This chapter also presents a comparison of the one-dimensional ExB layer model and the two-dimensional model in order to demonstrate the consistency of the ExB layer model. Under the low potential drop condition, the one-dimensional ExB layer model predicts a slightly weaker plasma density reduction than does the two-dimensional ExB layer model because the one-dimensional model assumes a constant current density in the ExB layer. However, the two models are in agreement in the high potential drop condition. The suggested models also have good agreement under the strong magnetic field condition.

5.1 Experimental Setup

An experimental study was performed to validate the plasma mitigation technique based on the ExB layer [53, 66, 71]. Figure 5.1 shows the experimental setup

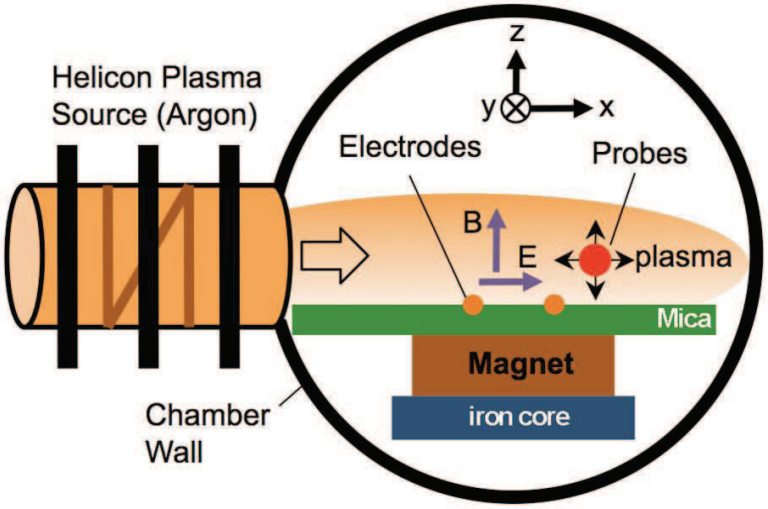

Figure 5.1: Diagram of experimental setup [71].

that is consistent with the theoretical model shown in Chapters III and IV. As can be seen, the experiment is mainly composed of a helicon plasma source, an electromagnet, the two electrodes (the anode and the cathode) and three types of probes to measure plasma density versus position. A helicon plasma source is used to create a high-density plasma. The electromagnet and electrodes are constructed around an antenna embedded in a mica sheet which simulates a vehicle body. Probes measure the electron number density to indicate whether the applied ExB layer can manipulate the plasma layer.

Experiments were carried out in the Cathode Test Facility (CTF) at the University of Michigan. The CTF chamber is designed to simulate a range of plasma and neutral densities representing a range of altitudes for re-entry vehicles [66]. Figure 5.2 shows the CTF, which is a 2 m long by 0.6 m diameter vacuum chamber. The CTF chamber is pumped by a 135 CFM mechanical vacuum pump for roughing and a CVI TM500 cryogenic vacuum pump with a measured pumping speed of 1,500 l/s [86].

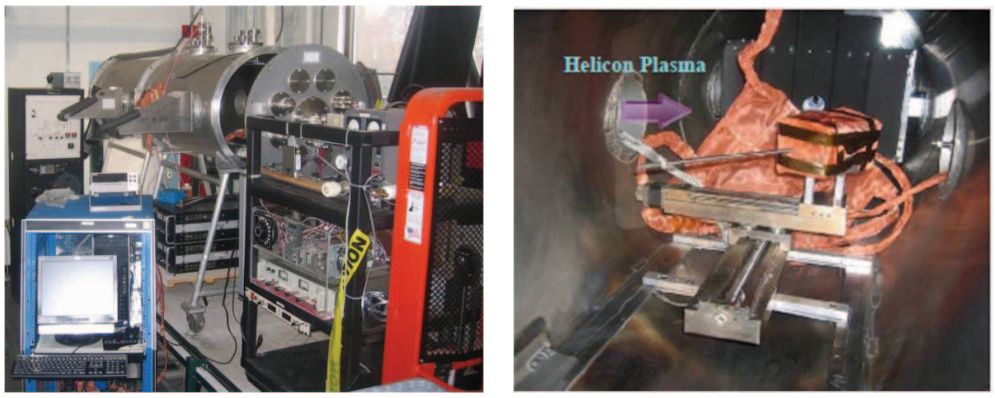

(a) (b)

Figure 5.2: Cathode test facility chamber for experiment (Courtesy of Plasmadynamics and Electric Propulsion Laboratory (PEPL) at the University of Michigan) (a)PEPL's CTF chamber at the University of Michigan (b)An inside of the CTF chamber showing the experimental setup.

The experiment uses an argon helicon plasma, which can very efficiently generate high density plasma using RF power[87] and the number of neutral particles in the plasma can be varied. As shown in Figure 5.2 (b), to inject a high-density plasma over a test region, the helicon plasma source is mounted horizontally on the front left side flange of the CTF. The helicon plasma source is able to generate plasma densities up to 10^{18} m^{-3} [66] which corresponds to the 81 km altitude condition of RAM-C.

As schematically shown in Figure 5.1, to provide the electric field the experimental setup has two electrodes, namely an anode and a cathode, which are 1/8 inch stainless steel tubes. Stainless steel was chosen to reduce sputtering and a tube electrode was used to reduce arcing effects to the chamber walls and instruments. The anode is grounded and the cathode is variably biased up to -2 kV with a power supply capable of sourcing up to 10 A.

Figures 5.3 (a) and (b) show the ferrous iron core of the magnet, and the core with windings. The electromagnet uses 7 parallel windings and is a hand wound solenoid

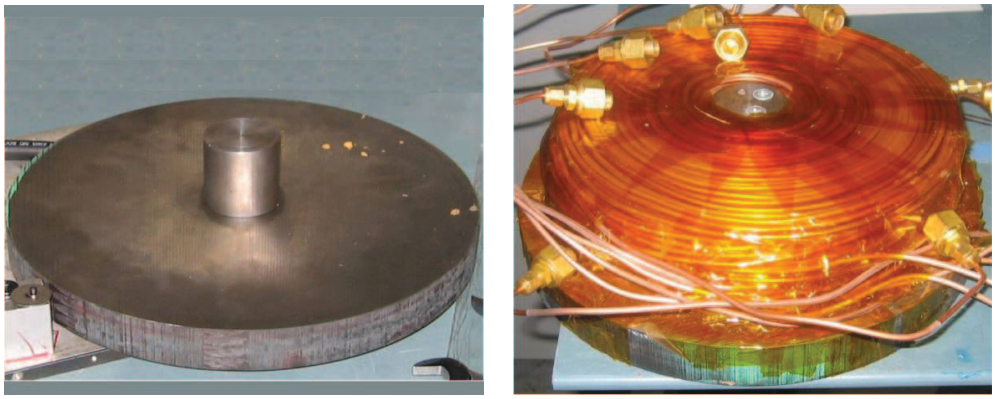

(a) (b)

Figure 5.3: Electromagnet for experiment (Courtesy of PEPL at the University of Michigan and EDA)(a) a blank core (b) a final wound magnet before installation

constructed with internally water cooled copper tubing around an iron core. The coil layers are insulated and fixed in place with Kapton tape. The magnet is powered by a 300 A - 8 V power supply that is capable of producing fields at the center surface of up to 0.6 T. The magnetic fields of both the base magnet and the helicon magnets are characterized with an FW Bell 7030 3 axis high resolution magnetic field probe. As shown in Figure 5.1, the iron core solenoid electromagnet beneath the surface of the Mica sheet generates the magnetic field, while the electric field is created by linear electrodes embedded into the Mica on either side.

The plasma is instrumented alternately with a Langmuir probe, a resonance probe, and an RF transmission probe to improve the accuracy of the measurement and to provide cross verification of the plasma density. To measure the plasma density at the different positions these probes are swept throughout the area of interest via a set of three translation tables. A Hiden ESPION series electrostatic Langmuir probe system is used to measure the plasma density and potential. The Langmuir probe is RF compensated for 13.56 MHz, the operational frequency of the plasma

source.

Figure 5.4 shows a hairpin style resonance probe tuned to the plasma frequency of about 900 MHz. The hairpin antenna approach has higher sensitivity and is less susceptible to measurement ambiguity due to probe resonances with the vacuum chamber and/or measurement circuitry [88]. The hairpin resonance probe can also measure the conductivity of the plasma by looking at the relative change of resonance width [89]. In this probe, the plasma density can be determined via the ratio of the free space to plasma resonance frequencies of the hairpin antenna. Therefore, the plasma number density can be calculated as [90, 91]:

$$n_e = \frac{f_r^2 - f_0^2}{0.81} \times 10^{-2} \tag{5.1}$$

where f_r is the resonance frequency of the hairpin in Hz, and f_0 is the vacuum resonance frequency in Hz. The resonance frequency, f_{res}, of the antenna is given by the following equation:

$$f_r = \frac{c}{4L\sqrt{\varepsilon_r}} \tag{5.2}$$

where c is the speed of light, L is the length of the antenna and ε_r is the relative dielectric constant of the surrounding media. In vacuum, $\varepsilon_r = 1$ and the vacuum resonance frequency f_0 is simply $\frac{c}{4L}$. The resonant frequency of the antenna can be changed by adjusting its length. To modify the density determination to a magnetized plasma, the following expression can be used for the relative dielectric constant, ε_r [91].

$$\varepsilon_r = \left(1 - \frac{\omega_p^2}{\omega^2} \cdot \frac{\omega^2 - \omega_p^2}{\omega^2 - \left(\omega_p^2 + \omega_c^2\right)}\right)^{1/2} \tag{5.3}$$

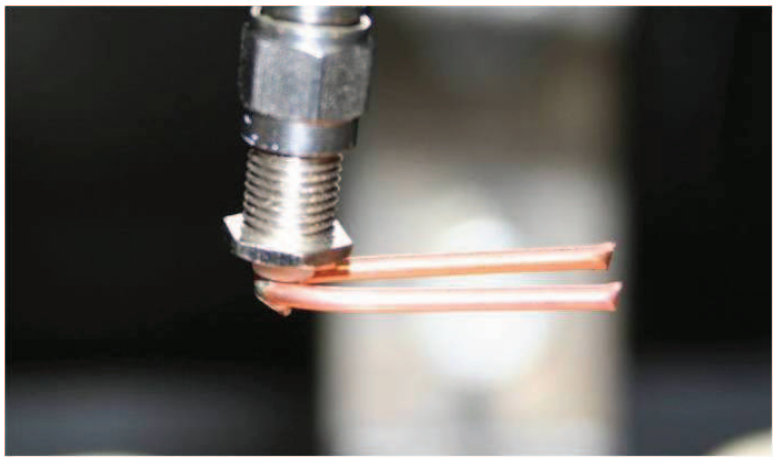

Figure 5.4: Hairpin resonance probe which is custom made at EDA used to measure plasma density changes (Courtesy of EDA)

where ω_p is the electron plasma frequency, and $\omega_c = 2\pi f_c$ is the electron cyclotron frequency.

Figure 5.5 shows an RF transmission probe that consists of two antennas 2 cm apart. The diagnostic antennas are custom made short dipoles at test frequencies of up to 1.5 GHz. The surfaces of the RF transmission probe are insulated with Kapton tape to reduce arcing. These are configured in a pair on the probe body to allow translation in the same fashion as the Langmuir and resonance probes [92]. Between these antennae, an HP 8753D network analyzer with a frequency range of 30 kHz to 3 GHz and a sensitivity down to -60 dB is used to measure S11 (Reflection Loss) and S21 (Gain) parameters with time gating applied to reduce the influence of internal reflections. Experimentally, the measured S21 response for the RF transmission probe shows a decrease from -33 dB W to -38 dB W at 1.5 GHz, as the density varied from 6.0×10^{15} to 3.6×10^{16} m^{-3}. The probe provides sufficient sensitivity to resolve density changes of about one tenth of magnitude.

The probe techniques used to gather experimental data are illustrated in Figure 5.6. Also shown are the RF filters and DC blocks used to protect the equipment

Figure 5.5: RF transmission probe for plasma density measurement (Courtesy of EDA)

from the high levels of RF power generated by the helicon source, and the occasional high voltage arcs from the electrodes. The measurements are calibrated in air to eliminate the effect of these protective devices on the final readings. The Langmuir probe measurement allows plasma density calculation via I-V curves [53, 93]. The Transmission Probe measures transmitted RF power S21, while the Resonance Probe measures reflected RF power S11.

5.2 Assessment of the ExB Layer Models

This section assesses the ExB layer models in relation to analytical solution and experimental data. The analytical solution is described in Chapter III for the simplified one-dimensional case. The experimental data is obtained from PEPL of the University of Michigan and EDA. The experiment has an argon plasma density of 4.2×10^{16} m^{-3} with 1 mTorr neutral pressure. To maintain consistency, the simulation uses the same flow field condition. The comparison with the analytical solution and experimental will give an indication of the accuracy of the suggested ExB layer models, the one-dimensional and two-dimensional models. The two suggested ExB

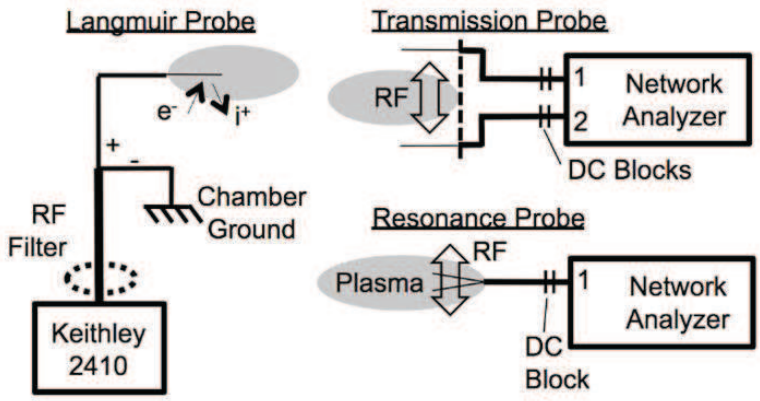

Figure 5.6: Probe techniques used for plasma density measurements [71]. The Langmuir probe measurement allows plasma density calculation via I-V curves. The Transmission Probe measures transmitted RF power S21, while the Resonance Probe measures reflected RF power S11.

layer models are also compared to determine whether they are consistent.

5.2.1 Analytical Solution

The analytical solution for the simplified one-dimensional ExB layer model is presented in Chapter III. Comparison with the analytical solution is useful to demonstrate the accuracy of the numerical solution of the one-dimensional ExB layer model. Since the analytical solution does not include the collision drag term, this term is neglected in the numerical solution. Therefore, the results of both the analytical and the numerical solutions are obtained under the same condition.

Figure 5.7 shows a comparison of the one-dimensional ExB layer model with the analytical solution. In this case, the flow condition corresponds to the experiment, in which the inflow plasma number density is 4.6×10^{16} m^{-3} with 1 mTorr neutral pressure and the applied current density is 100 A/m^2. As can be seen, the one-dimensional ExB layer model gives very good agreement with the analytical solution. Both results show that the density reduction increases with magnetic field strength. The density reduction reaches a plateau at a magnetic field of about 0.2 T.

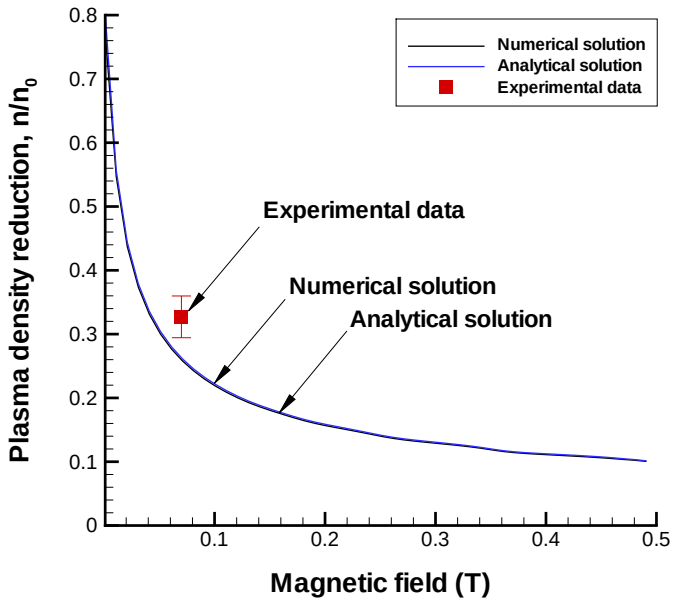

Figure 5.7: Assessment of the one-dimensional ExB layer model by comparison with the analytical solution at the experimental condition which is 4.6×10^{16} m^{-3} plasma number density with 3 mTorr neutral pressure at 100 A/m^2 current density.

5.2.2 Experimental Data

The ExB layer mitigation scheme experiment was performed by EDA and PEPL at the University of Michigan. As presented in Section 5.2, a helicon plasma source of argon is used to simulate the plasma layer around a hypersonic vehicle. Since the CTF chamber is completely filled with argon plasma, the entire test chamber can be considered as a plasma layer.

Figure 5.8 compares the experimental measurements of plasma density reduction with the two-dimensional ExB layer model results. In this case, the applied potential drop is -800 V with a 0.07 T magnetic field strength. As can be seen, the ExB layer model agrees well with the measured data near the two electrodes. However, the model usually predicts stronger plasma density reduction ratios than the experimental results at the x = 2.7 cm and 4.0 cm positions. This is caused by a difference in the magnetic field configuration.

Figures 5.9 and 5.10 show the magnetic field configurations for the experiment and simulation. In the experiment, the magnetic field data is measured with an FW Bell 7030 3-axis high-resolution magnetic field probe. For the simulation, the applied magnetic field is obtained by solving a Poisson equation with the experimental data as boundary conditions as discussed in Chapter IV. As can be seen, the magnetic field strength of the simulation is slightly higher than that of the experiment for both the x and z directions. The reason for this is that the simulation assumes the magnetic field is two-dimensional, whereas the experimental magnetic field configuration is axially symmetetric.

Both numerical and experimental data in Figure 5.8 show that the applied ExB layer only affects the plasma density near the cathode. This means that an ExB layer will not disturb the entire flow. This is an important factor for practical application

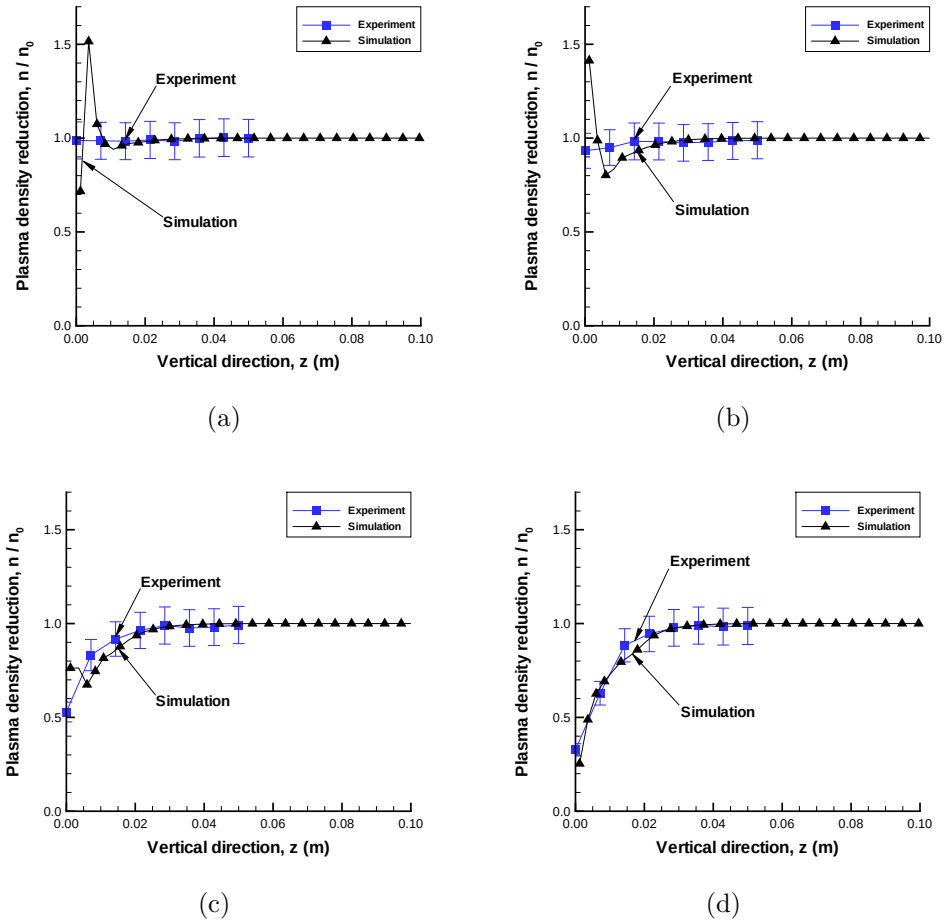

Figure 5.8: Comparison between numerical and experiment results : (a) x = 0.1 cm (b) x = 1.4 cm (c) x = 2.7 cm (d) x = 4.0 cm

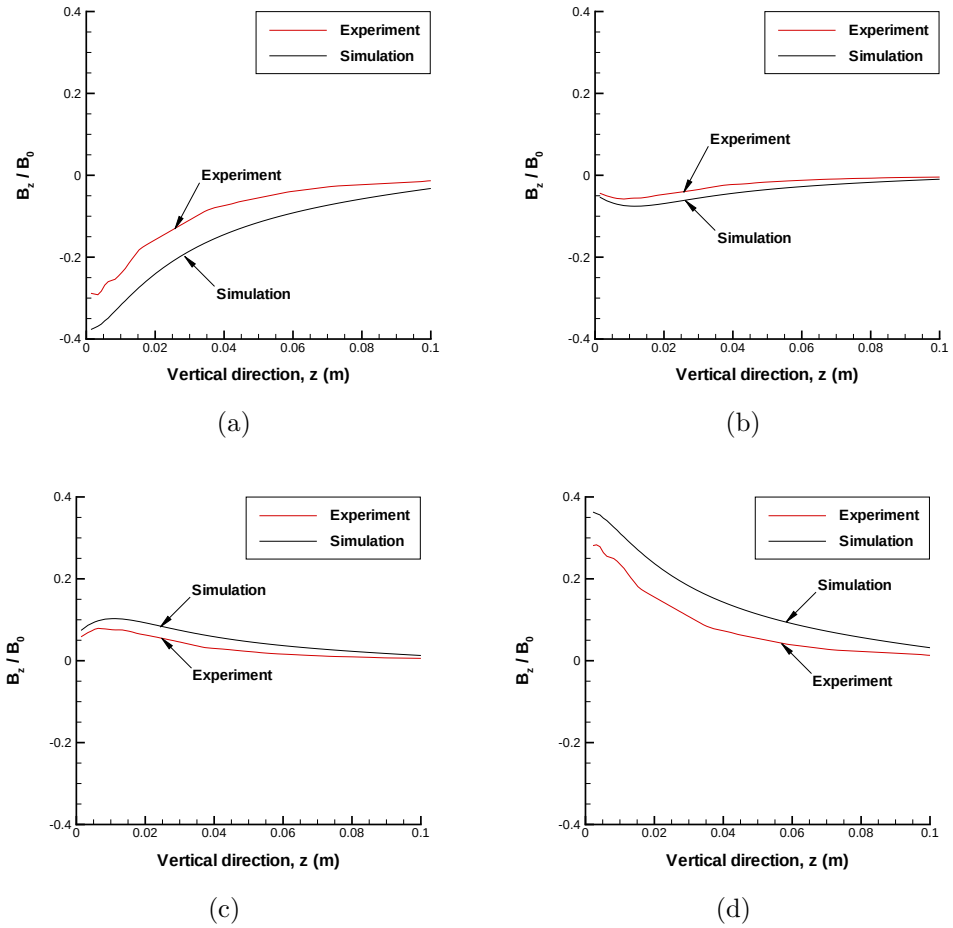

Figure 5.9: Comparison between numerical and experimental data for the x-component magnetic field: (a) x = 0.1 cm (b) x = 1.4 cm (c) x = 2.7 cm (d) x = 4.0 cm

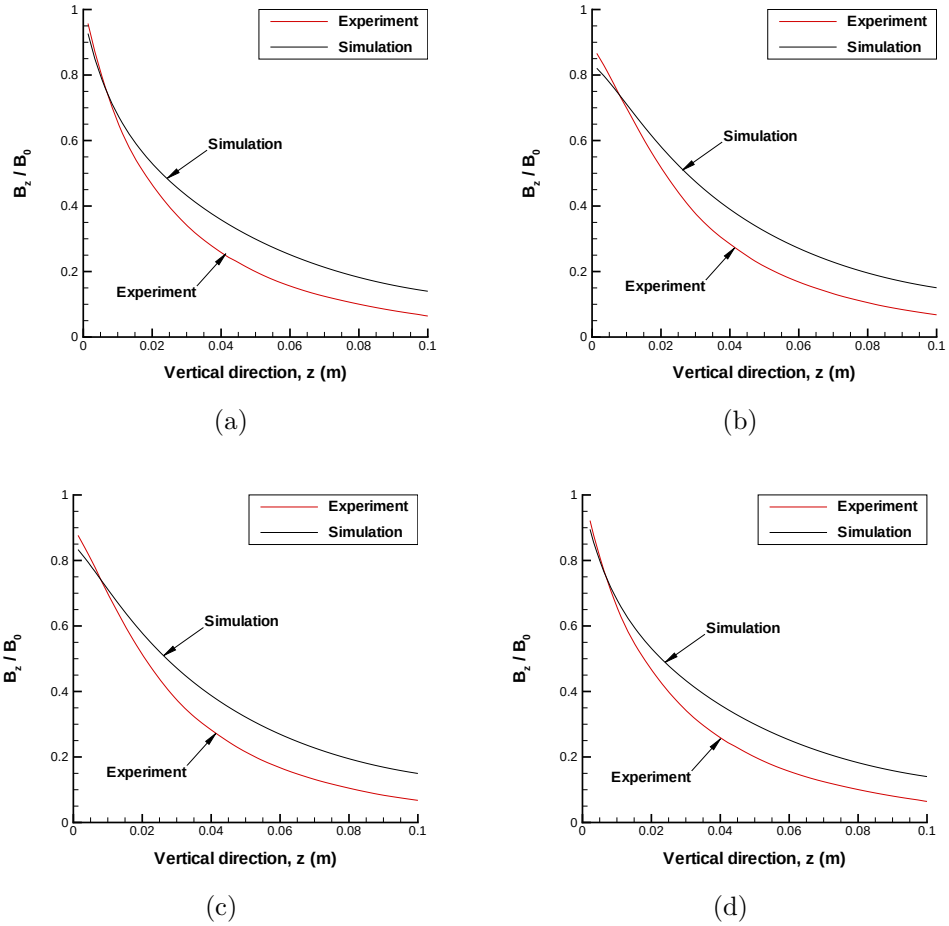

Figure 5.10: Comparison between numerical and experimental data for the z-component magnetic field: (a) x = 0.1 cm (b) x = 1.4 cm (c) x = 2.7 cm (d) x = 4.0 cm

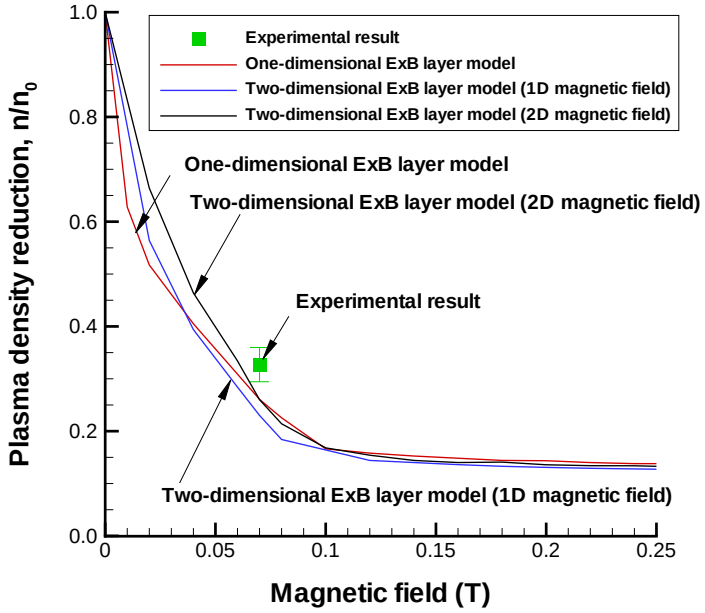

Figure 5.11: Consistency of one-dimensional and two-dimensional ExB layer models at experimental condition, 4.6×10^{16} m^{-3} plasma number density with 1 mTorr neutral pressure at -800V potential drop.

because an applied ExB layer should give a window for communication without any effect on a vehicle's aerodynamics.

5.3 Model Consistency

Figure 5.11 shows a comparison of the one-dimensional and two-dimensional ExB layer MHD models as a function of the magnetic field strength. As can be seen, the plasma density reduction ratio strengthens with magnetic field for both models. However, the rate of increase in plasma density reduction becomes smaller for strong magnetic fields. The optimized plasma density reduction ratio is given by the 0.2 T magnetic field condition. It is also interesting that all models are in agreement in the case of large magnetic field, stronger than 0.2 T.

Figure 5.12 compares the one-dimensional and two-dimensional ExB layer MHD

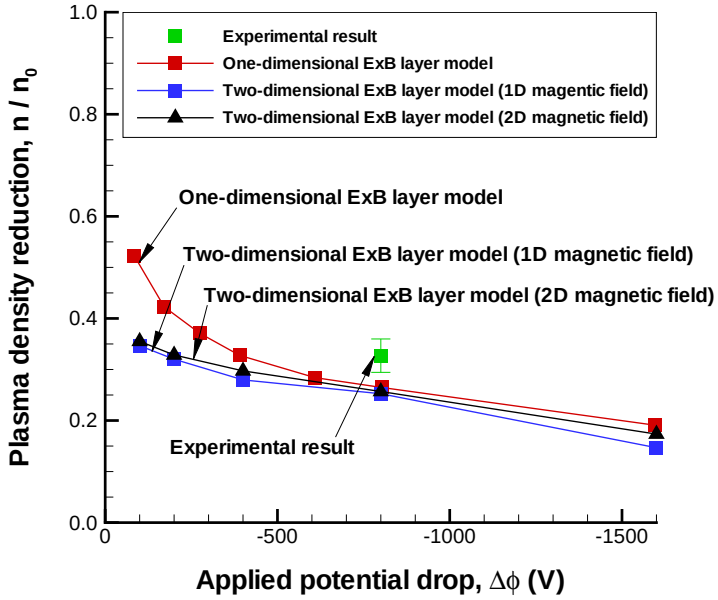

Figure 5.12: Consistency of one-dimensional and two-dimensional ExB layer models at experimental condition, 4.6×10^{16} m^{-3} plasma number density with 1 mTorr neutral pressure at 0.07 T magnetic field.

models as a function of the potential drop. Under the low potential drop condition, the one-dimensional ExB layer model predicts a slightly weaker plasma density reduction than the two-dimensional ExB layer model because the one-dimensional model assumes a constant current density in the ExB layer. However, the two models are in agreement for the high potential drop condition.

5.4 Conclusion

The ExB layer models were assessed using an analytical solution and experimental results. The suggested ExB layer model provides exact agreement with theory and has good agreement with the measured data. Both model and measurements show a significant density reduction in the ExB layer and the maximum density reduction occurs near the cathode. Furthermore, the results show the applied ExB layer does

not affect the entire flow.

The suggested one-dimensional and two-dimensional ExB layer models show good agreement under a high magnetic field. This means that the two-dimensional effects of the magnetic and electric fields become less important under the high magnetic field condition and the z-direction component becomes dominant. The rate of change of plasma density becomes smaller in the high magnetic field condition. All of the ExB layer models agree in the case of a high magnetic field, above 0.2 T, which gives the optimized plasma density reduction. The electric field also shows phenomena similar to that of the magnetic field. The models predict a similar plasma density reduction at the high potential drop, above -500 V.

The good agreements demonstrated that the ExB layer models can accurately predict the reduced plasma density in the ExB layer. The numerical and experimental results show that the applied ExB layer can significantly manipulate the plasma density for communication. Therefore, the application of electric and magnetic fields should allow radio communication through a hypersonic plasma layer during re-entry.

CHAPTER VI

Simulation of an Electromagnetic Mitigation Scheme in Hypersonic Flow

The ExB layer model was presented in Chapters III and IV for a single species plasma. The suggested model demonstrated that an applied ExB layer can significantly reduce the plasma density under the experimental condition using an argon plasma. However, the single species plasma model cannot be easily applied to simulate the re-entry hypersonic flight condition, thus requiring the consideration of a multi-chemical species model: N, O, N_2, O_2, NO, N^+, O^+, N_2^+, O_2^+, NO^+, and e^-. This chapter focuses mainly on the simulation of the ExB layer in a hypersonic flow, to assess the mitigation scheme in a realistic operating condition. For this simulation, the OREX (Orbital Re-entry Experiment Vehicle) geometry is used because it is a typical blunt body reentry vehicle. In this case, the governing equations are composed of two parts: the flow field and the electric field. The flow field equations are the Navier-Stokes equations and are solved numerically using a hypersonic CFD code, LeMANS (The Michigan Aerothermal Navier-Stokes Solver), developed at the University of Michigan Nonequilibrium Gas and Plasma Dynamics Laboratory (NGPDL). For the electric field equation, this chapter describes a finite element method (FEM) for solving the Poisson equation. In this chapter, the effectiveness of the ExB

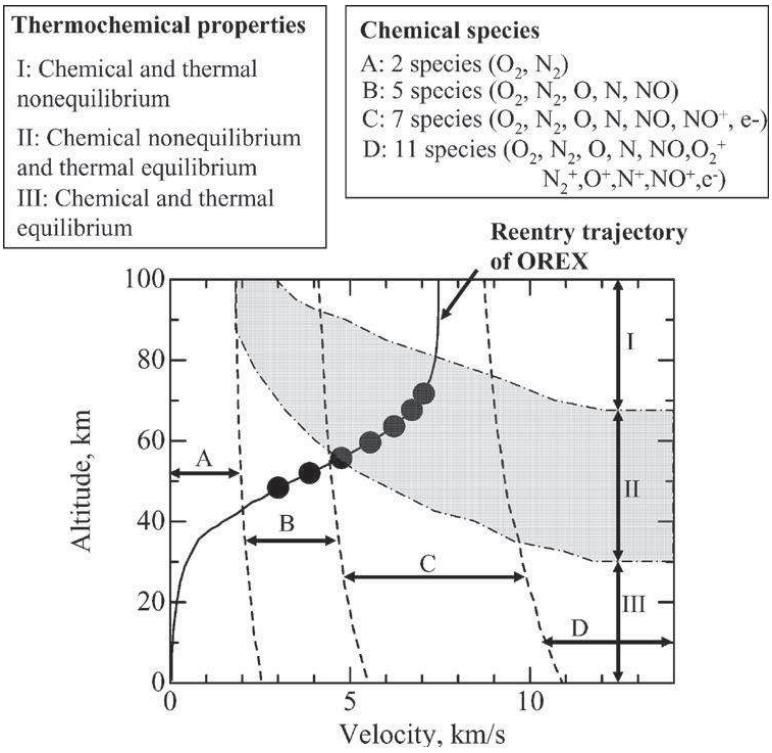

Figure 6.1: Thermochemical properties of gas in the shock layer in reentry flight for OREX [taken from [94]]

layer is expressed in terms of the radio wave attenuation.

6.1 Governing Equations

In the previous chapters, the ExB layer mitigation scheme was demonstrated under an experimental condition, in which the generation of the plasma layer was not considered.

Figure 6.1 shows the thermochemical properties of the OREX re-entry flight. As can be seen, the re-entry flow requires a multi-chemical species model [94]. In this section, the following eleven species air chemistry model is considered: N, O, N_2, O_2, NO, N^+, O^+, N_2^+, O_2^+, NO^+, and e^-.

The governing equations for the ExB layer with the eleven chemical species are composed mainly of two parts, which are the flow field and the electric field. The

flow field equations describe a hypersonic flow with a Lorentz force, which is provided by the applied ExB layer. In this case, the flow field equations require the current, electric field, and magnetic field. These are provided by the electric field equation which comes from Maxwell's equations and Faraday's law.

6.1.1 Flow Field Equations

The flow field equations describe a hypersonic flow with the ExB layer and they are similar to the Navier-Stokes equations. The hypersonic condition causes many physical phenomena in the flow field including chemical non-equilibrium, vibrational and electronic excitation, thermal non-equilibrium and ionization [15]. This section considers chemical non-equilibrium using a finite rate chemistry model and assumes a thermal equilibrium consistent with the thermochemical properties of the OREX re-entry as shown in Figure 6.1 [95]. Therefore, the hypersonic flow is described by the continuum framework, which means the Knudsen number, Kn, is much smaller than unity and the particles are big enough to see their environment as a continuum, by means of a chemical non-equilibrium one-temperature gas model.

The governing equations for the flow field description are the mass conservation equations of the chemical species, the momentum conservation equations and the total energy conservation equation. In order to simplify the flow field equations, the magnetic Reynolds number is assumed to be much smaller than unity because the typical magnetic Reynolds number is the order of 10^{-3} in a weakly ionized gas [59]. For a low magnetic Reynolds number assumption, the flow field equations are obtained by coupling the Navier-Stokes equation with the Lorentz force, $\vec{J} \times \vec{B}$, and the energy interaction, $\vec{E} \cdot \vec{J}$, terms [96].

The governing equations of the flow field with the ExB layer can be expressed in

the following form:

$$\frac{\partial \mathbf{Q}}{\partial t} + \nabla \cdot \mathbf{F} - \nabla \cdot \mathbf{F}_v = \mathbf{S}_{cv} + \mathbf{S}_{MHD} \tag{6.1}$$

where $\mathbf{Q}$ is the vector of conserved variables, $\mathbf{F}$ is the flux vector, $\mathbf{F}_v$ is the viscous flux vector, $\mathbf{S}_{cv}$ is a thermochemical source term, and $\mathbf{S}_{MHD}$ is a source term related to the electromagnetic force. For a three-dimensional system, the vector of conserved variables, $\mathbf{Q}$, is given by

$$\mathbf{Q} = \left\{ \begin{array}{c} \rho_1 \\ \rho_2 \\ \vdots \\ \rho_{ns} \\ \rho u \\ \rho v \\ \rho w \\ E_t \end{array} \right\} \tag{6.2}$$

where ρ_i is the density of species i, $u, v,$ and w are flow velocities, and E_t is the total energy.

The inviscid and diffusive flux vector components in the x direction are given by

$$\mathbf{F}_x = \left\{ \begin{array}{c} \rho_1 u \\ \rho_2 u \\ \vdots \\ \rho_{ns} u \\ \rho u^2 + p \\ \rho u v \\ \rho u w \\ (E+p)\, u \end{array} \right\} \tag{6.3}$$

and

$$\mathbf{F}_{v,x} = \left\{ \begin{array}{c} -J_{x,1} \\ -J_{x,2} \\ \vdots \\ -J_{x,ns} \\ \tau_{xx} \\ \tau_{xy} \\ \tau_{xz} \\ \tau_{xx} u + \tau_{xy} v + \tau_{xz} w - q_x - \sum_{\text{all species}} (J_{x,s} h_s) \end{array} \right\} \tag{6.4}$$

where, ρ is the mixture mass density which is defined as the summation of species mass densities, $\rho = \sum_{\text{all species}} \rho_s$, p is the pressure, $\vec{\mathbf{J}}_s$ is the species diffusion flux, $\tau_{i,j}$ are the viscous stress components, $\vec{\mathbf{q}}$ is the heat flux, and h_s is the species enthalpy. The diffusion fluxes are modeled using a modified Ficks law to enforce that the sum

of the diffusion fluxes is zero [15, 97]

$$\vec{\mathbf{J}}_{s,\text{modified}} = \vec{\mathbf{J}}_s - C_s \sum_{r \neq e} \vec{\mathbf{J}}_s \tag{6.5}$$

with

$$\vec{\mathbf{J}}_s = -\rho D_s \nabla C_s \tag{6.6}$$

where D_s is the species diffusion coefficient and C_s is the species mass fraction. However, for the electrons, Eq. 6.5 gives a small value for the electron diffusion because the mass of electrons is relatively small compared to that of atoms and molecules as shown in Table 6.1. In this case, the diffusion flux of electrons can be calculated assuming ambipolar diffusion which guarantees the charge neutrality of the flow field by [15]

$$\vec{\mathbf{J}}_e = m_e \sum_{s \neq e} \frac{\vec{\mathbf{J}}_{s,\text{modified}} c_s}{m_s} \tag{6.7}$$

where m_e is the electron mass, 9.109×10^{-31} kg, c_s is the electrical charge of the species, and m_s is the species molecular mass. The viscous stress tensor, $\tilde{\tau}$ can be expressed for a Newtonian viscous fluid as follows [98]:

$$\tau_{i,j} = \mu \left(\frac{\partial u_i}{\partial x_j} + \frac{\partial u_j}{\partial x_i} \right) + \delta_{i,j} \lambda \nabla \vec{\mathbf{V}} \tag{6.8}$$

where μ is the coefficient of viscosity and λ is the coefficient of bulk viscosity. The bulk viscosity coefficient can be obtained using Stokes' hypothesis [98, 15].

$$\lambda + \frac{2}{3}\mu = 0 \tag{6.9}$$

The detailed expression for the diffusion and viscosity coefficients can be found in [15].

The thermochemical source term,$\mathbf{S}_{vc}$, is given by

$$\mathbf{S}_{cv} = \begin{Bmatrix} \dot{\omega_1} \\ \dot{\omega_2} \\ \vdots \\ \dot{\omega_{ns}} \\ 0 \\ 0 \\ 0 \\ 0 \end{Bmatrix} \tag{6.10}$$

where $\dot{\omega_s}$ is the species mass production rates of chemical reactions, and can be expressed as [94]

$$\dot{\omega_s} = m_s \sum_{r}^{\text{all reaction}} (\beta_{s,r} - \alpha_{s,r}) (R_{f,r} - R_{b,r}) \tag{6.11}$$

where α and β are the stoichiometric coefficients of the reactions, and $R_{f,r}$ and $R_{b,r}$ are the forward and backward reaction rates, respectively. The forward reaction rate, $R_{f,r}$, is defined by

$$R_{f,r} = k_{f,r} \prod_{s}^{\text{all species}} \left(\frac{\rho_s}{m_s}\right)^{\alpha_{s,r}} \tag{6.12}$$

where $k_{f,r}$ is the forward reaction coefficient. The backward reaction rate, $R_{b,r}$, is defined by

$$R_{b,r} = k_{b,r} \prod_{s}^{\text{all species}} \left(\frac{\rho_s}{m_s}\right)^{\beta_{s,r}} \tag{6.13}$$

where $k_{b,r}$ is the backward reaction coefficient. The details of the forward and backward reaction coefficients can be found in [15] and [99].

Table 6.1: A relative mass of electron by comparison with atoms and molecules

Atoms / Molecules	Relative mass of electron, $\frac{m_e}{m_i}$
O	3.4290×10^{-5}
O_2	1.7145×10^{-5}
N	3.9168×10^{-5}
N_2	1.9584×10^{-5}
NO	1.8284×10^{-5}

The source term for the electromagnetic force can be expressed in the following form,

$$\mathbf{S}_{MHD} = \begin{Bmatrix} 0 \\ 0 \\ \vdots \\ 0 \\ \left(\vec{\mathbf{j}} \times \vec{\mathbf{B}}\right)_x \\ \left(\vec{\mathbf{j}} \times \vec{\mathbf{B}}\right)_y \\ \left(\vec{\mathbf{j}} \times \vec{\mathbf{B}}\right)_z \\ \vec{\mathbf{E}} \cdot \vec{\mathbf{j}} \end{Bmatrix} \tag{6.14}$$

where $\vec{\mathbf{j}}$ is the current density vector, $\vec{\mathbf{B}}$ is the magnetic field vector, and $\vec{\mathbf{E}}$ is the electric field vector.

The flow field equations, Eq. 6.1, are solved by LeMANS, which is a computational fluid dynamics code developed at the University of Michigan Department of Aerospace Engineering. LeMANS is a chemically reacting, parallelized, implicit Navier-Stokes CFD code using a modified Steger-Warming Flux Vector Splitting

scheme to calculate inviscid fluxes between mesh volumes. Complete details of the code can be found elsewhere [15]. To include the electromagnetic effect, additional source terms of the electromagnetic effect, $\mathbf{S}_{MHD}$, are included in LeMANS.

6.1.2 Electric Field Equations

The equations that describe the flow field have three electrical quantities, $\vec{\mathbf{j}}$, $\vec{\mathbf{B}}$, and $\vec{\mathbf{E}}$. To obtain these quantities, it is necessary to use an electric field equation.

First, the magnetic field $\vec{\mathbf{B}}$, is obtained from the imposed magnetic field. In the electric field equation, the magnetic field Reynolds number, R_M, is a good parameter for characterizing the equation because it is a measure of the coupling between the motion of the magnetic field line and the motion of the conducting fluid [43]. When the magnetic Reynolds number is much smaller than unity, the magnetic field is not greatly affected by the fluid motion. This means that the magnetic field induced by current is negligible compared with the imposed magnetic field. In this dissertation, the magnetic Reynolds number of the hypersonic flow field is assumed very small. This assumption is quite reasonable because in a Newtonian limit, the magnetic Reynolds number becomes very small in hypersonic flow, usually on the order of 10^{-3} [100, 101] for many aerospace applications [102]. The magnetic Reynolds number is smaller than 10^{-3} when an ionization rate is less than 1 % [59]. In OREX case at 79.9 km altitude condition, the maximum ionization rate is 0.07 % Therefore, the magnetic field, $\vec{\mathbf{B}}$, is a known variable from the imposed magnetic field. The configuration of the imposed magnetic field is the same as that given in Chapter IV.

The generalized Ohm's law is employed to obtain the current density [103]:

$$\vec{\mathbf{j}} = \sigma \left[\left(\vec{\mathbf{E}} + \vec{\mathbf{U}} \times \vec{\mathbf{B}} \right) - \beta \frac{\vec{\mathbf{j}} \times \vec{\mathbf{B}}}{B} + \alpha \left(\vec{\mathbf{j}} \times \vec{\mathbf{B}} \times \vec{\mathbf{B}} \right) \right] \tag{6.15}$$

where σ is the electrical conductivity, β is the Hall parameter, and α is an ion-slip

coefficient. The detailed derivation of the generalized Ohm's law can be found in [103].

The generalized Ohm's law, Eq.6.15 can be simplified with the conductivity tensor as follows:

$$\vec{\mathbf{j}} = \tilde{\sigma} \cdot \left(\vec{\mathbf{E}} + \vec{\mathbf{U}} \times \vec{\mathbf{B}} \right) \tag{6.16}$$

where $\tilde{\sigma}$ is a conductivity tensor given by

$$\tilde{\sigma} = \frac{\sigma}{D} \begin{bmatrix} \sigma_{11} & \sigma_{12} & \sigma_{13} \\ \sigma_{21} & \sigma_{22} & \sigma_{23} \\ \sigma_{31} & \sigma_{32} & \sigma_{33} \end{bmatrix} \tag{6.17}$$

where,

$$D = \left(1 + \alpha\sigma\vec{\mathbf{B}}^2 \right)^2 + \left(\beta\sigma\vec{\mathbf{B}} \right)^2 \tag{6.18}$$

and the coefficients, σ_{ij}, can be expressed as:

$$\sigma_{11} = \left(1 + \alpha\sigma\vec{\mathbf{B}}^2 \right) \left(1 + \alpha\sigma B_x^2 \right) + \beta^2\sigma^2 B_x^2 \tag{6.19}$$

$$\sigma_{12} = \sigma \left[\alpha B_x B_y \left(1 + \alpha\sigma\vec{\mathbf{B}}^2 \right) - \beta \left(B_z - \beta\sigma B_x B_y \right) \right] \tag{6.20}$$

$$\sigma_{13} = \sigma \left[\alpha B_x B_z \left(1 + \alpha\sigma\vec{\mathbf{B}}^2 \right) + \beta \left(B_y + \beta\sigma B_x B_z \right) \right] \tag{6.21}$$

$$\sigma_{21} = \sigma \left[\alpha B_x B_y \left(1 + \alpha\sigma\vec{\mathbf{B}}^2 \right) + \beta \left(B_z + \beta\sigma B_x B_y \right) \right] \tag{6.22}$$

$$\sigma_{22} = \left(1 + \alpha\sigma\vec{\mathbf{B}}^2 \right) \left(1 + \alpha\sigma B_y^2 \right) + \beta^2\sigma^2 B_y^2 \tag{6.23}$$

$$\sigma_{23} = \sigma \left[\alpha B_y B_z \left(1 + \alpha\sigma\vec{\mathbf{B}}^2 \right) - \beta \left(B_x - \beta\sigma B_y B_z \right) \right] \tag{6.24}$$

$$\sigma_{31} = \sigma \left[\alpha B_x B_z \left(1 + \alpha\sigma\vec{\mathbf{B}}^2 \right) - \beta \left(B_y - \beta\sigma B_x B_z \right) \right] \tag{6.25}$$

$$\sigma_{32} = \sigma \left[\alpha B_y B_z \left(1 + \alpha\sigma\vec{\mathbf{B}}^2 \right) + \beta \left(B_x + \beta\sigma B_y B_z \right) \right] \tag{6.26}$$

$$\sigma_{33} = \left(1 + \alpha\sigma\vec{\mathbf{B}}^2 \right) \left(1 + \alpha\sigma B_z^2 \right) + \beta^2\sigma^2 B_z^2 \tag{6.27}$$

The detailed derivation of the electrical conductivity tensor, σ_{ij}, is presented in Appendix C.

The electric field, $\vec{\mathbf{E}}$, can be obtained from the current density conservation with the definition of the electric field.

$$\nabla \cdot \vec{\mathbf{j}} = 0 \tag{6.28}$$

Now, using the generalized Ohm's law:

$$\nabla \cdot \left[\tilde{\sigma} \cdot \left(\vec{\mathbf{E}} + \vec{\mathbf{U}} \times \vec{\mathbf{B}} \right) \right] = 0 \tag{6.29}$$

Equation 6.29 becomes a scalar equation by using the definition of electric field, $\vec{\mathbf{E}} = -\nabla\phi$, as follows:

$$\nabla \cdot (\tilde{\sigma} \cdot \nabla\phi) = \nabla \cdot \left(\vec{\mathbf{U}} \times \vec{\mathbf{B}} \right) \tag{6.30}$$

For a hypersonic re-entry flow, Eq. 6.30 can be simplified. In Eqs. 6.15 and 6.16, the Hall and ion-slip effect are considered. The estimated electron Hall parameter, defined as the product of the electron cyclotron frequency and the mean collision free time with the other chemical species, is of the order of 10^{-1} [104]. Therefore, in the plasma region produced behind the shock, the ion slip effect does not have a considerable influence on the electric current [94, 105]. Since the Hall effect does not have negative influences on the usefulness of the MHD flow control, the Hall effect could be negligible [105]. Therefore the conductivity tensor becomes a scalar and the equation for the electric field is obtained as follows:

$$\nabla \cdot (\sigma \nabla\phi) = \nabla \cdot \left[\sigma \left(\vec{\mathbf{U}} \times \vec{\mathbf{B}} \right) \right] \tag{6.31}$$

Equation 6.31 is solved by using a finite element method (FEM) to give the potential distribution [105, 106].

6.2 OREX

The OREX (Orbital Re-entry Experiment Vehicle) geometry is considered in order to simulate a hypersonic flow of a re-entry vehicle with an ExB layer to manipulate the plasma. OREX, which was launched from the Tanegashima Space Center of Japan in 1994 in order to conduct reentry experiments, used the C-band for the tracking signal, and S-band and X-band for the data telemetry [107]. OREX was especially designed to acquire the following data related to atmospheric re-entry:

1. Aerodynamic and aerodynamic heating data during re-entry
2. Heat-resistant structural data during re-entry
3. Communications blackout data during re-entry
4. GPS navigation data during re-entry and in orbit

6.2.1 OREX Geometry

Figure 6.2 shows the geometry of OREX which has an axisymmetric shape. OREX is a typical blunt body reentry vehicle with a nearly zero angle of attack in the re-entry experiment. The forebody shape of OREX is composed of a spherical nose with a 1.35 m radius, a cone, and a circular shoulder.

Figure 6.3 shows OREX with a proposed configuration of the electrodes and electromagnet that provide the ExB layer for the blackout mitigation scheme. The ExB layer is applied to OREX to manipulate the plasma layer. As can be seen, the electrodes are located on the vehicle surface and they are separated by 10 cm. The electromagnet is located inside of the vehicle. The applied magnetic field data are based on measured data, and is similar to the magnetic field presented in Chapter IV.

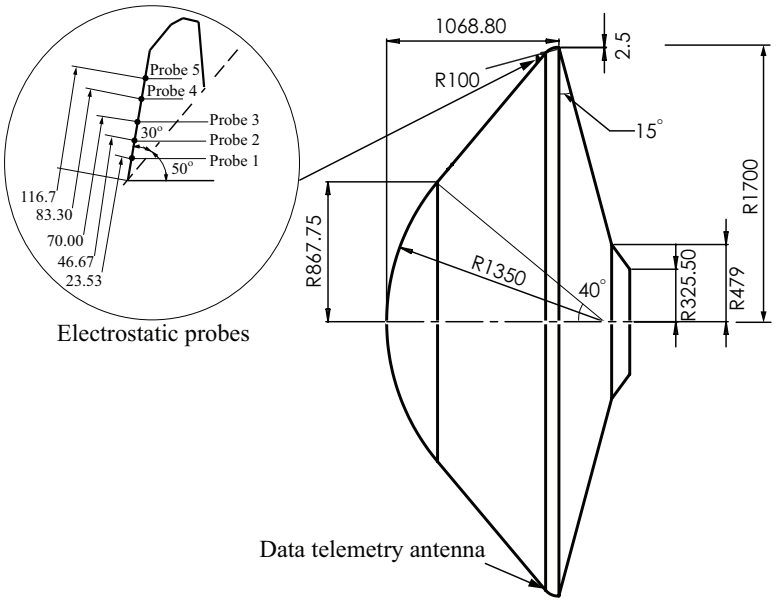

Figure 6.2: Geometry of OREX where the units are mm

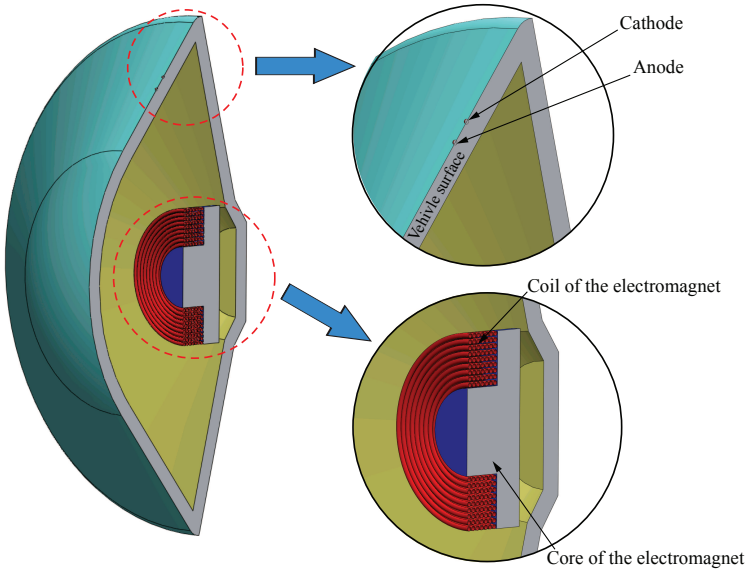

Figure 6.3: Configuration of OREX with the electrode and electromagnet which provide the ExB layer as the blackout mitigation scheme.

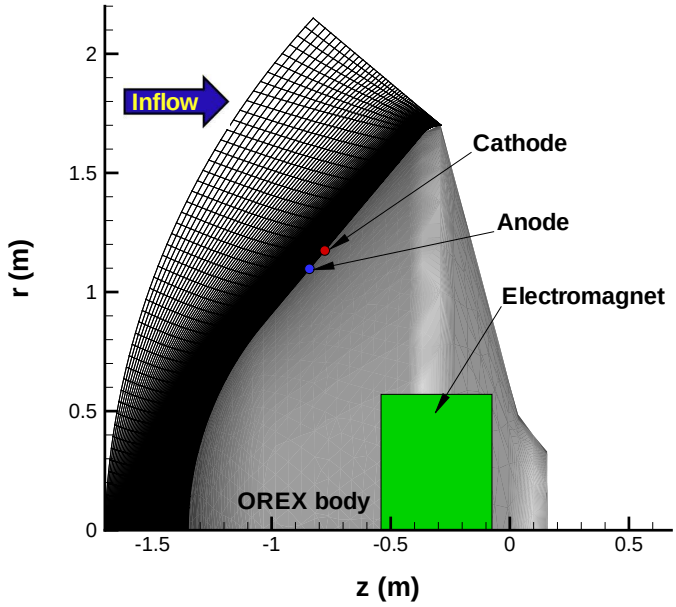

Figure 6.4: Mesh for the two-dimensional OREX simulation with the ExB layer with a schematics of the ExB layer configuration

Figure 6.4 shows the simulation domain with a simplified OREX geometry. The simplified configuration is composed of a spherical nose with a 1.35 m radius and a cone. Figure 6.4 also shows the location of the two 5 mm radius electrodes and the electromagnet. The electromagnet is located at the center of the vehicle because of its size. In order to provide 0.5 T, a typical size of electromagnet is about 60 cm in diameter [54].

6.2.2 Boundary Conditions

Table 6.2 shows the inflow conditions and wall temperature of OREX at several altitudes [4]. The chemical composition of free stream air is assumed to be 79% N_2 and 21% O_2 in terms of mole fraction at all altitudes. Since OREX experienced a radio blackout at approximately 80 km [108], this study chose the 79.9 km inflow condition of OREX for the simulation.

Table 6.2: Freestream conditions and wall temperature of OREX for several altitude conditions [4]

Altitude H (km)	Velocity U_∞ (m/s)	Temperature T_∞ (K)	Pressure P_∞ (Pa)	Wall Temperature T_w (K)
92.82	7454.1	188.70	0.163	492
84.01	7415.9	188.90	0.594	587
79.90	7360.2	198.64	1.052	690
71.73	7049.2	214.98	4.023	1078
67.66	6720.3	225.99	7.892	1251
63.60	6223.4	237.14	14.02	1413
59.60	5561.6	248.12	23.60	1519
55.74	4759.1	258.74	39.48	1571
51.99	3873.4	268.20	63.48	1557
48.40	3000.0	270.65	98.50	1501

The boundary condition of the cathode is straightforward because the potential there is assumed to be an externally given value. The anode is grounded on the vehicle so it has the same potential as the surface. On the surface of OREX, a zero potential is assumed. The inflow and outflow boundary condition use a zero potential variation across the boundary.

Figure 6.5 shows the magnetic field configuration. In this study, the electromagnet is assumed to be located at the center of OREX when considering the size of the actual electromagnet which has an approximately 0.5 m radius for the core. As can be seen, the maximum magnetic field strength occurs at the front of the vehicle.

6.3 Simulation Results

Figure 6.6 shows the electron number density distribution for OREX at 79.9 km. As can be seen, the plasma number density is high enough to cause the radio blackout of L-band and UHF communication. The critical densities for L-band and S-band communications are $3.53 \times 10^{16} m^{-3}$ and $6.54 \times 10^{16} m^{-3}$, respectively. This result is consistent with the fact that the blackout of OREX actually started at 80 km and ended at 50 km [108]. Figure 6.7 shows the comparison with the OREX measurement of electron number densities by an electrostatic probe mounted on the conical flank before the probe shoulder [4] and the simulation result of LeMANS and indicates that LeMANS provides a reasonable result for the reentry simulation of OREX.

Figure 6.8 shows the plasma number density distribution with the ExB layer mitigation scheme. In this case, the 0.1 T magnetic field with -800 V potential drop is applied. As can be seen, the applied ExB layer reduces the electron number density and creates a window for communication. The manipulated plasma number density is low enough for the S-band communication which was used for the data

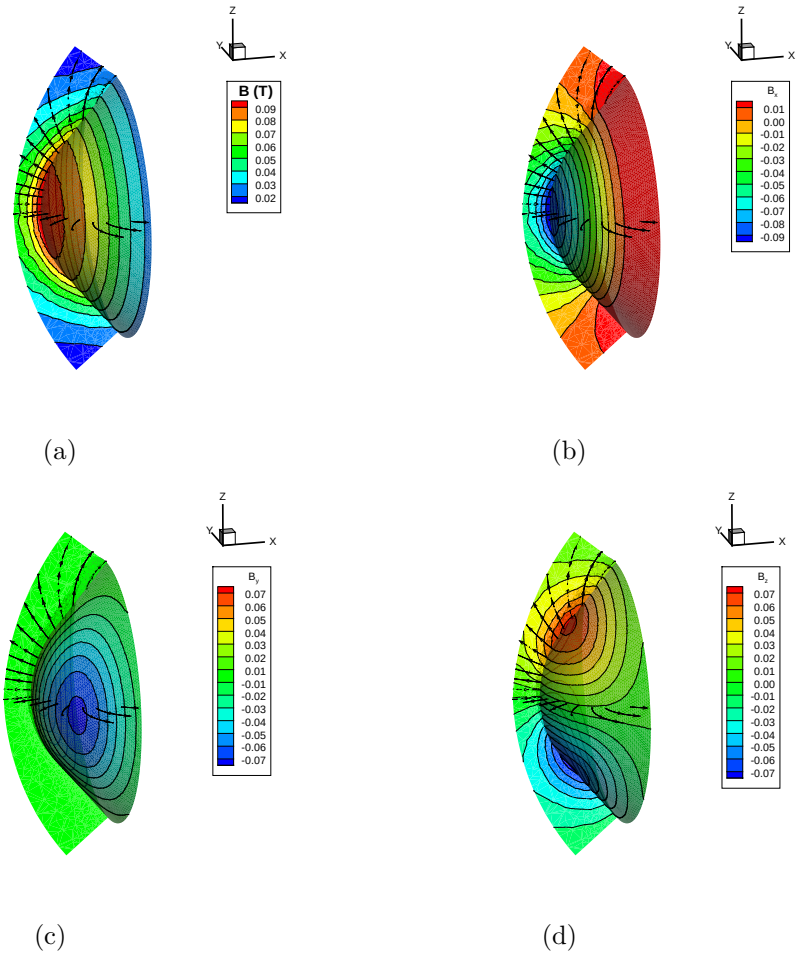

Figure 6.5: Configuration of the applied magnetic field: (a) Magnetic field strength, B, in T with the magnetic field lines. (b) x-direction magnetic field, B_x, in T with the magnetic field lines. (c) y-direction magnetic field, B_y, in T with the magnetic field lines. (d) z-direction magnetic field, B_z, in T with the magnetic field lines.

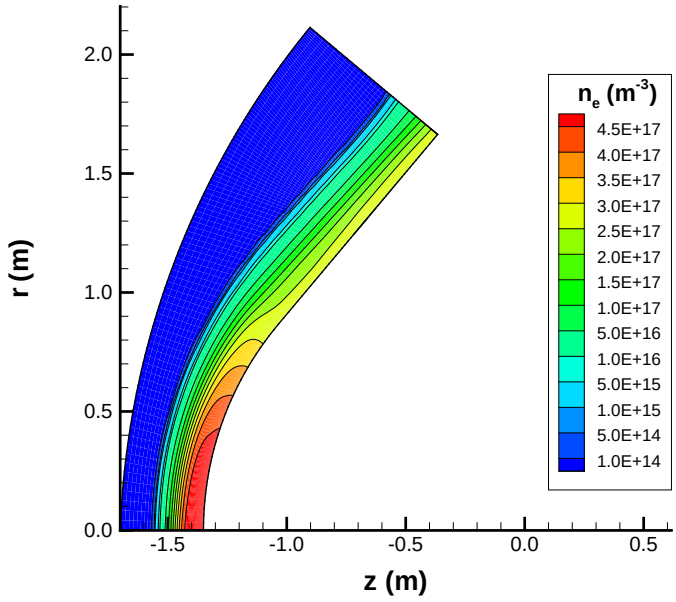

Figure 6.6: Distribution of the electron number density without the ExB layer mitigation scheme.

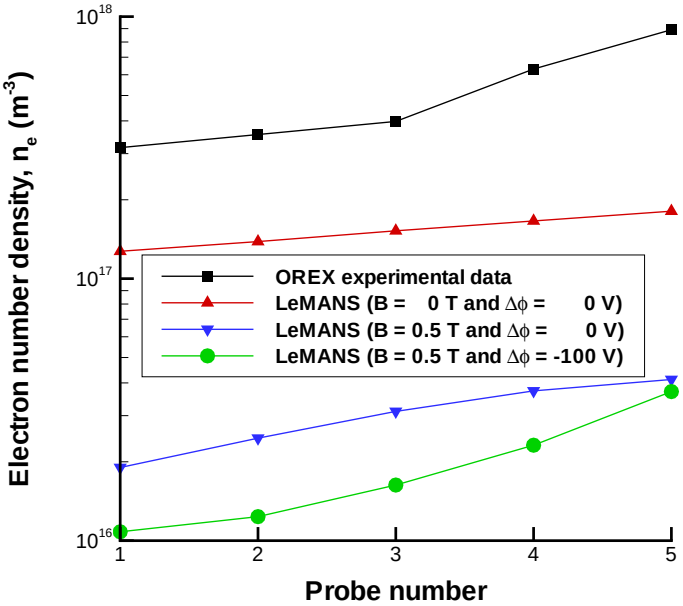

Figure 6.7: The comparison of the OREX measurement and the simulation result of LEMANS for electron number density.

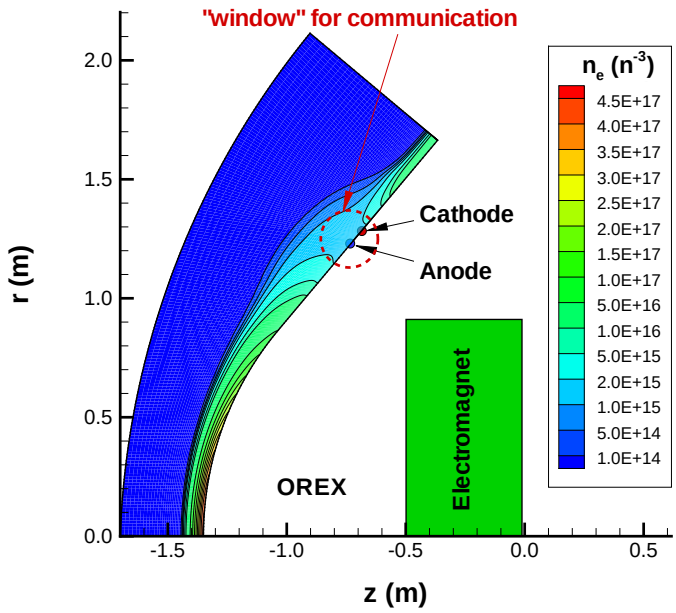

Figure 6.8: Distribution of the electron number density with the ExB layer mitigation scheme. The applied magnetic field is 0.1 T with -800 V a potential drop.

telemetry of OREX. Figure 6.8 also shows that the plasma density returns to its original density past the applied ExB layer. This indicates that the applied ExB layer can manipulate a plasma layer in order to solve the communication blackout problem without disturbing the flow field.

Figure 6.9 shows the applied magnetic field configuration. The electromagnet is located at the center of OREX and provides the maximum magnetic field at the front of the vehicle. The location of the electromagnet is quite realistic considering the size of the electromagnet, which has a 0.5 m core radius.

Figure 6.10 shows the potential distribution of the ExB layer. As can be seen, the applied potential is mainly focused near the cathode. This means that the applied ExB layer can reduce plasma density only near the cathode.

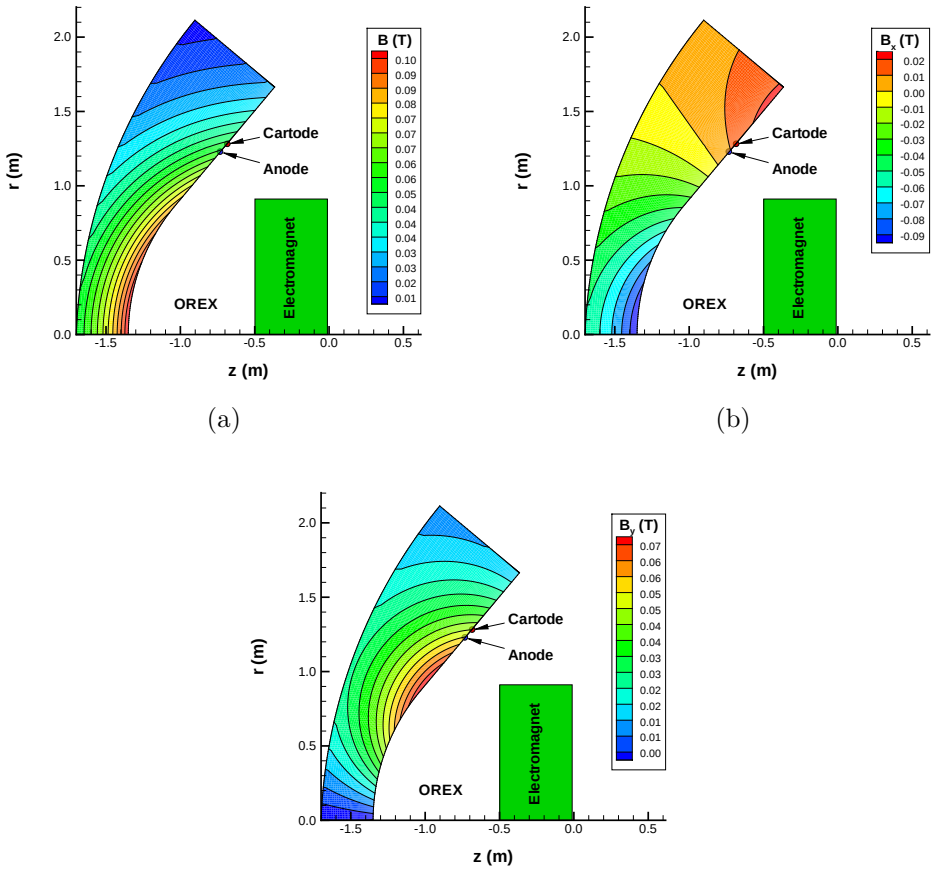

Figure 6.9: Configuration of the applied magnetic field: (a) Magnetic field strength, B, in T with the magnetic field lines. (b) x-direction magnetic field, B_x, in T with the magnetic field lines. (c) y-direction magnetic field, B_y, in T with the magnetic field lines.

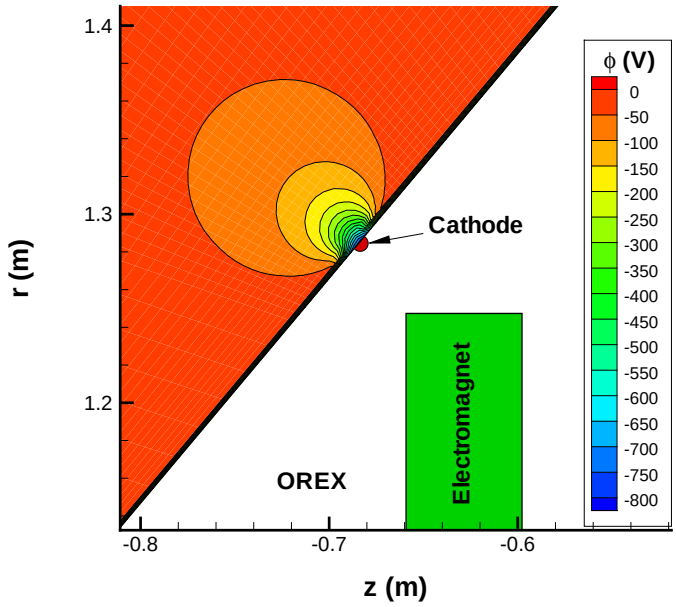

Figure 6.10: Distribution of potential: the anode is grounded at 0 V and the cathode is at -800 V

6.4 Discussion

Figure 6.11 shows the plasma density distribution for OREX near the ExB layer as a function of applied magnetic-field strength and potential drop. As can be seen, the plasma density reduction increases with magnetic field strength and the highest plasma density reduction occurs when both the electric field and magnetic field are applied. This agrees with the previous results for the ExB layer which were presented in Chapters III and IV. Figure 6.11 also shows that the plasma density reduction improves significantly when the electric field is applied. This means that the ExB layer mitigation scheme gives better performance in the manipulation of the plasma layer than the magnetic window method which uses only a magnet.

Figure 6.11 reveals a plasma density reduction even when no voltage is applied to the cathode. The density reduction in this case occurs because of the magnetic

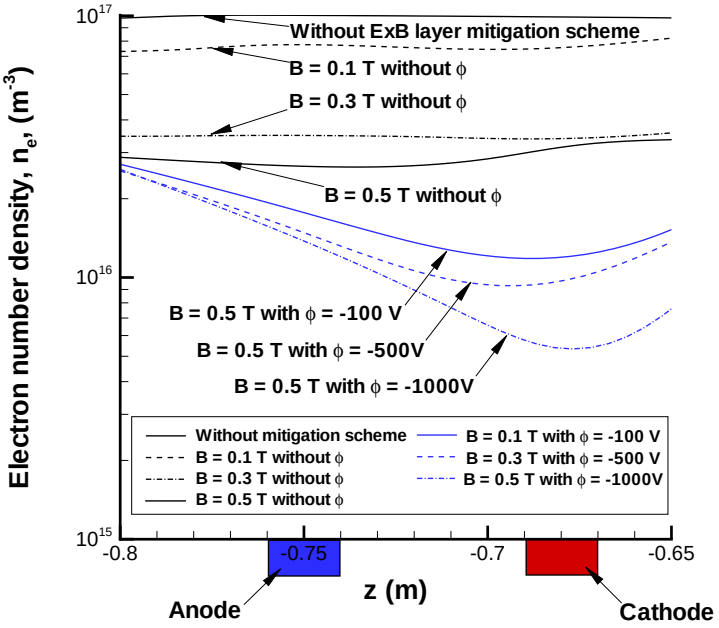

Figure 6.11: The electron number density distribution near the surface of OREX for several operational conditions of an ExB mitigation scheme.

field, which can generate a current density in the absence of an electric field. The generated current density is smaller than that in the electric field case, but it can give a Lorentz force for the plasma acceleration. When the electric field is applied, it gives a higher current density. In this case, the magnetic field helps to maintain a strong electric field. Therefore the electric field improves the plasma density reduction in the hypersonic plasma layer.

Figure 6.12 shows the maximum plasma density reduction in terms of applied magnetic-field strength and potential drop. The minimum required plasma density reduction is tabulated in Table 6.3. At the 79.9 km reentry condition, OREX has a radio blackout for VHF, UHF, L- band, GPS frequency, and S-band. In order to solve radio blackout for the S-band, which is used for the data telemetry of OREX, the plasma density reduction should be stronger than 0.6. This density reduction can be

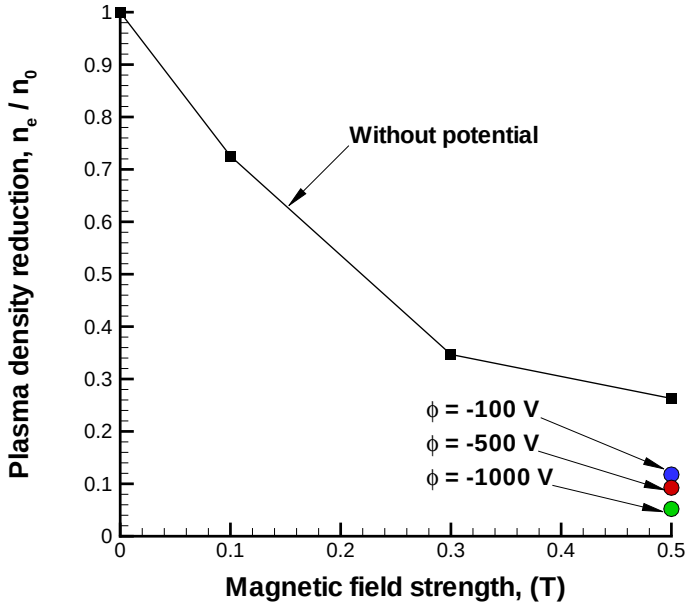

Figure 6.12: The maximum plasma density reduction by an ExB layer in a hypersonic flight condition

obtained with a 0.3 T magnetic field in the ExB layer mitigation scheme. However, this configuration of the ExB layer still provides a weak plasma density reduction for the L-band and GPS frequency. Even a 0.5 T magnetic field can not solve a blackout for the L-band. However, the applied ExB layer with 0.5 T and -1000 V potential drop gives a plasma density reduction of about 0.05. In this case, the plasma density reduction satisfies the minimum required value for L-band and GPS communication. For the GPS frequency, signal attenuation becomes approximately 10 dB with the ExB layer mitigation scheme. This demonstrates the possibility of an ExB layer mitigation scheme to solve radio blackout in the hypersonic flight condition.

Table 6.3: The required plasma density reduction for OREX at 79.9 km reentry condition

VHF 300 MHz	UHF 3000 MHz	L band 2 GHz	GPS 1.4 GHz	S band 4 GHz	X band 12 GHz	K_u band 18 GHz
0.004	0.3497	0.1486	0.0728	0.5945	No blackout	No blackout

6.5 Conclusion

This chapter discussed the simulation of the ExB layer mitigation scheme in a hypersonic flow for the OREX reentry vehicle. Since OREX is representative of a typical blunt body reentry vehicle, the hypersonic flow simulation with the mitigation scheme is useful for demonstrating the ExB layer mitigation scheme in a realistic operating condition.

The simulation results for OREX show that the applied ExB layer provides a reduced plasma density near the cathode in a hypersonic flow at a 79.9 km reentry condition. As expected, the plasma density reduction depends on the strength of the electric field and magnetic field. The maximum plasma density reduction occurs with a combination of the electric and magnetic fields. This fact indicates that to communicate through the plasma layer, the ExB layer mitigation scheme is a more effective solution for radio blackout than the magnetic window method which, though promising, is impractical [6].

The configuration of the ExB layer can be determined in relation to the radio wave band for communication. As the flight data show [108], OREX experienced radio blackout at 80 km altitude. The simulation results at 79.9 km show that the plasma density of OREX is high enough to cause radio blackout for UHF, the L-band, and the S-band. For the S-band communication blackout, the ExB layer

with a 0.3 T magnetic field provides a sufficient plasma density reduction to enable communication through the plasma layer. The ExB layer with 0.5 T and - 800 V potential shows the possibility for communication through the plasma layer for the L band and GPS frequency.

CHAPTER VII

Conclusion

This chapter provides a summary and review of the thesis and identifies original contributions of this study. Potential future work is outlined in the last section of this chapter.

7.1 Summary and Review

This dissertation presented mitigation schemes for communication blackout during hypersonic/reentry flight and analyzed them using numerical models. The dissertation provided two possible methods to manipulate the plasma layer: the electrostatic sheath and the electromagnetic layer, i.e. the ExB layer.

The electrostatic sheath method was described and demonstrated as a mitigation scheme in Chapter II. This method uses a unique property whereby electrons are depleted in the electrostatic sheath. To be a potential mitigation scheme, the size of the sheath should be maximized so that it is larger than the antenna. To maximize the electrostatic sheath, this dissertation suggested the use of two-dimensional shaped electrodes and evaluated those as a mitigation scheme for radio blackout.

The electromagnetic manipulation scheme was presented in Chapters III and IV. To simulate the electromagnetic, ExB layer, one-dimensional and two-dimensional

models were suggested. The effects of altitude, magnetic field, and current density were studied and indicated a possible ExB layer configuration which solves the radio blackout problem, as described in Chapter III. Since the one-dimensional ExB layer model cannot determine the size of the communications window which is created by the manipulated plasma density, a two-dimensional ExB layer model was provided in Chapter IV. The simulation results showed that the applied ExB layer can effectively reduce the plasma number density outwards to approximately 2cm from the surface. The overall efficiency of the electromagnetic scheme for reentry telemetry was evaluated in terms of the magnetic and electric fields and provided an optimal configuration of the ExB layer, as given in Chapter IV.

In Chapter V, the simulation results were assessed through comparison with experimental data and with analytical solutions. The suggested ExB layer model provided exact agreement with theory and offered good agreement with the experimental results. The consistency of the ExB layer model was also demonstrated in a comparison of the one-dimensional ExB layer model and the two-dimensional model in Chapter V. The suggested one-dimensional and two-dimensional ExB layer models showed good agreement under high magnetic and high electric fields. As a result of this good agreement, the ExB layer models demonstrated that they can accurately predict the reduced plasma density in the ExB layer.

The ExB layer mitigation scheme was simulated in a hypersonic flow for the OREX reentry vehicle and evaluated for solving blackout in Chapter VI. The simulation results at 79.9 km revealed that the plasma density of OREX is high enough to cause radio blackout for the UHF, the L-band, and the S-band. The results indicated that the suggested ExB layer mitigation scheme is a more realistic solution for radio blackout than the magnetic window method.

7.2 Contributions

This dissertation mainly contributes to the development of a reliable and acceptable communication method for radio blackout during hypersonic/reentry flight. Outlined below is a numbered list of major original contributions, made by the present study.

1. **The electrostatic sheath was investigated as a mitigation scheme and two-dimensional shaped electrodes were suggested to offer the possibility for communication through the plasma layer. (Chapter II)** The electron depleted region of the two dimensional electrode system was simulated by using a two-dimensional fluid sheath model. The simulation result demonstrated that the two-dimensional shaped electrodes create a thicker sheath than is possible with a plate electrode under the same voltage condition. The electrostatic mitigation scheme has unique advantages compared with other mitigation schemes. Other mitigation schemes based on plasma manipulation present difficulties in solving a low frequency radio blackout problem such as voice communication because it is difficult to completely deplete electrons. However, the sheath region of the electrostatic mitigation scheme has almost zero electrons thus allowing low frequency communication such as VHF and UHF. Since the sheath thickness is also affected by the plasma density, reducing the plasma density can enlarge the sheath thickness. The plasma density can be significantly reduced by using an electromagnetic, ExB layer, which was discussed in Chapters III and IV. Therefore, the possibility of communication during radio blackout will be maximized through combination of an ExB layer and the two-dimensional shaped electrode.

2. **Numerical studies demonstrated that the application of electric and magnetic fields will produce a significant reduction in the plasma density allowing radio communication through a hypersonic plasma layer. (Chapters III and IV)** Previously, the magnetic window method was the most promising method to allow communication during radio blackout [6]. However, this method was difficult to apply to a reentry or hypersonic vehicle because of the weight of the required magnet. This technical limitation of the magnetic window method was improved via the addition of electric fields which increase the potential density reduction for a given magnetic field strength. This method was called the ExB layer mitigation scheme. The ExB layer method provided stronger plasma density reduction than can be achieved by a magnetic field alone with the same magnetic field strength. Numerical analysis of an ExB layer demonstrated that the applied ExB layer can create a "window" in the reentry plasma layer through which radio waves can be transmitted.

3. **A one-dimensional ExB layer model was developed and the effect of the ExB layer investigated in terms of magnetic field and current density. (Chapter III)** A one-dimensional ExB layer model was proposed with two approximations, namely the plasma-optic and MHD limits. The plasma-optic regime focused on the ExB drift and the MHD regime concentrated on the JxB drift. The numerical results showed that a strong density reduction can be obtained with a high magnetic field and potential drop. However, the maximum magnetic field and potential drop were limited by technical aspects which include the weight of the magnet and the arcing problem. The applicable ranges of the magnetic field and potential drop made it possible to create a solution map which provides a possible configuration of the ExB layer.

4. **A two-dimensional ExB layer model was developed to evaluate the required size of the created window for communication. (Chapter IV)** A two-dimensional ExB layer model was proposed and demonstrated the possibility of the ExB layer as a blackout mitigation scheme. This model showed the optimal location of the transmit antenna and the effective area of the ExB layer. The numerical result showed that the maximum density reduction occurs near the cathode and revealed that the applied ExB layer can effectively reduce the plasma number density outwards to approximately 2 cm from the surface.

5. **The developed ExB layer models were assessed using analytical solution and experimental measurement. (Chapter V)** The ExB layer models were assessed using an analytical solution and experimental results. The suggested ExB layer model provides exact agreement with theory and has good agreement with the measurements. The good agreement demonstrated that the suggested ExB layer models can accurately predict the reduced plasma density in the ExB layer. The numerical and experimental results showed that the applied ExB layer can significantly manipulate the plasma density for communication.

6. **The possibility of the ExB layer as a blackout mitigation scheme was evaluated for the OREX reentry vehicle. (Chapter VI)** OREX was simulated with the ExB layer to demonstrate the capability of the ExB layer as a reentry mitigation scheme. The simulation results demonstrated that the applied ExB layer manipulates the plasma density near the cathode in a hypersonic flow at a 79.9 km reentry condition. The simulation results at 79.9 km

showed that the plasma density of OREX is high enough to cause radio blackout for the UHF, the L-band, and the S-band. For the S-band communication blackout, the ExB layer with 0.3 T provided a sufficient plasma density reduction to enable communication through plasma layer. The ExB layer with 0.5 T and - 800 V potential drop shows the possibility for communication through the plasma layer for the L band and GPS frequency. Consequently, the ExB layer method showed a more effective approach to address radio blackout than the magnetic window.

7.3 Future Work

This study has many possibilities for real-world applications because the ExB layer mitigation scheme can manipulate plasma in a specific region. By adjusting an ExB layer configuration, it is possible to manipulate a plasma in an etching reactor in which a dense plasma layer can improve the etching rate of a wafer; thus, the ExB layer scheme has potential applications in the semiconductor industry. This configuration can also be used for the thermal protection system of a reentry vehicle because an applied magnetic field can shift the position of the shock. Due to diverse and numerous possibilities of an ExB layer, future research can revolve around the development of "plasma manipulation systems", for applications from hypersonic vehicles to the semiconductor industry and include additional models to be developed and incorporated into the ExB layer model. The following sections provide suggested future work.

7.3.1 Electrical conductivity model

In the ExB layer simulation, an empirical model is used for the electrical conductivity that is suggested by Otsu *et al.* This model suggests that the electrical

conductivity is only a function of temperature and attempts to capture the conductivity once it starts to approach a constant at high temperature due to the negligible electrical conductivity at low temperature. Since there is a remarkable difference between the measured electrical conductivity of air and the empirical conductivity model at low temperature, it would be interesting to consider a detailed electrical conductivity model. A more detailed electrical conductivity model could improve the accuracy of the ExB layer simulation and be used for other MHD simulations.

7.3.2 Advanced physical modeling

The current ExB layer model does not include several potentially important physical phenomena such as plasma sheaths, ablation, and radio wave propagation. In order to determine the effectiveness of the system, it is necessary to simulate an ExB layer with a thermal protection system (TPS) because the ExB layer mitigation system should be located under the TPS of a reentry/hypersonic vehicle. The radio wave propagation model is useful for calculating detailed radio wave attenuation in a plasma layer. Radio wave attenuation is useful for determining the required plasma density reduction for communication during radio blackout. A sheath near an electrode can affect the plasma density so it would be interesting to include a plasma sheath model in the ExB layer analysis. Additional models would be useful to investigate detailed physics in an ExB layer and help to expand real-world applications of an ExB layer mitigation scheme.

7.3.3 Improved MHD fluid simulation model

The ExB layer mitigation scheme is an example of MHD flow control. Current MHD simulation models use a one-fluid approximation that is useful only for a neutral plasma application because it assumes ion and electron densities are the

same. However, this model needs to consider the space charge effect for non-neutral plasma applications. In order to consider a space charge, two-fluid approximation models are needed. For some applications, the manipulated plasma density is too low to apply a fluid simulation. In this case, it is necessary to use a kinetic simulation model. Since a fluid model is computationally less expensive than a kinetic model, a kinetic-MHD hybrid simulation model is useful. Therefore, developing a kinetic-MHD hybrid simulation method may point to numerous and diverse applications of an ExB layer.

7.3.4 Analysis of PEPL experiment with 3D magnetic field

In the two-dimensional ExB layer study, a two-dimensional magnetic field is used. However, the magnetic field generated by the electromagnet is three-dimensional. Since the magnetic field is one of the most important parameters which can affect plasma density reduction, the PEPL experiment of the ExB layer is necessary to be numerically analyzed with the three-dimensional magnetic field configuration.

7.3.5 Analysis of OREX with thermal nonequilibrium

The OREX with the ExB layer is simulated with thermal equilibrium condition. The analysis of OREX with thermal nonequilibrium is good to understand the effectiveness of the thermal nonequilibrium condition. Since the radio blackout of the re-entry vehicle occurs both thermal equilibrium and nonequilibrium condition, this analysis give more potential possibility of the ExB layer method as a blackout mitigation method.

7.3.6 Parallelized the hypersonic CFD code with MHD solver

The OREX simulation with the ExB layer uses a single processor for simulation. Since this simulation is computationally very expensive, it is necessary to parallelize the hypersonic CFD code with MHD solver. The parallelize code can reduce a computational cost of the ExB layer simulation.

7.3.7 Analysis of hypersonic vehicle with 3D magnetic field and 3D electric field

In the hypersonic simulation, the axisymmetric magnetic is employed. In real application, the electromagnet could be located below an antenna. In this case, the magnetic field is not axisymmetric. Since the magnetic and electric fields determine the performance of the ExB layer as a plasma manipulation method, an analysis of hypersonic vehicle with three-dimensional magnetic and electric fields can be useful for a design of real applications.

7.3.8 Additional Experiment the ExB layer approach

The previous experiment was performed for the electromagnetic method with a single species plasma. However, an experiment using the electrostatic method was not performed. Since the electrostatic method has a unique advantage compared with other mitigation methods, the combination of the electrostatic and electromagnetic methods could be a more efficient way for solving radio blackout. In addition, the experiment of the electrode-life-time can give more reliability of the ExB layer mothod as a real technology.

APPENDICES

APPENDIX A

Analytical Solution of the One-dimensional ExB Layer

A.1 Analytical Solution for the Plasma-Optic Regime

The derivation of the analytical solution of the one-dimensional ExB layer model in the plasma-optic regime is presented below. The analytical solution is useful to validate the numerical results of the one-dimensional ExB layer model. In this derivation, only the x-direction is considered and the applied magnetic field only has a component in the z-direction. The ion collision and electron pressure drag terms are ignored to simplify the model.

The plasma-optic regime provides the mass and momentum conservation equations for the one-dimensional case as follows:

$$\nabla \left(nV_i \right) = 0 \tag{A.1}$$

$$nm_i \left(V_i \nabla V_i \right) = enE \tag{A.2}$$

$$0 = -en \left(E + V_e \times B \right) - nm_e \nu_e \left(V_e - V_i \right) \tag{A.3}$$

where n is the plasma number density, V is the ion velocity in the x-direction, m_i is the ion mass, m_e is the electron mass, 9.11×10^{-31} kg, and ν_e is the electron collision frequency.

Equation A.2 includes the electric field which can be obtained from Equation A.3.

$$\begin{aligned} E &= \frac{j}{\sigma} - V_e \times B \\ &= \frac{j}{\sigma} - V_{e,y} B \end{aligned} \tag{A.4}$$

where j is the current density which is defined as $j = en\left(V_i - V_e\right)$ and σ is the electrical conductivity, $\sigma = \frac{e^2 n}{m_e \nu_e}$. In a one-dimensional ExB layer model, the current is assumed to be constant. The electron drift velocity in the ExB direction, $V_{e,y}$, is [67]

$$\begin{aligned} V_{e,y} &= -V_e \frac{\omega_e}{\nu_e} \\ &= -\beta V_e \end{aligned} \tag{A.5}$$

where ω_e is the electron cyclotron frequency, $\frac{eB}{m_e}$, and β is the Hall parameter. Thus, Equation A.4 can be expressed as:

$$E = \frac{j}{\sigma} + \beta V_e B \tag{A.6}$$

Equation A.6 still contains an electron velocity, V_e. The electron velocity can be calculated from the definition of the current density as:

$$V_e = V_i - \frac{j}{en} \tag{A.7}$$

Thus, the electric field can be expressed as:

$$E = \frac{j}{\sigma} + \beta B \left(V_i - \frac{j}{en} \right) \tag{A.8}$$

The system of equations, A.1, A.2, and A.8, should be solved analytically to provide unknown variables, n and V_i. Using Equation A.8, the momentum conservation equation, Equation A.2, becomes as follows:

$$nm_i\left(V\nabla V\right) = en\left(\frac{j}{\sigma} + \beta B\left(V_i - \frac{j}{en}\right)\right) \tag{A.9}$$

For the one-dimensional case, nV_i is a constant from Equation A.1.

$$n_0 V_{i,0} = nV_i \tag{A.10}$$

where n_0 is the initial plasma number density and $V_{i,0}$ is the initial ion velocity. Equation A.9 can be simplified by dividing by $n_0 V_{i,0}$ as follows:

$$\frac{dV_i}{dx} = \frac{e}{m_i}\left\{\frac{j}{n_0 V_{i,0}}\cdot\frac{n}{\sigma} + \underbrace{\beta B}_{constant} - \underbrace{\beta B\cdot\frac{j}{e}\cdot\frac{1}{n_0 V_{i,0}}}_{constant}\right\} \tag{A.11}$$

where the last two terms are constants. Equation A.11 contains a $\frac{n}{\sigma}$ term. This can be expressed as:

$$\begin{aligned}\frac{n}{\sigma} &= \frac{n}{\frac{e^2 n}{m_e\nu_e}} \\ &= \frac{m_e\nu_e}{e^2} = constant\end{aligned} \tag{A.12}$$

The ion velocity distribution along the x-direction can be obtained:

$$V_i\left(x\right) = V_{i,0} + \left(\frac{m_e}{m_i}\cdot\frac{nu_e}{e}\cdot\frac{j}{n_0 V_{i,0}} + \omega_i\beta\left(1 - \frac{j}{e}\cdot\frac{1}{n_0 V_{i,0}}\right)\right)\cdot x \tag{A.13}$$

Therefore, the density reduction ratio, n/n_0, at $x = L$ can be calculated as

$$N = \frac{n_0 V_{i,0}}{V_{i,0} + \left(\frac{m_e}{m_i}\cdot\frac{\nu_e}{e}\cdot\frac{j}{n_0 V_{i,0}} + \omega_i\beta\left(1 - \frac{j}{e}\cdot\frac{1}{n_0 V_{i,0}}\right)\right)\cdot L} \tag{A.14}$$

where N is the plasma density reduction, n/n_0, and L is the inter-electrode length.

A.2 Analytical Solution for the MHD Regime

The derivation of the analytical solution of the one-dimensional ExB layer model in the MHD regime is presented below. The analytical solution is useful to validate the numerical results of the one-dimensional ExB layer model. In this derivation, only the x-direction is considered and the applied magnetic field only has a component in the z-direction. The ion collision drag terms are ignored to simplify the model.

The MHD regime provides the mass and momentum conservation equations for the one-dimensional case as follows:

$$\nabla \left(nV_i \right) = 0 \tag{A.15}$$

$$nm_i \left(V_i \nabla V_i \right) + k \left(T_i + T_e \right) \nabla n = j \times B \tag{A.16}$$

where n is the plasma number density, V is the ion velocity in x-direction, m_i is the ion mass, T_i is the ion temperature, T_e is the electron temperature, k is the Boltzmann constant, and j is the current density.

For the one-dimensional case, nV_i is a constant from Equation A.15.

$$n_0 V_{i,0} = nV_i \tag{A.17}$$

where n_0 is the initial plasma number density and $V_{i,0}$ is the initial ion velocity. Equation A.16 can be simplified by dividing by $n_0 V_{i,0}$ as follows:

$$\frac{dV_i}{dx} = \left(\frac{jB_z}{m_i} \cdot \frac{1}{n_0 V_{i,0}} \right) + \left(\frac{k \left(T_i + T_e \right)}{m_i} \right) \cdot \frac{1}{n_0 V_{i,0}} \frac{dn}{dx} \tag{A.18}$$

For the one-dimensional case, Equation A.15 becomes:

$$n \frac{dV_i}{dx} + V_i \frac{dn}{dx} = 0 \tag{A.19}$$

Using Equation A.19, $\frac{dn}{dx}$ can be expressed in terms of $\frac{dV}{dx}$ as follows:

$$\frac{dn}{dx} = -\frac{n}{V_i}\frac{dV_i}{dx} \tag{A.20}$$

Using Equation A.20, Equation A.18 becomes:

$$\begin{aligned} \frac{dV_i}{dx} &= \left(\frac{jB_z}{m_i}\cdot\frac{1}{n_0 V_{i,0}}\right) - \left(\frac{k\left(T_i+T_e\right)}{m_i}\right)\cdot\frac{1}{n_0 V_{i,0}}\left(\frac{n}{V_i}\frac{dV_i}{dx}\right) \\ &= \left(\frac{jB_z}{m_i}\cdot\frac{1}{n_0 V_{i,0}}\right) - \left(\frac{k\left(T_i+T_e\right)}{m_i}\right)\cdot\frac{1}{V_i^2}\frac{dV_i}{dx} \end{aligned} \tag{A.21}$$

Therefore, the differential equation for ion velocity can be obtained:

$$\left(1+\left(\frac{k\left(T_i+T_e\right)}{m_i}\right)\cdot\frac{1}{V_i^2}\right)\frac{dV_i}{dx} = \underbrace{\frac{jB_z}{m_i}\cdot\frac{1}{n_0 V_{i,0}}}_{constant} \tag{A.22}$$

$$\left(1+\left(\frac{k\left(T_i+T_e\right)}{m_i}\right)\cdot\frac{1}{V_i^2}\right)dV_i = \left(\underbrace{\frac{jB_z}{m_i}\cdot\frac{1}{n_0 V_{i,0}}}_{constant}\right)dx \tag{A.23}$$

At the end of the ExB layer, $x = L$, Equation A.23 can be solved as:

$$\left[V_i - \frac{k\left(T_i+T_e\right)}{m_i}\cdot\frac{1}{V_i}\right] - \left[V_{i,0} - \frac{k\left(T_i+T_e\right)}{m_i}\cdot\frac{1}{V_{i,0}}\right] = \left(\frac{jB_z}{m_i}\cdot\frac{1}{nV_{i,0}}\right)\cdot L \tag{A.24}$$

Solving for ion velocity V_i, one can arrive at the following:

$$V_i = \frac{\left(\frac{k(T_i+T_e)}{m_i V_{i,0}} - V_{i,0} + \left(\frac{jB_z}{m_i}\frac{L}{n_0 V_{i,0}}\right)\right) \pm \sqrt{\left(-\frac{k(T_i+T_e)}{m_i V_{i,0}} + V_{i,0} - \left(\frac{jB_z}{m_i}\frac{L}{n_0 V_{i,0}}\right)\right)^2 - 4\frac{k(T_i+T_e)}{m_i}}}{2} \tag{A.25}$$

The second term of the right-hand side should have a positive sign, because velocity is accelerated along the x-direction. Therefore, ion velocity V_i at $x = L$ becomes

$$V_i = \frac{\left(\frac{k(T_i+T_e)}{m_i V_{i,0}} - V_{i,0} + \left(\frac{jB_z}{m_i}\frac{L}{n_0 V_{i,0}}\right)\right) + \sqrt{\left(-\frac{k(T_i+T_e)}{m_i V_{i,0}} + V_{i,0} - \left(\frac{jB_z}{m_i}\frac{L}{n_0 V_{i,0}}\right)\right)^2 - 4\frac{k(T_i+T_e)}{m_i}}}{2} \tag{A.26}$$

The density reduction ratio n/n_0 at $x = L$ can be calculated from Equation A.27:

$$N = \frac{2V_{i,0}}{\left(\frac{k(T_i+T_e)}{m_i V_{i,0}} - V_{i,0} + \left(\frac{jB_z}{m_i}\frac{L}{n_0 V_{i,0}}\right)\right) + \sqrt{\left(-\frac{k(T_i+T_e)}{m_i V_{i,0}} + V_{i,0} - \left(\frac{jB_z}{m_i}\frac{L}{n_0 V_{i,0}}\right)\right)^2 - 4\frac{k(T_i+T_e)}{m_i}}} \tag{A.27}$$

where N is the plasma density reduction, n/n_0, and L is the inter-electrode length.

APPENDIX B

Thermalized Potential

The derivation of the thermalized potential is presented below. From the steady-state electron momentum equation, an Ohm's law can be expressed as [109]:

$$\eta\vec{\mathbf{j}}_e = \vec{\mathbf{E}} + \frac{\nabla p_e - \vec{\mathbf{j}}_e \times \vec{\mathbf{B}}}{en} - \eta_{ei}\vec{\mathbf{j}}_i \tag{B.1}$$

where

$$\begin{aligned}
\eta &= \text{electron mobility} \\
\vec{\mathbf{E}} &= \text{electric field} \\
\vec{\mathbf{j}}_e &= \text{electric current density} \\
\vec{\mathbf{j}}_i &= \text{ion current density} \\
\vec{\mathbf{B}} &= \text{magnetic field} \\
p_e &= \text{electron pressure}
\end{aligned}$$

A schematic of the thermalized potential with the magnetic field line geometry is shown in Figure B.1. In the magnetic frame of reference, the current density can be expressed as:

$$\vec{\mathbf{j}} = j_\perp \eta_\perp + j_\parallel \eta_\parallel + j_\wedge \eta_\wedge \tag{B.2}$$

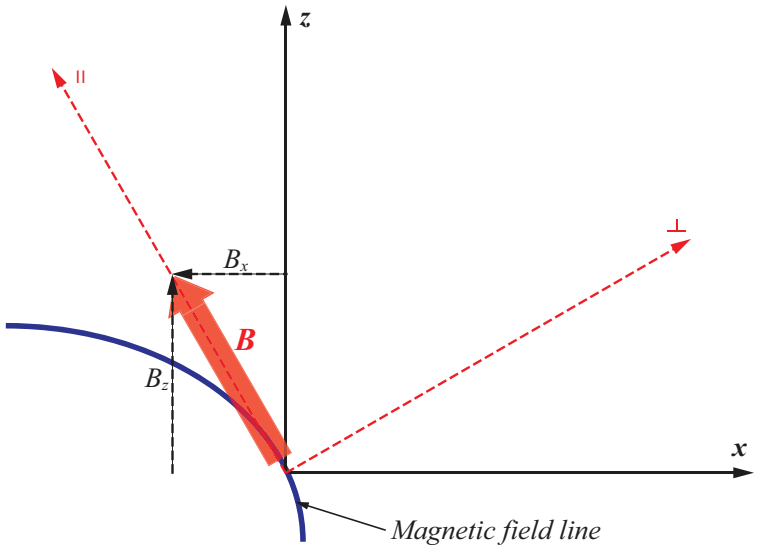

Figure B.1: A schematic of the thermalized potential with the magnetic field line geometry

where the subscripts, $\perp$, $\|$, and $\wedge$, represent the directions perpendicular, parallel, and transverse i. e. the ExB drift direction, respectively, to the local magnetic field line and η is the electron mobility.

In the direction along the magnetic field lines, the $\vec{\mathbf{j}} \times \vec{\mathbf{B}}$ cross product in the electron momentum equation is zero [109]. Therefore, Equation B.1 becomes:

$$\eta j_{e,\|} = E_\| + \frac{\nabla_\| p_e}{en} - \eta_{ei} j_{i,\|} \tag{B.3}$$

Then, along the magnetic field line, the electric field can be written as:

$$\begin{aligned} E_\| &= \frac{\nabla_\|}{en} + \eta_\| j_{e,\|} - \eta_{ei,\|} j_{i,\|} \\ &= -\nabla_\| \phi \end{aligned} \tag{B.4}$$

$$\tag{B.5}$$

With the standard assumption used along magnetic fields in many plasmas of zero net current, $j_{e,\|} \approx j_{i,\|}$, and constant electron temperature, Equation B.5 can be solved for the potential along the field line to give

$$\phi = \phi_0 + T_e \ln\left(\frac{n}{n_0}\right) \tag{B.6}$$

where ϕ_0 and n_0 are the reference potential and electron number density, respectively. Equation B.6 is called the thermalized potential in the Hall thruster literature and was originally proposed by Morozov [110].

APPENDIX C

Electrical conductivity tensor

The detailed derivations of the electrical conductivity tensor are presented below. The generalized Ohm's law can be written in vector form [103]:

$$\vec{\mathbf{J}} = \sigma \left[\vec{\mathbf{E}} + \vec{\mathbf{U}} \times \vec{\mathbf{J}} - \beta \left(\vec{\mathbf{J}} \times \vec{\mathbf{B}} \right) + \alpha \left(\vec{\mathbf{J}} \times \vec{\mathbf{B}} \times \vec{\mathbf{j}} \right) \right] \tag{C.1}$$

where σ is the electrical conductivity, β is the Hall parameter, and α is an ion-slip coefficient. The component form of Equation C.1 becomes:

$$\begin{aligned} \begin{pmatrix} J_x \\ J_y \\ J_z \end{pmatrix} &= \sigma \begin{pmatrix} \left(\vec{\mathbf{E}} + \vec{\mathbf{U}} \times \vec{\mathbf{B}} \right)_x \\ \left(\vec{\mathbf{E}} + \vec{\mathbf{U}} \times \vec{\mathbf{B}} \right)_y \\ \left(\vec{\mathbf{E}} + \vec{\mathbf{U}} \times \vec{\mathbf{B}} \right)_z \end{pmatrix} - \sigma\beta \begin{pmatrix} J_y B_z - J_z B_y \\ J_z B_x - J_x B_z \\ J_x B_y - J_y B_x \end{pmatrix} \\ &+ \sigma\alpha \begin{pmatrix} -\left(B_y^2 + B_z^2 \right) J_x + B_x B_y J_y + B_x B_z J_z \\ B_x B_y J_x - \left(B_x^2 + B_z^2 \right) J_y + B_y B_z J_z \\ B_x B_z J_x + B_y B_z J_y - \left(B_x^2 + B_y^2 \right) J_z \end{pmatrix} \end{aligned} \tag{C.2}$$

Equation C.2 can be simplified using a matrix form as:

$$\begin{pmatrix} J_x \\ J_y \\ J_z \end{pmatrix} = \sigma \begin{pmatrix} \left(\vec{\mathbf{E}} + \vec{\mathbf{U}} \times \vec{\mathbf{B}}\right)_x \\ \left(\vec{\mathbf{E}} + \vec{\mathbf{U}} \times \vec{\mathbf{B}}\right)_y \\ \left(\vec{\mathbf{E}} + \vec{\mathbf{U}} \times \vec{\mathbf{B}}\right)_z \end{pmatrix} - \sigma\beta \begin{pmatrix} 0 & B_z & -B_y \\ -B_z & 0 & B_x \\ B_y & -B_x & 0 \end{pmatrix} \begin{pmatrix} J_x \\ J_y \\ J_z \end{pmatrix} + \sigma\alpha \begin{pmatrix} -\left(B_y^2 + B_z^2\right) & B_x B_y & B_x B_z \\ B_x B_y & -\left(B_x^2 + B_z^2\right) & B_y B_z \\ B_x B_x & B_y B_z & -\left(B_x^2 + B_y^2\right) \end{pmatrix} \begin{pmatrix} J_x \\ J_y \\ J_z \end{pmatrix} \tag{C.3}$$

Equation C.3 is rewritten to solve the current density, $\vec{\mathbf{J}}$, as:

$$\begin{pmatrix} 1 + \sigma\alpha\left(B_y^2 + B_z^2\right) & -\sigma\alpha B_x B_y + \sigma\beta B_z & -\sigma\alpha B_x B_z - \sigma\beta B_y \\ -\sigma\alpha B_x B_y - \sigma\beta B_z & 1 + \sigma\alpha\left(B_x^2 + B_z^2\right) & -\sigma\alpha B_y B - z + \sigma\beta B_x \\ -\sigma\alpha B_x B_z + \sigma\beta B_y & -\sigma\alpha B_y B_z - \sigma\beta B_x & 1 + \sigma\alpha\left(B_x^2 + B_y^2\right) \end{pmatrix} \vec{\mathbf{J}} = \sigma\left(\vec{\mathbf{E}} + \vec{\mathbf{U}} \times \vec{\mathbf{B}}\right) \tag{C.4}$$

This equation allows to calculate a current density using an electric field, velocity, and magnetic field. Therefore, the current density can be written as:

$$\vec{\mathbf{J}} = \sigma \begin{pmatrix} 1 + \sigma\alpha\left(B_y^2 + B_z^2\right) & -\sigma\alpha B_x B_y + \sigma\beta B_z & -\sigma\alpha B_x B_z - \sigma\beta B_y \\ -\sigma\alpha B_x B_y - \sigma\beta B_z & 1 + \sigma\alpha\left(B_x^2 + B_z^2\right) & -\sigma\alpha B_y B - z + \sigma\beta B_x \\ -\sigma\alpha B_x B_z + \sigma\beta B_y & -\sigma\alpha B_y B_z - \sigma\beta B_x & 1 + \sigma\alpha\left(B_x^2 + B_y^2\right) \end{pmatrix}^{-1} \left(\vec{\mathbf{E}} + \vec{\mathbf{U}} \times \vec{\mathbf{B}}\right) \tag{C.5}$$

Equation C.5 may be expressed as:

$$\vec{\mathbf{J}} = \tilde{\sigma} \cdot \left(\vec{\mathbf{E}} + \vec{\mathbf{U}} \times \vec{\mathbf{B}}\right) \tag{C.6}$$

where $\tilde{\sigma}$ is a conductivity tensor. Equation C.6 is known as the generalized Ohm's law. In this case, the conductivity tensor can be found from an inverted matrix of

Equation C.5.

$$\tilde{\sigma} = \begin{pmatrix} 1+\sigma\alpha\left(B_y^2+B_z^2\right) & -\sigma\alpha B_xB_y+\sigma\beta B_z & -\sigma\alpha B_xB_z-\sigma\beta B_y \\ -\sigma\alpha B_xB_y-\sigma\beta B_z & 1+\sigma\alpha\left(B_x^2+B_z^2\right) & -\sigma\alpha B_yB-z+\sigma\beta B_x \\ -\sigma\alpha B_xB_z+\sigma\beta B_y & -\sigma\alpha B_yB_z-\sigma\beta B_x & 1+\sigma\alpha\left(B_x^2+B_y^2\right) \end{pmatrix}^{-1}$$

$$= \frac{1}{D}\begin{pmatrix} \sigma_{11} & \sigma_{12} & \sigma_{13} \\ \sigma_{21} & \sigma_{22} & \sigma_{23} \\ \sigma_{31} & \sigma_{32} & \sigma_{33} \end{pmatrix} \tag{C.7}$$

where the coefficient σ_{ij} is:

$$\begin{aligned} \sigma_{11} &= \left(1+\sigma\alpha\left(B_x^2+B_y^2+B_z^2\right)\right)\left(1+\sigma\alpha B_x^2\right)+\sigma^2\beta^2B_x^2 \\ &= \left(1+\sigma\alpha\vec{\mathbf{B}}^2\right)\left(1+\sigma\alpha B_x^2\right)+\sigma^2\beta^2B_x^2 \qquad \text{(C.8)} \\ \sigma_{12} &= \sigma\left[\alpha B_xB_y\left(1+\sigma\alpha\left(B_x^2+B_y^2+B_z^2\right)\right)-\beta\left(B_z-\sigma\beta B_xB_y\right)\right] \\ &= \sigma\left[\alpha B_xB_y\left(1+\sigma\alpha\vec{\mathbf{B}}^2\right)-\beta\left(B_z-\sigma\beta B_xB_y\right)\right] \qquad \text{(C.9)} \\ \sigma_{13} &= \sigma\left[\alpha B_xB_z\left(1+\sigma\alpha\left(B_x^2+B_y^2+B_z^2\right)\right)+\beta\left(B_y+\sigma\beta B_xB_z\right)\right] \\ &= \sigma\left[\alpha B_xB_z\left(1+\sigma\alpha\vec{\mathbf{B}}^2\right)+\beta\left(B_y+\sigma\beta B_xB_z\right)\right] \qquad \text{(C.10)} \end{aligned}$$

$$\begin{aligned} \sigma_{21} &= \sigma\left[\alpha B_xB_y\left(1+\sigma\alpha\left(B_x^2+B_y^2+B_z^2\right)\right)+\beta\left(B_z+\sigma\beta B_xB_y\right)\right] \\ &= \sigma\left[\alpha B_xB_y\left(1+\sigma\alpha\vec{\mathbf{B}}^2\right)+\beta\left(B_z+\sigma\beta B_xB_y\right)\right] \qquad \text{(C.11)} \\ \sigma_{22} &= \left(1+\sigma\alpha\left(B_x^2+B_y^2+B_z^2\right)\right)\left(1+\sigma\alpha B_y^2\right)+\sigma^2\beta^2B_y^2 \\ &= \left(1+\sigma\alpha\vec{\mathbf{B}}\right)\left(l+\sigma\alpha B_y^2\right)+\sigma^2\beta^2B_y^2 \qquad \text{(C.12)} \\ \sigma_{23} &= \sigma\left[\alpha B_yB_z\left(1+\sigma\alpha\left(B_x^2+B_y^2+B_z^2\right)\right)-\beta\left(B_x-\sigma\beta B_yB_z\right)\right] \\ &= \sigma\left[\alpha B_yB_z\left(1+\sigma\alpha\vec{\mathbf{B}}^2\right)-\beta\left(B_x-\sigma\beta B_yB_z\right)\right] \qquad \text{(C.13)} \end{aligned}$$

$$\begin{aligned}
\sigma_{31} &= \sigma\left[\alpha B_x B_z\left(1+\sigma\alpha\left(B_x^2+B_y^2+B_z^2\right)\right)-\beta\left(B_y-\sigma\beta B_x B_z\right)\right] \\
&= \sigma\left[\alpha B_x B_z\left(1+\sigma\alpha\vec{\mathbf{B}}^2\right)-\beta\left(B_y-\sigma\beta B_x B_z\right)\right] \qquad \text{(C.14)} \\
\sigma_{32} &= \sigma\left[\alpha B_y B_z\left(1+\sigma\alpha\left(B_x^2+B_y^2+B_z^2\right)\right)+\beta\left(B_x+\sigma\beta B_y B_z\right)\right] \\
&= \sigma\left[\alpha B_y B_z\left(1+\sigma\alpha\vec{\mathbf{B}}^2\right)+\beta\left(B_x+\sigma\beta B_y B_z\right)\right] \qquad \text{(C.15)} \\
\sigma_{33} &= \left(1+\sigma\alpha\left(B_x^2+B_y^2+B_z^2\right)\right)\left(1+\sigma\alpha B_z^2\right)+\sigma^2\beta^2 B_z^2 \\
&= \left(1+\sigma\alpha\vec{\mathbf{B}}^2\right)\left(l+\sigma\alpha B_z^2\right)+\sigma^2\beta^2 B_z^2 \qquad \text{(C.16)}
\end{aligned}$$

and the denominator, D, is:

$$\begin{aligned}
D &= \left(1+\sigma\alpha\left(B_x^2+B_y^2+B_z^2\right)\right)^2+\left(\sigma\beta\left(B_x^2+B_y^2+B_z^2\right)\right)^2 \\
&= \left(1+\sigma\alpha\vec{\mathbf{B}}^2\right)^2+\left(\sigma\beta\vec{\mathbf{B}}^2\right)^2 \qquad \text{(C.17)}
\end{aligned}$$

BIBLIOGRAPHY

BIBLIOGRAPHY

[1] Wood, G. E., Asmar, S. W., Rebold, T. A., and Lee, R. A., "Mars Pathfinder Entry, Decent, and Landing Communicstions," Tech. rep., Jet Propulsion Laboratory, Pasadena, CA, The Telecommunications and Data Acquisition Progress Report 42-131, July-September 1997.

[2] *Manual of Regulations and Procedures for Federal Radio Frequency Management*, National Telecommunications and Information Administration, Washington, D.C., may 2003 ed., 2007, Jan. 2007 revised.

[3] *United States Frequency Allocations: The Radio Spectrum*, National Telecommunications and Information Administration, Washington, D.C., 2003.

[4] Yamamoto, Y. and Yoshioka, M., "CFD and FEM Coupling Analysis of OREX Aerothermodynamic Flight Data," *AIAA 95-2087*, June 1995, presented at 30th Thermophysics Conference, San Diego, CA.

[5] Starkey, R., Lewis, R., and Jones, C., "Plasma Telemetry in Hypersonic Flight," *International Foundation for Telemetering Paper 02-15-2*, October 2002, International Telemetering Conference, San Diego, CA.

[6] Hartunian, R. A., Stewart, G. E., Fergason, S. D., Curtiss, T. J., and Seibold, R. W., "Cause and Mitigations Radio Frequency (RF) Blackout During re-entry of Reusable Launch Vehicles," ATR 2007(5309)-1, AEROSPACE CORPORATION, 2007, ATR-2007(5309)-1.

[7] Rybak, J. P. and Churchill, R. J., "Progress in Re-entry Communications," *IEEE Transactions on Aerospace and Electronic Systems*, Vol. aes-7, No. 5, 1971, pp. 879–894.

[8] Sims, T. E. and Jones, R. F., "Flight Measurements of VHF-signal Attenuation and Antenna Impedence for the RAM A-1 Slender Probe at Velocities up to 17,800 feet per second," TM X-760, NASA, 1963.

[9] Russo, F. P. and Hughes, J. K., "Measurements of The Effects of Static Magnetic Fields on VHF Transmission in Ionized Flow Fields," TM X-907, NASA, 1964.

[10] Lehnert, R. and Rosenbaum, B., "Plasma Effects on Apollo Re-entry Communication," TN D-2732, NASA, 1965.

[11] Rawhouser, R., "Overview of the AF Avionics Laboratory Re-entry Electromagnetics Program," *The Rntry Plasma Sheath and its Effects on Space Vehicle Electromagnetic Systems*, Vol. I, NASA Langley Research Center, 1964, pp. 3–17, NASA SP-252.

[12] Keidar, M., Kim, M., and Boyd, I. D., "Electromagnetic Reduction of Plasma Density During Atmospheric Reentry and Hypersonic Flights," *Journal of Spacecraft and Rockets*, Vol. 45, No. 3, 2008, pp. 445–453.

[13] Rogers, L., *It's ONLY Rocket Science*, Astronomers' Universe, Springer New York, 2008.

[14] Boyd, I. D., "Modeling of Plasma Formation in Rarefied Hypersonic Entry Flows," *AIAA 2007-206*, January 2007, presented at 45th AIAA Aerospace Sciences Meeting and Exhibit, Reno, Nevada.

[15] Scalabrin, L. C., *Numerical Simulation of Weakly Ionized Hypersonic Flow Over Re-entry Capsules*, 2007, PhD thesis, Department of Aerospace Engineering, University of Michigan.

[16] *Columbia Accident Investigation Board Report*, Columbia Accident Investigation Board, 2003, Printing Office, Washington, DC.

[17] Dabbs, J. H. and Schmidt, O. L., "Apollo Experience Report - Voice Communications Techniques And Performance," TN D-6739, NASA, March 1972.

[18] Sakurai, H., Kobayasi, M., Yamazaki, I., Shirouzu, M., and Yamamoto, M., "Development of the Hypersonic Flight Experimental Vehicle," *Acta Astronautica*, Vol. 40, No. 2-8, 1997, pp. 105–112, Enlarging The Scope of Space Applications.

[19] Peltzer, K. E., "Apollo Unified S-Band System," TM X-55492, NASA, April 1966.

[20] Vacchione, J., Burke, K., Huang, J., Otoshi, T., and Smith, H., "A Novel Waveguide Antenna System for the Mars Pathfinder Spacecraft/Lander," Vol. 3, Jul 1996, pp. 1704–1707.

[21] Davies, K., *Ionospheric Radio Propagation*, National Bureau of Standards Monograph 80, 1965.

[22] Morabito, D. D., "The Spacecraft Communications Blackout Problem Encountered during Passage or Entry of Planetary Atmospheres," Progress Report 42-150, IPN, 2002.

[23] Spencer, D. F., "An Evaluation of the Communication Blackout Problem for a Blunt Mars-Entry Capsule and a Potential Method for the Elimination of Blackout," Technical Report 32-594, Jet Propulsion Laboratory, Pasadena, Califonia, April 15 1964.

[24] Belov, I. F., Borovoy, V. Y., Gorelov, V. A., Kireev, A. Y., Korolev, A. S., and Stepanov, E. A., "Investigation of Remote Antenna Assembly for Radio Communication with Reentry Vehicle," *Journal of Spacecraft and Rockets*, Vol. 38, No. 2, 2001, pp. 249–256.

[25] Hunter, S. R., Carter, J. G., and Christophorou, L. G., "Low Energy Electron Attachment to SF_6 in N_2, Ar, and Xe buffer gases," *Journal of Chemical Physics*, Vol. 90, No. 9, 1989, pp. 4879–4891.

[26] Kowari, K., Leung, K., and Shizgal, B. D., "The Coupling of Electron Thermalization and Electron Attachment in CCl_4/Ar and CCl_4/Ne Mixtures," *Journal of Chemical Physics*, Vol. 108, No. 4, 1998, pp. 1587–1600.

[27] Beckwith, I. E. and Huffman, J. K., "Injection and Distribution of Liquids in the Flow Fields of Blunt Shapes at Hypersonic Speeds," TM X-989, NASA, August 1964.

[28] Hinson, W. F., Gooderum, P. B., and Bushell, D. M., "Experimental Investigation of Multiple-Jet Liquid Injection into Hypersonic Flow," TN D-5861, NASA, June 1970.

[29] Weaver, W. L., "Multiple-Orifice Liquid Injection into Hypersonic Air Streams and Application to RAM C-III Flight," TM X-2486, NASA, 1972, NASA TM X-2486.

[30] Starkey, R., Lewis, R., and Jones, C., "Electromagnetic Wave/Magnetoactive Plasma Sheath Interaction for Hypersonic Vehicle Telemetry Blackout Analysis," *AIAA 2003-4167*, June 2003, presented at 34th AIAA Plasmadynamics and Lasers Conference.

[31] Hodara, H., "The Use of Magnetic Fields in the Elimination of the Re-Entry Radio Blackout," *Proceedings of the IRE*, Vol. 49, No. 12, Dec. 1961, pp. 1825–1830.

[32] Usui, H., Matsumoto, H., Yamashita, F., Yamane, M., and Takenaka, S., "Computer Experiments on Radio Blackout of a Reentry Vehicle," *Proceedings of the 6th Spacecraft Charging Conference*, Nov 1998, pp. 107–110.

[33] Nazarenko, S. V., Newell, A. C., and Zakharov, V. E., "Communication through Plasma Sheaths via Raman (Three-wave) Scattering Process," *Physics of Plasmas*, Vol. 1, No. 9, 1994, pp. 2827–2834.

[34] Kim, M., Keidar, M., and Boyd, I. D., "Analysis of an Electromagnetic Mitigation Scheme for Reentry Telemetry Through Plasma," *Journal of Spacecraft and Rockets*, Vol. 45, No. 6, 2008, pp. 1223–1229.

[35] Choinière, E. and Gilchrist, B. E., "Self-Consistent 2-D Kinetic Simulations of High-Voltage Plasma Sheaths Surrounding Ion-Attracting Conductive Cylinders in Flowing Plasmas," *IEEE Transactions on Plasma Science*, Vol. 35, No. 1, 2007, pp. 7–22.

[36] Kim, M., Keidar, M., and Boyd, I. D., "Electrostatic Manipulation of a Hypersonic Plasma Layer: Images of the 2D Sheath," *IEEE Transactions on Plasma Science*, Vol. 36, No. 4, 2008, pp. 1198–1199.

[37] Child, C. D., "Discharge From Hot CaO," *Physical Review (Series I)*, Vol. 32, No. 5, May 1911, pp. 492–511.

[38] Langmuir, I., "The Effect of Space Charge and Residual Gases on Thermionic Currents in High Vacuum," *Physical Review*, Vol. 2, No. 6, Dec. 1913, pp. 450–486.

[39] Bilen, S. G. and Gilchrist, B. E., "Transient Plasma Sheath Model for Thin Conductors Excited by Negative High Voltages with Application to Electrodynamic Tethers," *Plasma Science, IEEE Transactions on*, Vol. 28, No. 6, Dec 2000, pp. 2058–2074.

[40] Keidar, M., Monteiro, O. R., Anders, A., and Boyd, I. D., "Magnetic Field Effects on the Sheath Thickeness in Plasma Immersion Ion Implantation," *Applied Physics Letters*, Vol. 81, No. 7, 2002, pp. 1183–1185.

[41] McMahon, J. C., Xu, G. Z., and G., L. J., "The Effect of Ion Drift on the Sheath, Presheath, and Ion-current Collection for Cylinders in a Collisionless Plasma," *Physics of Plasmas*, Vol. 12, No. 6, 2005, pp. 062109–1–062109–11.

[42] Porwitzky, A. J., Keidar, M., and D., B. I., "On the Mechanism of Energy Transfer in the Plasma-Propellant Interaction," *Propellant, Explosive, Pyrotechnics*, Vol. 32, No. 5, 2007, pp. 385–391.

[43] Dendy, R. O., *Plasma Dynamics*, Oxford University Press, 1990.

[44] Li, S., "An HLLC Riemann Solver for Magneto-hydrodynamics," *Journal of Computational Physics*, Vol. 203, No. 1, 2005, pp. 344–357.

[45] Franklin, R. N., "What Significance Does the Bohm Criterion have in an Active Collisional Plasma-Sheath?" *Journal of Physics D: Applied Physics*, Vol. 35, No. 18, 2002, pp. 2270–2273.

[46] Lieberman, M. A. and Lichtenberg, A. J., *Principles of Plasma Discharges and Materials Processing*, Wiley-interscience, 2nd ed., 2005.

[47] Keidar, M., Boyd, I. D., and Beilis, I. I., "Plasma Flow and Plasma-Wall Transition in Hall Thruster Channel," *Physics of Plasmas*, Vol. 8, No. 12, 2001, pp. 5315–5322.

[48] Grantham, W. L., "Flight Results of a 25000-foot-per-second Re-entry Experiment using Microwave Reflectometers to Measure Plasma Electron Density and Standoff Distance," TN D-6062, NASA, 1970.

[49] Jones, W. L. and Cross, A. E., "Electrostatic Probe Measurements of Plasma Parameters for Two Re-entry Flight Experiments at 25000 feet-per-second," TIC D-6617, NASA, 1972.

[50] Kim, D. and Economou, D. J., "Simulation of a Two-dimensional Sheath Over a Flat Wall with an Insulator/Conductor Interface Exposed to a High Density Plasma," *Journal of Applied Physics*, Vol. 94, No. 5, Sep 2003, pp. 2852–2857.

[51] Rakhovskii, V. I., "Arc Formation at Contacts on Switching Off High Currents," *Powder Metallurgy and Metal Ceramics*, Vol. 1, No. 1, 1962, pp. 30–33.

[52] Lin, C.-S., Huang, J.-J., Lo, C.-S., and Chuang, L.-S., "Control of Arcing Problem in the Passivation HDP Deposition Process Solution," *2002 Semiconductor Manufacturing Technology Workshop (IEEE Cat. No. 02EX613)*, 2002, pp. 161–164.

[53] Kim, M., Keidar, M., Boyd, I. D., and Morris, D. P., "Plasma Density Reduction using Electromagnetic ExB Field During Re-entry Flight," *International Foundation for Telemetering Paper 07-19-03*, October 2007, International Telemetering Conference, Las Vegas, NV.

[54] Leung, E., Hilal, M., Parmer, J., and Peck, S., "Lightweight Magnet for Space Applications," *Magnetics, IEEE Transactions on*, Vol. 23, No. 2, March 1987, pp. 1331–1335.

[55] Chapman, J. N., Schmidt, H. J., Ruoff, R. S., Chandrasekhar, V., Dikin, D. A., and Litchford, R. J., "Flightweight Magnets for Space Application using Carbon Nanotubes," *AIAA 2003-330*, January 2003, presented at 41th AIAA Aerospace Sciences Meeting and Exhibit, Reno, Nevada.

[56] Brown, M. J. and McWilliams, R., "Convective Flow Zones in Filament-Discharge Plasma Sources," *Journal of Instrumentation*, Vol. 2, No. 01, 2007, pp. P01008.

[57] Li, X., Fu, D., and Ma, Y., "Direct Numerical Simulation of Hypersonic Boundary-Layer Transition over a Blunt Cone," *AIAA JOURNAL*, Vol. 46, No. 11, 2008, pp. 2899–2913.

[58] Davidson, P. A., *An Introduction to Magnetohydrodynamics*, Cambridge University Press, 2001.

[59] Shang, J. S., Menart, J., Kimmel, R. L., and Hayes, J., "Hypersonic Inlet with Plasma Induced Compression," *AFRL-VA-WP-TP-2006-333*, Jan 2006.

[60] TODD, J. F. J., "Recommendations for Nomenclature and Symbolism for Mass Spectroscopy (Including an Appendix of Terms Used in Vacuum Technology)," *International Journal of Mass Spectrometry and Ion Processes*, Vol. 142, No. 3, 1995, pp. 209–240.

[61] Gryzinski, M., "Classical Theory of Atomic Collisions. I. Theory of Inelastic Collisions," *Physical Reviev*, Vol. 138m, No. 2A, 1967, pp. A336–A358.

[62] Huo, W., "Electron-Impact Excitation and Ionization in Air," *AIAA 2008-1207*, January 2008, presented at 46th AIAA Aerospace Sciences Meeting and Exhibit, Reno, Nevada.

[63] Tchuen, G. and Zeitoun, D. E., "Computation of Weakly Ionized Air Flow in Thermochenical Nonequilibrium Over Sphere-Cones," *International Journal of Heat and Fluid Flow*, Vol. 29, No. 5, 2008, pp. 1393 – 1401.

[64] Boyd, I. D., "Modeling of Associative Ionization Reactions in Hypersonic Rarefied Flows," *Physics of Fluids*, Vol. 19, No. 9, 2007, pp. 096102.

[65] Kang, S. W., Dunn, M. G., and Jones, W. L., "Theoretical and Measured Electron-Density Distributions for the Ram Vehicle at High Altitudes," *AIAA 1972-689*, June 1972, presented at 5th AIAA Fluid and Plasma Dynamics Conference, Boston, MA.

[66] Lemmer, K., Gallimore, A., Smith, T., S., N., Morris, D., Davis, C., and Zagel, J., "Simulating Hypersonic Atmospheric Conditions in a Laboratory Setting Using a 15-Cm-Diameter Helicon Source," *ICOPS-2007-1489*, June 2007, presented at 34th IEEE International Conference on Plasma Science (ICOPS), Albuquerque, New Mexico.

[67] Keidar, M. and Beilis, I. I., "Electron Transport Phenomena in Plasma Devices with ExB Drift," *IEEE Transaction on Plasma Science*, Vol. 34, No. 3, 2006, pp. 804–814.

[68] Merlino, R. L. and D'Angelo, N., "Electron and Ion Inertia Effects on Current-Driven Collisional Dust Acoustic, Dust Ion Acoustic, and Ion Acoustic Instabilities," *Physics of Plasmas*, Vol. 12, No. 5, 2005, pp. 054504.

[69] Nichols, B. J. and Witteborn, F. C., "Measurements of Resonant Charge Exchange Cross Section in Nitrogen and Argon between 0.5 and 17 eV," TN D-3265, NASA, 1966.

[70] Powell, K. G., Roe, P. L., Linde, T. J., Gombosi, T. I., and De Zeeuw, L. D. L., "A Solution-Adaptive Upwind Scheme for Ideal Magnetohydrodynamics," *Journal of Computation Physics*, Vol. 154, No. 2, 1999, pp. 284–309.

[71] Lemmer, K. M., *Use of a Helicon Source for Development of a Re-Entry Blackout Amelioration System*, 2009, PhD thesis, Department of Aerospace Engineering, University of Michigan.

[72] Otsu, H., Abe, T., and Konigorski, D., "Influence of the Hall Effect on the Electrodynamic Heat Shield System for Reentry Vehicles," *AIAA 2005-5049*, Jun 2005, presented at the 36th AIAA Plasmadynamics and Lasers Conference, Toronto, Ontario Canada.

[73] Candler, G. V. and MacCormack, R. W., "The Computation of Hypersonic Ionized Flows in Chemical and Thermal Nonequilibrium," *AIAA Paper 88-0511*, Januarary 1988, presented at 34th Aerospace Sciences Meeting, Reno, NV.

[74] Josyula, E. and Bailey, W. F., "Governing Equations for Weakly Ionized Plasma Flowfields of Aerospace Vehicles," *Journal of Spacecraft and Rockets*, Vol. 40, No. 6, 2003, pp. 845–857.

[75] Park, C., *Nonequilibrium Hypersonic Aerothermodynamics*, Wiley-Interscience, 1990.

[76] Candler, G. V. and MacCormack, R. W., "Computation of Weakly Ionized Hypersonic Flows in Thermochemical Nonequilibrium," *Journal of Thermophysics and Heat Transfer*, Vol. 5, No. 3, 1991, pp. 266–273.

[77] Kim, M., Keidar, M., and Boyd, I. D., "Two-dimensional Model of an Electromagnetic Layer for the Mitigation of Communications Blackout," *AIAA 2009-1232*, Jan 2009, presented at the 47th AIAA Aerospace Sciences Meeting including The New Horizons Forum and Aerospace Exposition, Orlando, Florida.

[78] Losev, S. A., Makarov, V. N., and Pogoskekyan, M. Y., "Model of The Physico-Chemical Kinematics Behind the Front of a Very Intense Shock Wave in Air," *Fluid Dynamics*, Vol. 30, No. 2, 2005, pp. 299–309.

[79] Morozov, A. I., Esinchuk, Y. V., Tilinin, G. N., Trofimov, A. V., Sharov, Y. A., and Shchepkin, G. Y., "Plasma Accelerator with Closed Electron Drift and Extended Acceleration Zone," *Soviet Physics Technical Physics*, Vol. 17, 1972, pp. 38–45.

[80] Morozov, A. I., "The Conceptual Development of Stationary Plasma Thrusters," *Plasma Physics Reports*, Vol. 29, No. 3, 2003, pp. 235–250.

[81] Koo, J., *Hybrid PIC-MCC Computational Modeling of Hall Thrusters*, 2005, PhD thesis, Department of Aerospace Engineering, University of Michigan.

[82] Koo, J. W. and Boyd, I. D., "Computational Model of a Hall Thruster," *Computer Physics Communications*, Vol. 164, No. 1-3, 2004, pp. 442–447, Proceedings of the 18th International Conference on the Numerical Simulation of Plasmas.

[83] Gaitonde, D. V., "A High-Order Implicit Procedure For The 3-D Electric Field in Complex Magnetogasdynamic Simulations," *Computers and Fluids*, Vol. 33, No. 3, 2004, pp. 345–374.

[84] Dellar, P. J., "A Note on Magnetic Monopoles and the One-dimensional MHD Riemann Problem," *Journal of Computational Physics*, Vol. 172, No. 1, 2001, pp. 392–398.

[85] Levchenko, I., Romanov, M., and Korobov, M., "Plasma Jet Interaction With a Spherical Target in Magnetic Field," *IEEE Transactions on Plasma Science*, Vol. 32, No. 5, 2004, pp. 2139–2143.

[86] Morris, D., Gilchrist, B. E., Gallimore, A. D., and Jensen, K., "Developing Field Emitter Array Cathode Systems For Electrodynamic Tether Propulsion," *AIAA Paper 2000-3867*, July 2000, presented at the 36th AIAA/ASME/SAE/ASEE joint propulsion conference and exhibit, Huntsville, AL.

[87] Chen, F. F. and Boswell, R. W., "Helicons-the Past Decade," *IEEE Transactions on Plasma Science*, Vol. 25, No. 6, Dec 1997, pp. 1245–1257.

[88] Bilen, S. G., Haas, J. M., Gulczinski, F. S., I., Gallimore, A. D., and Letoutchaia, J. N., "Resonance-probe Measurements of Plasma Densities in Electric-propulsion Plumes," *AIAA-1999-2714*, June 1999, presented at 35th AIAA/ASME/SAE/ASEE Joint Propulsion Conference and Exhibit, Los Angeles, CA.

[89] Choinière, E., Gilchrist, B. E., and Bilén, S. G., "Enhancement of Electrodynamic Tether Electron Current Collection Using Radio Frequency Power," *Space Technology and Applications International Forum*, Vol. 552, No. 1, 2001, pp. 473–478.

[90] Piejak, R. B., Godyak, V. A., Garner, R., Alexandrovich, B. M., and Sternberg, N., "The Hairpin Resonator: A Plasma Density Measuring Technique Revisited," *Journal of Applied Physics*, Vol. 95, No. 7, 2004, pp. 3785–3791.

[91] Karkari, S. K., Gaman, C., Ellingboe, A. R., Swindells, I., and Bradley, J. W., "A Floating Hairpin Resonance Probe Technique for Measuring Time-Resolved Electron Density in Pulse Discharge," *Measurement Science and Technology*, Vol. 18, No. 8, 2007, pp. 2649–2656.

[92] Ohler, S. G., Gilchrist, B. E., and Gallimore, A. D., "Nonintrusive Electron Number Density Measurements in the Plume of a 1 kW Arcjet using a Modern

Microwave Interferometer," *IEEE Transactions on Plasma Science*, Vol. 23, No. 3, Jun 1995, pp. 428–435.

[93] Choi, I. and Chung, C.-W., "A Simple Analysis Method For the I-V Curve Of Single Langmuir Probes," *abstract #FTP.107*, October 2008, presented at the 61st Annual Gaseous Electronics Conference, Dallas, TX.

[94] Fujino, T. and Ishikawa, M., "Numerical Simulation of Control of Plasma Flow With Magnetic Field for Thermal Protection in Earth Re-entry Flight," *IEEE Transactions on Plasma Science*, Vol. 34, No. 2, 2006, pp. 409–420.

[95] Yamamoto, Y. and Yoshioka, M., "CFD and FEM Coupling Analysis of OREX Aerothermodynamic Flight Data," *AIAA 1995-2087*, Jan 1995, presented at the 30th Thermophysics Conference, San Diego, CA.

[96] Gaitonde, D. V., "Three-Dimensional Flow-Through Scramjet Simulation with MGD Energy-Bypass," *AIAA Paper 2003-172*, January 2003, presented at the 41st Aerospace Sciences Meeting, Reno, NV.

[97] Shutton, K. and Gnoffo, P. A., "Multi-component Diffusion with Application to Computational Aerothermodynamics," *AIAA Paper 1998-2575*, June 1998, presented at the 7th AIAA/ASME Joint Thermophysics and Heat Transfer Conference,Albuquerque, NM.

[98] White, F. M., *Viscous Fluid Flow*, McGraw-Hill Book Company, 3rd ed., 2006.

[99] Gnoffo, P. A., Gupta, R. N., and Shinn, J. L., "Conservation Equations and Physical Models for Hypersonic Air Flows in Thermal and Chemical Nonequilibrium," TP 2867, NASA, 1989.

[100] Matsuo, T., Tadamatsu, A., and Shimasaki, M., "3-D Magnetohydrodynamic Field Computation of Supersonic Duct Flow of Weakly Ionized Plasma," *Magnetic, IEEE Transactions on*, Vol. 39, No. 3, May 2003, pp. 1444–1447.

[101] Meyer, R. X., "Magnetohydrodynamic-Hypersonic Flow in the Quasi-Newtonian Approximation," *Reviews of Modern Physics*, Vol. 32, No. 4, Oct 1960, pp. 1004–1007.

[102] Poggie, J., "Computational Studies of Magnetic Control in Hypersonic Flow," *AIAA-2001-196*, Jan 2001, presented at 39th Aerospace Sciences Meeting and Exhibit, Reno, NV.

[103] Mitchner, M. and Kruger, C. H., *Partially Ionized Gases*, John Wiley, 1973.

[104] Fujino, T., Sugita, H., Mizuno, M., Funak, I., and Ishikawa, M., "Influences of Electrical Conductivity of Wall on Magnetohydrodynamic Control of Aerodynamic Heating," *Journal of Spacecraft and Rockets*, Vol. 43, No. 1, 2006, pp. 63–70.

[105] Fujino, T., Funak, I., Mizuno, M., Sugita, H., and Ishikawa, M., "Developing Field Emitter Array Cathode Systems for Electrodynamic Tether Propulsion," *AIAA Paper 2004-2561*, June 2004, presented at the 35th AIAA Plasmadynamics and Lasers Conference, Portland, Oregon.

[106] Borghi, C. A., Carraro, M. R., and Cristofolini, A., "Numerical Modeling of MHD Interaction in the Boundary Layer of Hypersonic Flows," *IEEE Transactions on Magnetics*, Vol. 39, No. 3, 2003, pp. 1507–1510.

[107] JAXA(Japan Aerospace Exploration Agency) hompage. http://www.jaxa.jp/.

[108] Inouye, Y., "OREX Flight - Quick Report and Lessons Learned," *Aerothermodynamics for space vehicles*, edited by J. J. Hunt, Vol. 367 of *ESA Special Publication*, 1995, pp. 271–278.

[109] Goebel, D. M. and Katz, I., *Fundamentals of Electric Propulsion: Ion and Hall Thrusters*, Wiley-interscience, 2008.

[110] Morozov, A. I., "Focussing of Cold Quasineutral Beams in Electromagnetic Fields," *Soviet Physics-Doklady*, Vol. 10, No. 8, February 1966, pp. 775–777.